sensors

MDPI

Review

Road Map of Semiconductor Metal-Oxide-Based Sensors: A Review

Taposhree Dutta [1], Tanzila Noushin [2], Shawana Tabassum [3] and Satyendra K. Mishra [4,5,*]

[1] Department of Chemistry, IIEST Shibpur, Howrah 711103, West Bengal, India; taposhreedutta812@gmail.com
[2] Department of Electrical and Computer Engineering, The University of Texas at Dallas, Richardson, TX 75080, USA; tanzila.noushin@utdallas.edu
[3] Department of Electrical Engineering, The University of Texas at Tyler, Tyler, TX 75799, USA; stabassum@uttyler.edu
[4] Danish Offshore Technology Center, Technical University of Denmark, 2800 Lyngby, Denmark
[5] SRCOM, Centre Technologic de Telecomunicacions de Catalunya, 08860 Castelldefels, Barcelona, Spain
* Correspondence: smishra@cttc.es

Abstract: Identifying disease biomarkers and detecting hazardous, explosive, flammable, and polluting gases and chemicals with extremely sensitive and selective sensor devices remains a challenging and time-consuming research challenge. Due to their exceptional characteristics, semiconducting metal oxides (SMOxs) have received a lot of attention in terms of the development of various types of sensors in recent years. The key performance indicators of SMOx-based sensors are their sensitivity, selectivity, recovery time, and steady response over time. SMOx-based sensors are discussed in this review based on their different properties. Surface properties of the functional material, such as its (nano)structure, morphology, and crystallinity, greatly influence sensor performance. A few examples of the complicated and poorly understood processes involved in SMOx sensing systems are adsorption and chemisorption, charge transfers, and oxygen migration. The future prospects of SMOx-based gas sensors, chemical sensors, and biological sensors are also discussed.

Keywords: semiconductor metal oxides; gas sensor; chemical sensor; biosensor; conduction band; valence band; p-n junction

Citation: Dutta, T.; Noushin, T.; Tabassum, S.; Mishra, S.K. Road Map of Semiconductor Metal-Oxide-Based Sensors: A Review. *Sensors* **2023**, *23*, 6849. https://doi.org/10.3390/s23156849

Academic Editors: Guillermo Villanueva, Tadeusz Pisarkiewicz and Artur M. Rydosz

Received: 18 April 2023
Revised: 22 June 2023
Accepted: 19 July 2023
Published: 1 August 2023

1. Introduction

In sensing applications, metal oxides (MOxs (metal oxides), mainly II–VI semiconductors) are mostly used due to their inexpensiveness, ease of manufacture, quick response time, wide detection range, and resistance to harsh conditions [1,2]. For sensors to be effective, (i) there must be a charge transfer between the analytes and sensing materials and (ii) the measurement must have an analyte concentration dependence [3,4]. In addition, there is a need for efficient and effective methods for detecting volatile, chemical, and biological compounds and molecules. Analytical chemistry methods, such as spectrophotometry, fluorometry, gas chromatography (GC), and high-performance liquid chromatography (HPLC), were previously used to detect these molecules accurately. Furthermore, these methods were heavy, expensive, had low throughput, time-consuming pretreatment steps, required highly skilled operators and significant power consumption, and did not provide real-time information for risk reduction or decision-making [5]. As a result of these limitations, most present sensing methods rely on SMOx-based materials for sensing applications, such as 1D and 2D field effect transistors (FET) and the Internet of things (IoT) [3,4,6–8].

Compounds with high levels of ionic bonding or electrostatic interaction are called semiconductor metal oxides (SMOxs) [9,10]. In recent years, they have attracted a great deal of attention due to their excellent sensing capabilities, adaptability in terms of size, ease of manufacture, and low power consumption. By tuning the size and composition of the materials, the electrical, optical, mechanical, catalytic, and magnetic properties can be

modulated. Because of their large surface-area-to-volume ratio, SMOxs, which have a size range between 1 and 100 nm, exhibit unique physical and chemical properties [11–16]. In addition to the size and geometry of the SMOx material, electron transport is also influenced by it [17,18]. Adding dopants, impurities, composite structures, or metal additives can further manipulate the charge transfer in a SMOx. In addition to improving the long-term stability and selectivity, these components lower the operation temperature, energy consumption, and humidity interference of pristine SMOx [19–23]. There are two types of SMOx materials: n-type and p-type, depending on the type of dopants. In SMOx, oxygen vacancies serve as electron donors, and hence, these compounds are n-type. Conversely, p-type SMOx, such as CuO, Co_3O_4, Cr_2O_3, and NiO, have metal ions and are electron acceptors. As a result of their tunable sensitivity, selectivity, and response time, SMOx-based materials are widely used in sensors that detect gases, chemicals, and biomolecules. With SMOx-based sensors, a wide range of gases can be detected, such as oxidizing gases and reducing gases [17,23].

Here, we present a brief review of the fundamentals and sensing properties of SMOx materials; the factors that influence their sensing performance; and their applications in gas, chemical, and biological sensing. There was a variety of literature available on SMOx gas sensors [24–31] and biosensors [32]. This article reviewed different aspects of SMOx materials and their sensing properties in one comprehensive article. This review provides researchers with a better understanding of the fundamentals and sensing applications of SMOx, enabling them to develop the next generation of SMOx-based sensors.

2. Fundamentals of Semiconductor Metal Oxides

The easy charge transfer properties of metal oxides (MOxs) make them unique among semiconducting materials. This effect is due to the large electronegativity difference, and thus, the high degree of ionic bonding, between the metal and oxygen that the MOx has. MOx has a conduction band minimum (CBM) and valence band maximum (VBM) of metal (M) ns and oxygen (O) 2p orbitals, respectively. Metals (Ms) and oxygen (O) have highly dispersed or localized orbitals (ns and 2p). Furthermore, metal oxides have a much higher dispersive valence band maximum (VBM) than n-type semiconductors. As an example, In_2O_3, ZnO, SnO_2, and their hybrid composites function as n-type MOx, while NiO and Cu_2O are p-type MOx. The first-known p-type transparent conductive oxide (TCO) was nickel oxide (NiO) [33].

The mobility (μ) of a carrier is inversely proportional to its effective mass (m*) and is given by the following equation:

$$\mu = e\,\tau/m^*$$

where τ is the free carrier scattering time

Controlled physical and chemical properties of metal oxides, including structural defects, morphology, grain size, and specific surface area, enable them to be used in a range of applications, such as catalysis, sensors, energy conversion, and environmental monitoring [34,35].

3. Properties of Semiconductor-Metal-Oxide-Based Sensors

Regarding the greenhouse effect, MOx-based sensors are used for the rapid detection of harmful and toxic gases, where the low concentration (in ppm or ppb) of the target gas is converted into a measurable electrical, optical, or magnetic signal. In these sensors, metal oxide semiconductors and metal oxide–polymer composites are used to produce excellent sensitivity [36–38]. As a result, semiconducting metal oxides (SMOxs) can be used to detect low gas concentrations with a high sensitivity and rapid response. A SMOx-based sensor is characterized by its low cost, rapid response and recovery time, high stability, simple electronic interface, and low maintenance, making it an ideal and promising material for detecting toxic gases [5,31,39,40]. Materials made of SMOx are ionic solids, which are held together by strong ionic bonds between positive metallic and negative oxygen ions. Semiconductor metal oxides (SMOxs) have filled electronic shells, making them more

thermally and chemically stable than free metal oxides. Incomplete electronic shells d endow optical properties, such as high dielectric constants [39,41–43]. Depending on the design, a SMOx can be flexible; porous; and can be in a zero-dimensional shape (0D), a 1D shape, a 2D shape, or a 3D shape [44–46]. As the temperature increases, SMOx materials' conductivity (and hence resistance) changes. Moreover, optical, electrical, and magnetic fields affect the conductivity of SMOx.

Understanding semiconductor metal oxides (SMOxs) is crucial to developing sensors with high sensitivity. SMOx sensing properties are affected by physical factors, such as crystalline structure, defects, energy bands, impurities, charge transport, and p-n junction formation. In a SMOx, charge transfer can be controlled by doping with donor materials [47–49].

3.1. Crystalline Structure with Defects

Due to noble metal doping, materials with high crystalline structures have been investigated to develop sensors. SMOx can be classified into two types of crystalline structure: monocrystalline and polycrystalline. A monocrystalline structure is formed by a regular arrangement of atoms. Conversely, polycrystalline structures consist of small single crystals arranged randomly. On the other hand, non-crystals possess irregular shapes with short-range structural order [50–52]. As an example, the surface of a crystal of SnO_2 usually lacks one or more atoms, resulting in abundant unsaturated bonds. Consequently, SnO_2 exhibits high chemical activity and participates in redox reactions [53,54]. SnO_2 has a tetragonal crystal structure [55,56], while ZnO has a hexagonal structure [44,57]. Semiconductor metal oxides (SMOxs) have special crystal structures that influence their physiochemical activity (Table 1).

Table 1. Some semiconductor metal oxide (SMOx)-based sensors with their structural parameters.

SMOx	Lattice Parameters	Applications	References
Nickel oxide (NiO)	**Cubic** Fm3m a = 2.983 Å b = 2.983 Å c = 5.160 Å	1. NO_2, CO gas sensing 2. Ammonia sensing 3. Ethanol sensing 4. Uric acid sensing 5. Lactic acid sensing 6. Glucose sensing	[58–65]
Cobalt oxide (CoO)	**Cubic** Fm3m a = 3.024 Å b = 3.012 Å c = 5.316 Å **Hexagonal** $P6_3mc$ a = 3.269 Å b = 5.289 Å c = 5.646 Å	1. Gas sensing 2. Oxygen sensing 3. Aceton sensing	[66–69]
Tin dioxide (SnO_2)	**Cubic** Fm3m a = 3.640 Å b = 3.640 Å c = 3.640 Å **Tetragonal** P4/mnm a = 4.832 Å b = 4.832 Å c = 3.243 Å	1. Gas sensors 2. Formaldehyde sensing 3. H_2S sensing 4. Alkene sensing 5. H_2 sensing 6. Biomarker of lung cancer 7. CO sensing	[70–81]

Table 1. *Cont.*

SMOx	Lattice Parameters	Applications	References
Titanium dioxide (TiO_2)	**Tetragonal** $I4_1/amd$ a = 5.566 Å b = 5.566 Å c = 5.566 Å **Tetragonal** $P4_2/mnm$ a = 4.653 Å b = 4.653 Å c = 2.969 Å	1. Hazardous gas sensing 2. Gas and UV sensor 3. Phosphopeptide sensing 4. Chemical sensing 5. Lactate sensing 6. Biosensors	[82–90]
Zinc oxide (ZnO)	**Cubic** Fm3m a = 3.068 Å b = 3.068 Å c = 3.068 Å **Hexagonal** $P6_3mc$ a = 3.289 Å b = 3.289 Å c = 5.307 Å	1. Gas sensor 2. H_2 sensing 3. Chemical sensing 4. Pesticide detection 5. Biosensors	[91–98]
Trimanganese tetraoxide (Mn_3O_4)	**Tetragonal** I41/amd a = 5.870 Å b = 6.348 Å c = 5.873 Å	1. H_2 gas sensing 2. Nitrogen sensing	[99,100]

There are various types of defects in SMOx, including point defects, line defects, plane defects, and volume defects. SMOx's physio-chemical activity can be enhanced by partial defects caused by impurities [101,102]. Photoelectric activity can induce point defects, also called 0D defects [103,104]. Another type of defect is a line defect, which is caused by partial crystal slides. There are two types of dislocation defects: closed rings and surface defects. There are also planar defects, which can include angular grain boundaries, stack layer faults, and twin crystals. In the crystal matrix, volume defects are voids with different structures, densities, and chemical compositions [105,106].

3.2. Energy Band of SMOx in the Presence of Impurities

In addition, the sensing property of n-type semiconductors and p-type semiconductors depends on the energy band structure of semiconductor metal oxides (SMOxs). When the SMOx thickness reaches a level comparable to the depletion layer width, the energy band is no longer constrained to the surface but is affected by a significant number of grains, which, in turn, affects the electronic structure and electron–hole charge carriers [107–109]. In general, an electron's conduction energy band becomes vacant when the minimum band gap energy (Eg) of the SMOx is reached (Figure 1). As a result, the valence band is left with holes. Electrons (e^-) and holes (h^+) are easily mobilized in the presence of an external electric field, while at low energy, electron–hole pairs ($e^- + h^+$) are electrostatically bound [110,111]. Since In_2O_3 has a small effective mass of electrons, its band structure shows a highly dispersive CBM. Its optical bandgap is 3.7 eV [112]. The presence of impurities induces intra-band electron transitions, such as electrons moving from defect states to ground states. By adjusting the size, shape, and composition of impurities, intraband gaps can be modulated. A SMOx sensor with a large Eg can work at high temperatures, which indicates that SMOx sensors are thermally

stable. When the operating temperature exceeds 300 °C, gas sensors should have a band gap greater than 2.5 eV. SMOx-based gas sensors have a weakly dependent chemical activity on ambient humidity [111,113,114] (Figure 1). In some core–shell semiconductors, for instance, the conduction and valence bands of the core and shell are staggered, and electrons and holes are separated. It was found that the conduction band energy was the lowest in the shell and highest in the core. The energy band offsets in semiconductor materials segregate electrons from the shell and holes from the core, allowing carrier recombination across the interface at a lower energy than any of their constituent band gaps [110,114]. Electron-saturation velocities are high, heterojunctions are readily available, gaps are broad, and breakdown fields are large, allowing for fast and very sensitive gas detection systems to operate. The size and shape of semiconductor materials can be controlled by applying strain due to quantum confinement phenomena. It is possible to adjust the bandgap range of semiconducting nanostructures due to their high elastic limit. The band structure governs the adsorption of light, charge separation, and recombination of charge, which determines the use of a SMOx in photoelectric conversion [109,114].

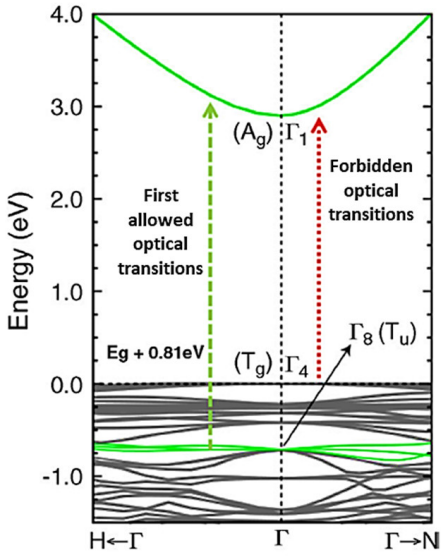

Figure 1. Band structure of In_2O_3 near the Brillouin zone. Here, a weak optical absorption is observed at 2.7 eV and a strong optical transition occurs between lower − lying valence bands [112].

Different electron–hole carriers produced by doped SMOx affect the conductivity [108,115]. There are two types of doped semiconductors: n-type and p-type [116–118]. The doping of materials regulates their conductivity and mass transfer, which is extremely important for gas sensors.

3.3. Carrier Transportation and Electronic Structure of SMOx

Conductivity in semiconductor metal oxides is affected by the production of free carriers, e.g., electrons in n-type semiconductors and holes in p-type semiconductors [119–121]. A stable concentration of conductive electrons and holes is maintained at thermal equilibrium [50,106,108]. Metal oxide's electronic structure, temperature, applied electronic field, doping, and lack of structural order in the material can influence carrier transport mechanisms, such as drift, diffusion, and recombination [122,123]. The movement of carriers from a high concentration to a low concentration is called diffusion [124,125]. Also, the carrier recombination rate affects the carrier lifetime and gas-sensing properties [110,126].

Its d valence bond orbitals impart unique physical and chemical properties for various applications, such as gas sensing [29,46].

3.4. Formation of p-n Junctions in a SMOx

Generally, p-n junctions form between semiconductors with different electronic structures [127,128]. A hole diffuses from a p-type semiconductor to a n-type semiconductor, leaving negatively charged ions on the p-type semiconductor. The n-type semiconductor, however, loses free electrons, leaving positively charged ions. p-n junctions possess unidirectional conductivity since the ions cannot diffuse and form a zone of space charge at the interface. A p-n junction affects the electronic, optical, and magnetic properties of SMOx materials [103,129]. It is possible to control the properties of SMOx to design it for a wide range of applications, such as gas sensing, catalysis, and energy storage. C. Han and co-workers presented hollow nanofibers based on p-CuO/n-ZnO for gas sensing [130]. Using atomic layer deposition (ALD), electrospun heterostructures were fabricated to investigate the effect of the composition on gas sensing. As the concentration is increased, the response rate slowly decreases, with Rzn/cu = 15.6. Compared with pure ZnO and pure CuO, these heterostructures exhibit 6 and 45 times higher responses to H_2S gas, respectively (Figure 2).

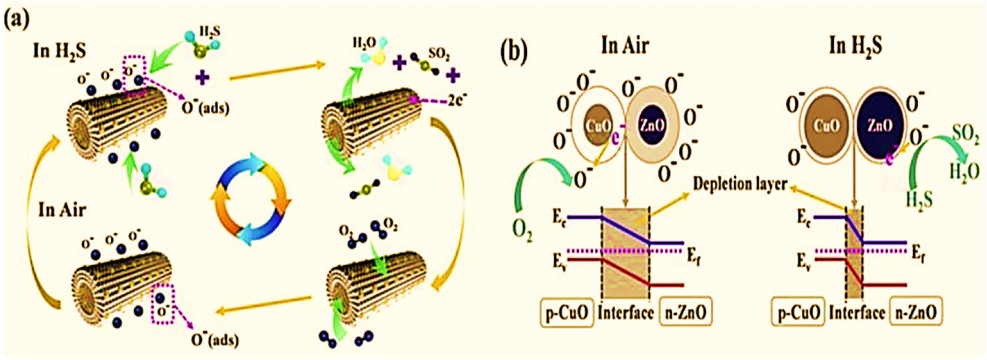

Figure 2. Schematic illustration of (**a**) H_2S gas detection via hollow nanofibers and (**b**) the formation of the depletion layer at the p−n interface [130].

According to Dhawale and co-workers, LPG detectability changes based on resistance or barrier height with a transition metal oxide [131]. The amount of chemisorbed oxygen on the surface; charges on the surface; diffusion; and other processes, such as gas adsorption and desorption, control the electrical resistance or barrier height (Figure 3). By adsorbing oxygen from the surrounding air on the film surfaces, ionic species like O_2-(ads), O-(ads), and O_2-(ads) are formed. Ionic species trap electrons from the valence band (topmost) and remove them from films. In consequence, these adsorbed oxygen species reduce the conductivity of n-type TiO_2. Whenever the chemisorption equilibrium is upset, the resistance or the barrier height of TiO_2 changes [132]. Since LPG is a reducing gas containing components such as CH_4, C_3H_8, and C_4H_{10}, gas-sensing mechanisms for LPG become more complicated [133]. During the exposure of LPG gas to a TiO_2 sensor, chemisorbed oxygen releases trapped electrons back onto the TiO_2 surface, resulting in a drastic reduction in the electrical resistance and barrier height. It is possible to increase the gas response by adding noble metals to metal oxide surfaces [134]. Painting Pd nanoparticles on TiO_2 improves the response of LPG over that of pristine TiO_2. The surface energy changes when Pd is added to TiO_2, and a spillover effect occurs [135]. Because of the weak interaction between the Pd atom and the oxygen gas, the Pd:TiO_2 sensor requires a relatively low temperature to dissolve [136]. However, a remarkably significant number of electrons are injected back into the topmost conduction band of TiO_2, thereby increasing the conductivity. Active Pd nanoparticle catalysts improve the LPG response by speeding up the process and providing more active sites. Furthermore, Lee and co-workers designed a hollow cube nanostructure with ZnO and CuO cores for acetone sensing, using the CuO (a p-type material) as a catalyst [134]. The n-type ZnO and p-type CuO domains produced a consistent p-n junction. When the two materials were still connected, charge conduction took place across the p-n junction, resulting in a balance in Fermi energies. The result was the formation of charge depletion layers and a potential barrier at the contact. Finally,

the ZnO–CuO core–hollow cube nanostructures at 200 °C displayed a 680 k resistance compared with the 8.8 kΩ of the CuO hollow cubes at the p-n junction. Surface-adsorbed oxygen species were consumed and the surface charge in CuO domains was reduced by acetone. Additionally, electrons were donated to the ZnO domain by removing the adsorbed oxygen species close to the interface. In response to this charge restructuring, the charge depletion area moved farther into the CuO domains. A considerable increase in resistance was observed across the CuO surface compared with the nanocubes without ZnO cores [134–136].

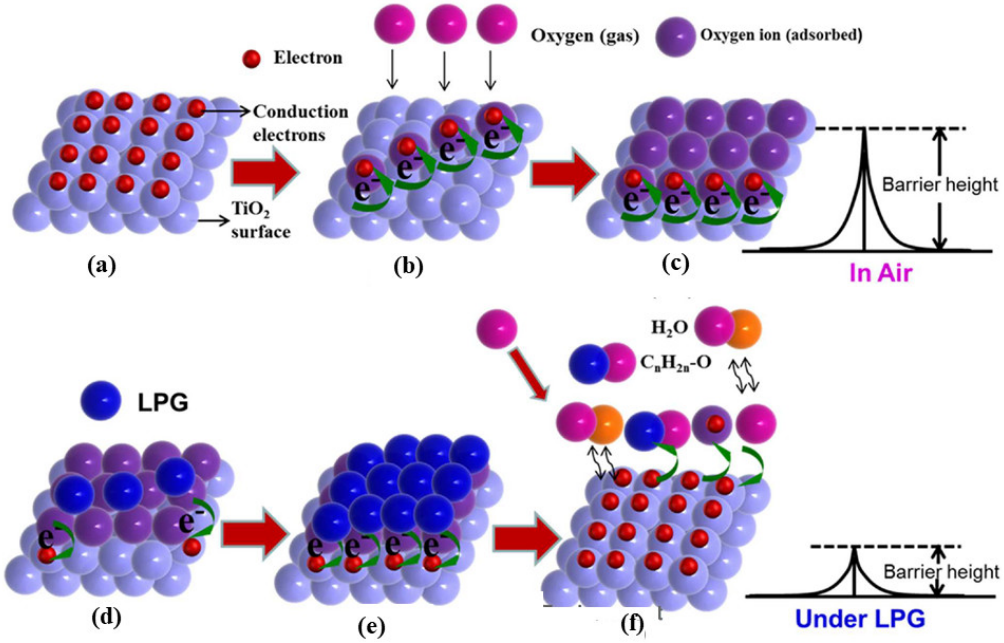

Figure 3. TiO_2 sensing mechanism shown schematically with exposure to LPG and in air. (**a**–**c**) TiO_2 sensor in air, where ionic species (O_2^-, O^- and O^{2-}) form due to adsorption of oxygen from ambient air on the surface film and capture the electrons from n-type TiO_2; (**d**–**f**) When LPG exposed and interacted with adsorbed oxygen, large number of electrons re-injected on TiO_2 surface and decreased the barrier hight [131].

3.5. Intrinsic Physical Characteristics

Several physical characteristics affect the application of SMOx materials in numerous fields, including morphology, particle size, crystal face, and porosity. A SMOx-based sensor, for instance, has nanoscale pores that can act as barriers to small grain sizes and improve the electronic transmission of sensitive receivers, thus influencing sensitivity to gases [36,137]. In order to diffuse gas molecules into the sensitive receptor, SMOx surface pores should be large. It has excellent sensitivity characteristics because it has large pores on the surface and small pores on the bulk, and it has good grain boundary contact [138,139].

4. Gas-Sensing Applications

A gas sensor fabricated with a gas-sensing element can detect analytic gas species by converting surface interactions into electrical signals [139]. In the last few decades, metal oxide (MOx) gas sensors with a simple and cost-effective fabrication process, high sensing response, and short recovery time captivated the attention of researchers because of their excellent surface morphology, high structural stability, adaptable electrical properties, and grain size, where metal oxide is used as the chemosensory material [5,140–143]. In 1960, Seiyama et al. introduced the gas-sensing properties of ZnO thin films, which have been used and studied extensively since then [144,145]. The advancement of gas sensing technology has allowed modern gas sensors to operate at low power [146–152]. As a result

of chemical reactions between gas molecules and semiconductor metal oxide surfaces, semiconductor-metal-oxide-based gas sensors have great potential (Figure 4) [144,153,154].

SMOx-based chemoresistors are portable devices that use a battery to operate at high temperatures. In factories, plants, and industries, these devices are used for detecting hazardous gases, for example, oxygen control in the exhaust emissions of gasoline, diesel, and gas engines, and humidity and air quality control in automobiles [155,156]. SMOx-based gas sensors are more sensitive when dopants are used [157], and the electrical properties of SMOx depend on the interactions between the sensor surface and gas molecules adsorbing on it [158].

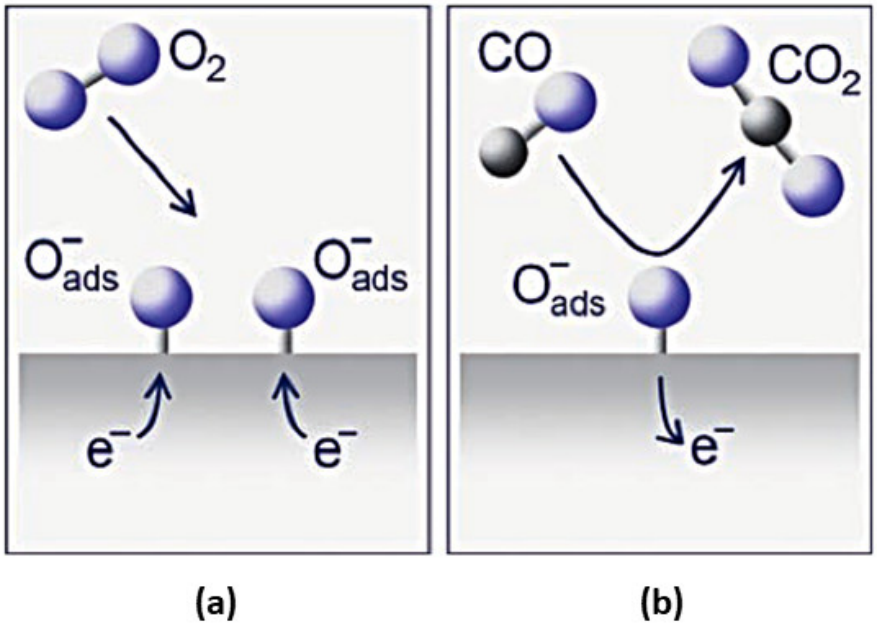

Figure 4. Schematic illustration of the chemical reactions at the surface of an n-type gas sensor. (**a**) Chemisorption of oxygen (O_2) traps electrons from the conduction band and forms the charged species atomic O^- and molecular $O_2{}^-$. (**b**) Reducing gases (e.g., CO) react with the surface-bound oxygen and release electrons back into the crystal leading to changes in the electrical conductivity that are related to the CO concentration [159].

4.1. Mechanism of SMOx-Based Gas Sensors

The sensing mechanism of a SMOx is complicated by different key factors that affect the sensing attributes, including the adsorption ability, electrophysical property, catalytic and chemical activity, thermodynamic stability, and surface adsorption or desorption properties [30,160–164]. Two processes are involved in the sensing mechanism of SMOx-based gas sensors: reception and transduction [19,156]. In the reception process, the sensor converts the chemical reaction into energy, which is then converted into analytical signals in the transduction process [165]. Through the gas–solid interface, the target gas is detected on the SMOx surface through a change in electrical properties. In the transduction process, chemical changes are induced in the surface and transformed into electrical signals, such as resistance changes in the sensor [166]. As a result of reversible redox reactions between reactive gases and the SMOx surface, a SMOx's electrical properties change. Finally, the electrical signals were measured and displayed using suitable circuits, such as a microprocessor unit [12,167].

The detection of gas molecules is primarily carried out by monitoring variations in the device current (IDS) or threshold voltage (VTH) caused by the adsorption of nearby molecules. In the case of Ohmic connections, such changes can occur by modulating the conductivity of FET channels, and in the case of non-Ohmic links, by modifying the Schottky barrier height. Due to the conductivity of the FET channel, the free-carrier density

in 1D/2D channels is decreased or increased during this process. If the hole (electron) carrier density alters due to gas adsorption, the phenomenon is called hole (electron) doping. An adsorption-induced doping process results in a positive (electron-acceptor) or negative (electron-donor) shift in the VTH, which, in turn, causes an alteration in the IDS for a VDS value. The adsorption of molecules from the surrounding environment can increase or decrease the charge carrier surface scattering and trapping. A change in the majority carrier mobility (p for holes and n for electrons) affects the channel conductivity for both p- and n-type FETs, modulating the IDS. A Schottky contact also modifies the metal workfunction, affecting the height of the energy barrier at the semiconductor interface [6,168].

To evaluate the response and recovery times of a FET sensor as a result of gas molecule adsorption/desorption processes, the real-time measurement of the IDS for VDS and VGS values was used. Trans-characteristic analysis revealed different sensing mechanisms for a 1D and 2D FET. FETs have the advantage of simultaneously monitoring many electrical parameters, such as the IDS, VTH, SVTH, SW, and Ion/Ioff upon gas molecule adsorption, over two-terminal electrical devices (such as resistors, capacitors, and diodes). This can be used to retrieve data on the specific sensing mechanisms when target analytes interact with the FET, such as changes in the concentration of electrons/holes, the energy barrier at the semiconductor/metal interface, or the mobility of the majority of charge carriers. As a result, scientists can tweak the gadget's architecture and materials to enhance its performance. Aside from this, the sensitivity of the sensor can also be electrically tuned for the detection of low (by lowering the amount of charge in the channel and, consequently, the background current) and high concentrations of the target gas by varying the VGS value and the charge carrier concentration in the FET channel, as opposed to two-terminal electrical components, which prevent it from being effective [6].

Reception: On the SMOx surface, the reception process involves the reactions (i) ionosorption of oxygen to form reactive oxygen species and (ii) the reaction of these reactive oxygen species with reducing gases. When SMOx-based sensors are heated without oxygen, free electrons easily flow through their boundaries. A SMOx (e.g., SnO_2), on the other hand, forms a potential barrier when oxygen is adsorbed onto its surface due to its presence in the atmosphere. Through this interaction, atmospheric oxygen traps electrons from the bulk material, thereby depleting a region of electrons. As a result, an increased potential barrier is formed at the surface. The flow of electrons is impeded by this phenomenon, which increases the resistance. The surface of the SMOx sensor absorbs gas molecules when exposed to reducing gases, lowering the potential barrier and allowing electrons to flow more freely. As a result, the electrical resistance also decreases. SMOx-based sensors were demonstrated to be variable resistors.

Due to its wide band gap, SMOx has many electrophysical properties, including insulating behavior and semiconductor properties [169–172]. A change in conductivity is caused by electrons trapped in adsorbed molecules. Figure 5 [13] shows that electrons are extracted from the conduction band (Ec) when oxygen molecules (O_2) adsorb on the SMOx surface [173–175] using ionosorption [173,174]. A space charge layer is formed when this phenomenon causes an upward band bend, resulting in an electron-depleted region. By reacting with CO, oxygen species decrease the amount of adsorbed oxygen at the surface, which reverses the band-bending process (Reaction 2). In addition, SMOx gas sensors display increased conductivity with high temperatures (300–450 °C) [25]. In n-type semiconducting metal oxides, where the depletion region is smaller than the grain size, this mechanism is crucial and well-suited for sensing gases.

$$\frac{1}{2}O_2 + V_0^{++} + 2e^- \rightleftharpoons O_0 \quad (1)$$

where V_0^{++}—oxygen vacancy.

$$O_0 + CO \rightarrow CO_2 + V_0^{++} + 2e^- \quad (2)$$

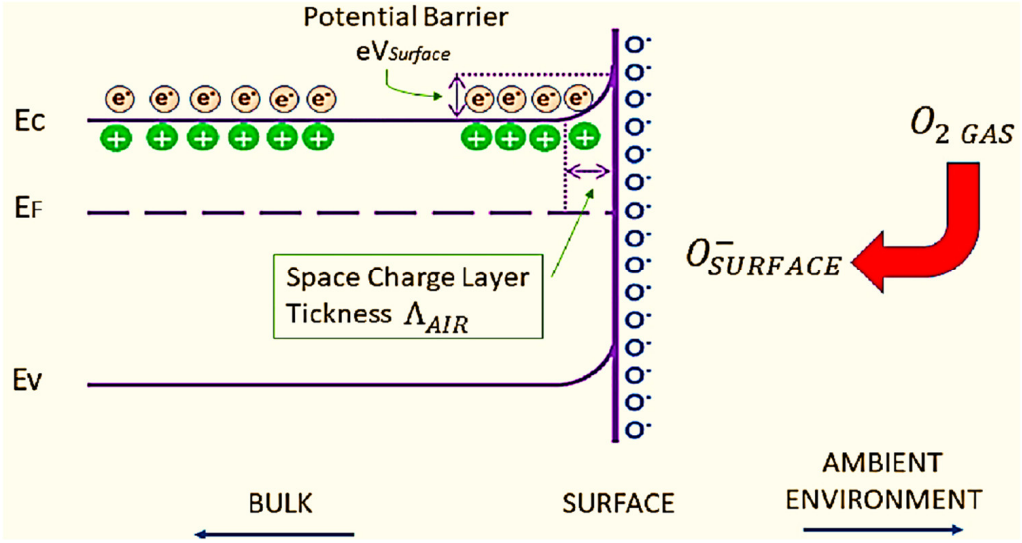

Figure 5. Schematic view of band−bending after the ionosorption of oxygen (chemisorption), where EC, EV, and EF denote the energies of the conduction band, valence band, and Fermi level, respectively. "e^-" represents conducting electrons and "+" represents donor sites [13].

SMOx gas sensors become oxidized when exposed to a reducing gas, such as CO, releasing electrons into the bulk material, resulting in a decrease in the number of O^- ions on the surfaces (Figure 6). As a result, the thickness of the space charge layer is reduced. By doing so, Schottky barriers between grains or particles become smaller, allowing electrons to easily pass through sensing layers.

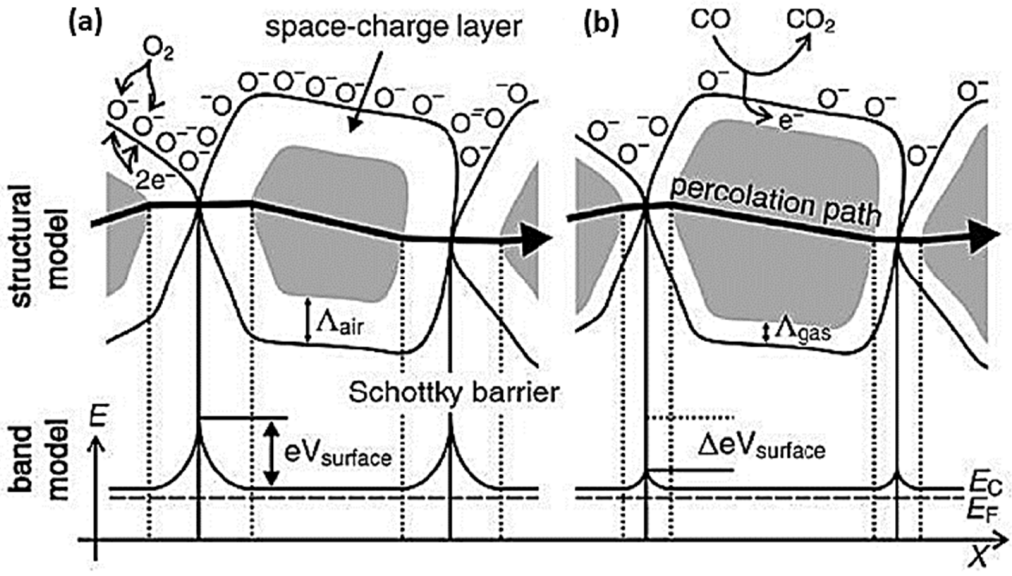

Figure 6. The structural and band models in the (**a**) presence of CO and (**b**) absence of CO [13,176].

Depending on the atmospheric composition, the surface reactions vary, which, in turn, changes the concentration of trapped charges on the surface and the associated space charge layer [177,178].

Transduction: It is necessary to convert surface charges into measurable electrical signals in order to obtain analytical signals. SMOx-based gas sensors measure surface reactions by varying the sensing layer's resistance. The surface charge is affected by the structural and morphological properties of the sensing layer [80,178], the electrical and chemical properties of SMOx, the size and shape of the SMOx material [179–181], and the

electrode's geometry [12]. According to Figure 7, spherical SMOx grains with a Debye length smaller than the grain radius were not affected by changes in the surface, resulting in an unaffected bulk region. A continuous Schottky barrier is created between different grain contacts at the surface as a result of the band bending. Due to oxygen biosorption, an electron-depleted surface layer formed in n-type SMOx, whereas a hole-depleted surface layer was observed in p-type SMOx [166,178,182].

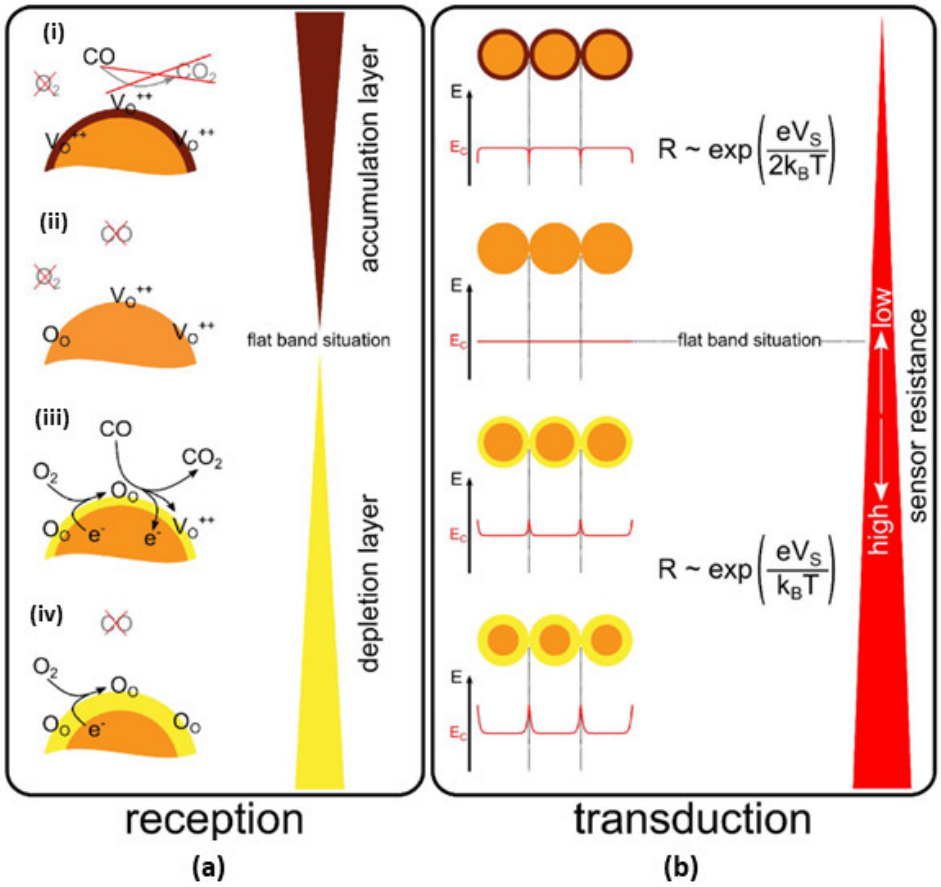

Figure 7. (**a**) Sensing mechanism of pristine n-type SMOx materials under four conditions in the reception process: (i) formation of an accumulation layer (brown color) in the presence of reduced gas with the absence of oxygen, (ii) flat band formation in the absence of surface states due to adsorbed species, (iii) formation of a depletion layer (yellow color) in the presence of oxygen and reducing gases, and (iv) formation of a depletion layer without reducing gas in the presence of oxygen. (**b**) Charge transport in the sensing layer depicting tentative resistance in the transduction process [20].

Conduction in p-type oxide semiconductors might be explained by a conflict between parallel routes spanning a broad resistive core (Rcore) and a constrained, p-semiconducting shell (Rshell). Barsan and co-workers provided a detailed explanation of the precise conduction model and energy band diagram of p-type oxide semiconductor-based gas sensors (Figure 8a) [166,182]. As shown in Figure 8a, the B region represents the electrode–semiconductor connections, while the A and C regions show the semiconductor grain-to-grain interactions. Oxygen anions on the surface of the SMOx react to form an oxidation process that injects electrons into the material, reducing the concentration of holes in the shell layer while increasing the sensor resistance (Figure 8b,c).

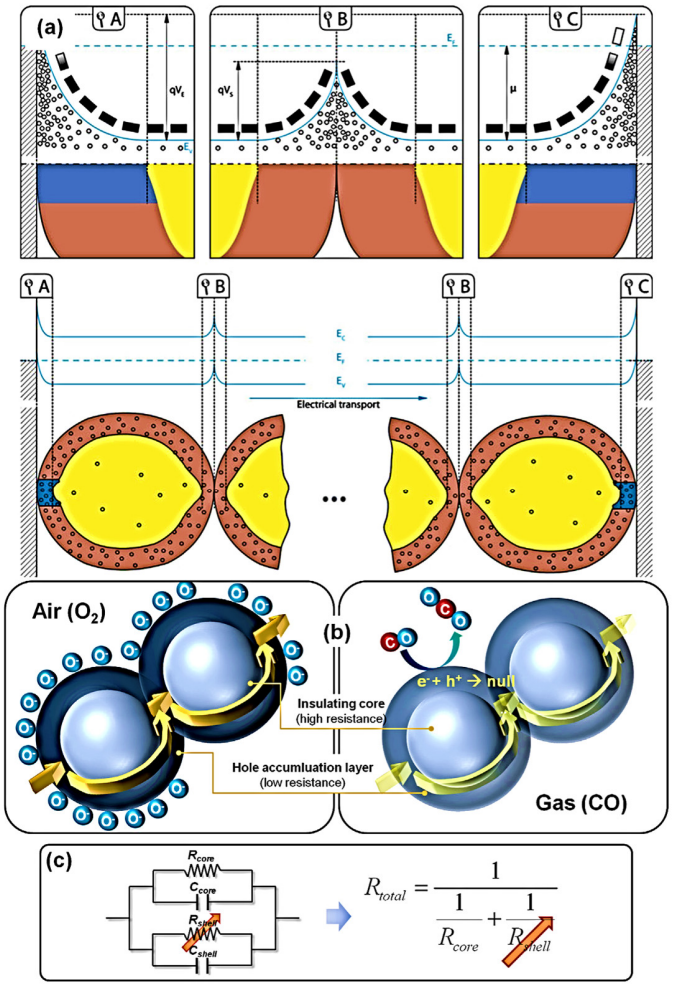

Figure 8. (**a**) Simplified representation of the essential sensing layer components for p-type oxide semiconductor gas sensors (low), where A and C are metal–semiconductor contacts and B is a grain-grain contact of a semiconductor. The energy band diagram described by Barsan and coworkers [166]: (**b**,**c**) p-type oxide semiconductors with a simplified gas-sensing mechanism and equivalent circuit [182].

P-type oxide semiconductors are known to lose resistance when exposed to oxidizing gases like NO_2 and O_3. As a result of the ionosorption of oxidizing gas, the concentration of holes in the shell layer increases. The chemo-resistive variation of p-type oxide semiconductors to oxidizing gases also appears to be not high when considering the gas-sensing mechanism. Based on literature data, NiO and CuO sensors respond moderately to 10–100 ppm NO_2 (Ra/Rg = 1.0–7.5) [183–185].

4.2. Sensitization Mechanism

The sensitization mechanism enhances the sensitivity of gas sensors by adding additional material or by modifying the existing material. The variation in the reception and transduction mechanisms increases the electronic and chemical interactions between the target gas and sensing material, resulting in a high sensitivity of the sensor [186–188]. As a result of dividing sensitization mechanisms into two main categories, namely, electronic sensitization and chemical sensitization, N. Yamazoe developed the concept of clear separation of electronic and chemical sensitization. By adding metal or metal oxide additives, both sensitizations could be achieved. During electronic sensitization, the additive accepts electrons from the analyte and changes its redox state or chemical potential (Figure 9a). Chemical sensitization, on the other hand, involves activation of the analyte, spillover, and a change in the surface oxygen concentration (Figure 9b). The concentration of charged

species at the surface and space charge layers remains unchanged without an analyte. As a result of the high surface concentration of active oxygen, a different phenomenon occurs during oxygen spillover. The high concentration of charged species at the surface of SMOx causes the band bending to increase when chemical activation occurs.

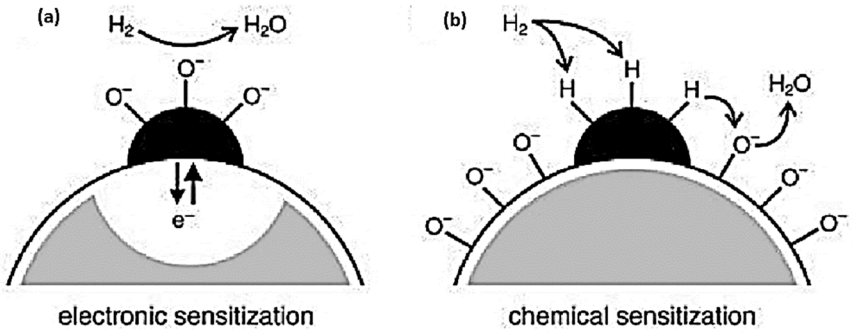

Figure 9. Sensitization mechanisms of SMOx by metal or metal oxide additives. (**a**) Electronic sensitization via changes in the Fermi level and (**b**) chemical sensitization via spillover [13].

Spillover effects promote the separation of molecular oxygen into an active surface. Spillover activation significantly impacted the sensor's gas-sensing properties. As the analyte gas adsorbs on the additive phase, the activated species are transferred to the SMOx surface, where the analyte gas reacts with active oxygen species (Figure 10). The oxidation catalysis process is affected by single additive sites, i.e. dopants [189] and by separate additive phases [190–192]. As a result of spillover effects, molecular oxygen separates into a more active surface. Chemical sensitization involves two important aspects: (i) the change in the surface charge of SMOx caused by chemical activation and (ii) the ambivalent relationship between catalytic activity and gas sensing. As an example, CO is activated by adsorption and transfer to SMOx surfaces, while other analytes (e.g., H_2) are activated by additive reactions. Analyte gas spillover activation enhances the reactivity of SMOx and accelerates oxygen vacancy formation. Despite the inverse spillover mechanism described by Korotcenkov et al. for the detection of reducing gases with Au-loaded SnO_2 (Figure 11a) [191], spillover mechanisms are generally used to improve the gas-sensing properties of metal-loaded SMOx (Figure 11b) [186,193–196].

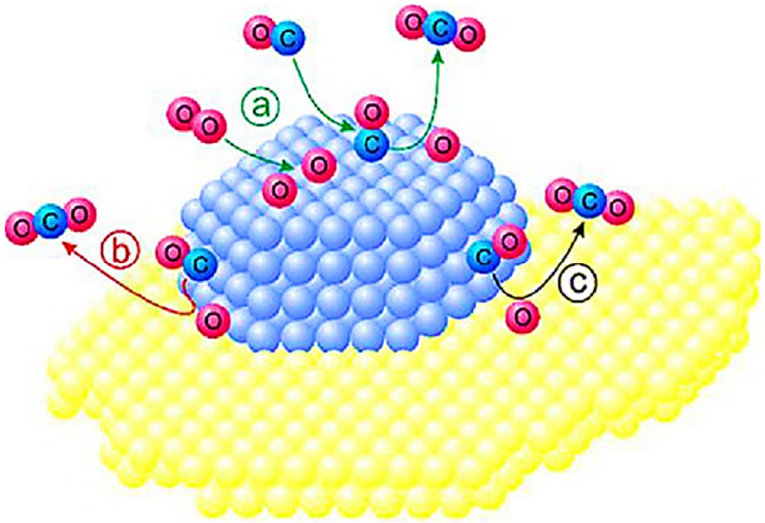

Figure 10. Schematic view of catalytic activation based on oxidation mechanism. (**a**) Direct reaction on the additive surface; (**b**) adsorption of oxygen on SMOx additive; (**c**) spillover of reactive species on the SMOx surface. O = oxygen (red colour), C = carbon (blue colour) on metal nanoparticle surface [189].

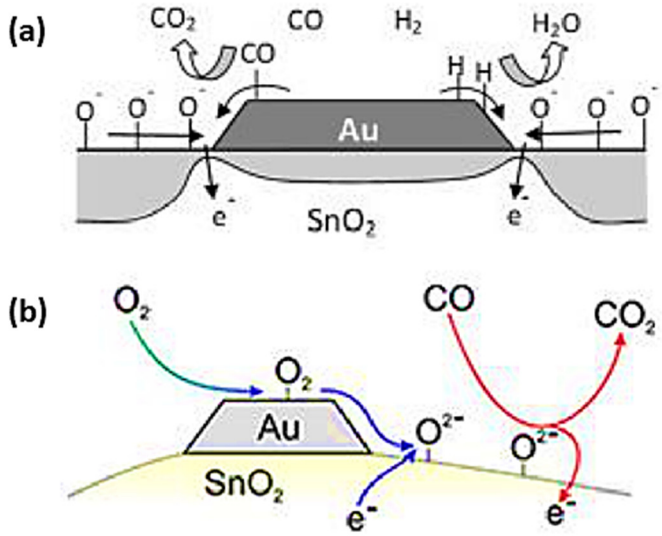

Figure 11. Schematic view of spillover mechanism on a Au− loaded SnO_2 gas sensor where (**a**) inverse oxygen spillover and (**b**) oxygen spillover take place [191,197].

The increase in initial band bending directly affects the resistance change due to changes in the surface charge of SMOx, which shows a significant impact on the electrical and chemical properties of the SMOx surface, and consequently on transduction and reception processes. The initial band bending is described by a non-linear relationship between the surface charge (Q_S) and the surface potential (V_S). The Schottky approximation, described by S. R. Morrison, provides a simplified explanation of this relationship [198] as follows:

$$V_s = \frac{e}{2\varepsilon\varepsilon_0 n_b} \times Q_S^2 \quad (3)$$

where

e—elementary charge;
ε—permittivity of SMOx;
ε_0—permittivity of vacuum;
n_b—concentration of charge carriers in the bulk.

The sensor signal (S) for the reducing gas is defined by the ratio of the resistance in the reference atmosphere (R_{ref}) and the resistance in the presence of the analyte gas (R_{gas}) [178]:

$$S = \frac{R_{ref}}{R_{gas}} \quad (4)$$

The relationship between the differential surface potential ΔV_s and sensor signal S is as follows:

$$S = \exp\left(\frac{e\Delta V_s}{k_g T}\right) \quad (5)$$

The change in band bending at the surface, which is represented as the differential surface potential ΔV_s as a function of the change in surface charge ΔQ_s as follows:

$$\Delta V_S = \frac{e}{2\varepsilon\varepsilon_0 n_b} \times \Delta Q_S.(2 \times Q_{S,0} - \Delta Q_S) \quad (6)$$

According to Equation (6), the change in the surface potential (ΔV_S) is a function of the initial surface charge ($Q_{S,0}$) and the change in the surface charge (ΔQ_S) as a consequence of reactions taking place on the surface. Combining Equations (5) and (6), the impact of different $Q_{S,0}$ values on the sensor signal can be calculated. From Figure 10, it is evident that the change in the surface charge results in a change in the sensor signal. The slopes of

the curves indicate that a higher initial band bending leads to an increased sensor signal and hence sensitivity. The increase in slopes, referred to as n-values, is experimentally observed in SnO_2 materials due to the self-doping effect (Figure 12) [199]. The presence of two SMOx materials shows a major effect on the electronic coupling between them, as the second material provides additional reaction sites on the additive phase [187,188].

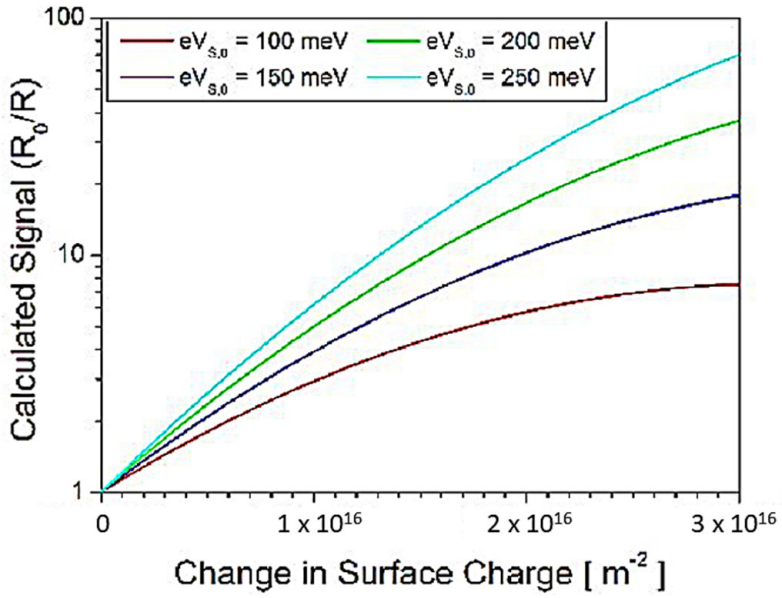

Figure 12. Sensor signal changes corresponding to changes in the surface charge for a SnO_2—based sensor at 300 °C [199].

4.3. Factors Affecting the Sensitivity

4.3.1. Chemical Composition

The chemical composition of SMOx plays a significant role in improving the adsorption ability, catalytic activity, sensitivity, and thermodynamic stability [200]. Recently, composite materials, like SnO_2-ZnO [201,202], Fe_2O_3-ZnO [203], and ZnO-CuO [204], were investigated for their improved performance. Furthermore, researchers are working on various ternary, quaternary, and complex metal oxides for different applications [205,206]. The combination of metal oxides and other components, for example, organic and carbon nanotubes, also showed promising results. Therefore, the chemical composition significantly influences the gas-sensing properties of composite metal oxides.

ZnO-SnO_2-composite-based sensors exhibit higher sensitivity compared with sensors made solely from tin dioxide or zinc oxide [203]. As described by De Lacy Costello and colleagues, the combined effect of two components in a synergistic effect enhances the sensitivity of sensors [203].

4.3.2. Surface Modification

Controlling the catalytic activity of gas sensors is another way to enhance their performance. Several widely used SMOxs, such as TiO_2, ZnO, SnO_2, Cu_2O, Ga_2O_3, and Fe_2O_3, have low activities [160]. Without a catalyst, pure SnO_2 exhibits poor sensitivity [207]. Noble metals, such as Pt, Au, Pd, and Ag, were highly effective oxidation catalysts and were also used to enhance reactions on metal oxide surfaces [208–212]. In order to detect Pd upon deposition, two mechanisms are involved: (i) electronic and (ii) chemical. The electronic mechanism involves the formation of depletion zones around the modified particles (Figure 13b) and modulation of the nano-Schottky barriers, which result from changes in the oxidation state of Pd during oxygen adsorption and desorption, boosting the sensing process. In Figure 13a, oxygen is shown as ionosorbing on the surface of Pd. Pd, which catalyzes molecular oxygen dissociation, is a better oxygen dissociation catalyst than tin

oxide. As a result, the atomic products diffuse to the surface of the SMOx (Figure 13a) [213]. Oxygen molecules reside on the oxide and diffuse to the catalyst particle. A back-spillover effect (Figure 13a) and effective "capture radius" (Rc) are observed around Pd particles (Figure 13b). An oxygen delivery system is developed when oxygen layers cover whole metal oxide surfaces [214]. This process enhances the oxygen ionosorption on MOx and the detection sensitivity [215].

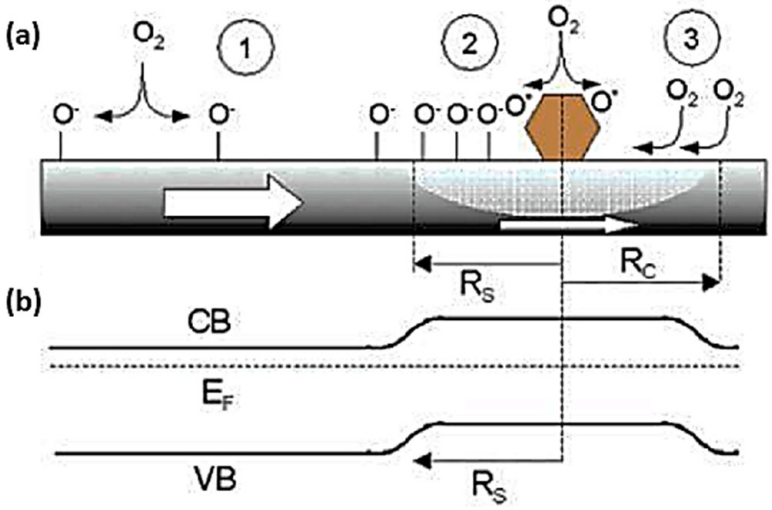

Figure 13. (**a**) Schematic view of a SnO_2 nanowire surface in the presence of O_2 and (1) ionosorption of oxygen at defect sites of the pristine surface; (2) molecular oxygen dissociation on Pd nanoparticles followed by spillover of the atomic species onto the oxide surface; (3) capture by a Pd nanoparticle of weakly adsorbed molecular oxygen. (**b**) band diagram of pristine SnO_2 in the vicinity of a Pd nanoparticle. The radius of the depletion region is determined by the radius of the spillover zone [216].

4.3.3. Microstructure

A significant effect on sensitivity was also observed when metal oxides were synthesized with an optimal morphology and crystallographic structure. SMOx sensors are made more sensitive by using small-grain materials in this method. According to Lu et al. the sensitivity of a SnO_2-based sensor to 500 ppm CO increased dramatically for particle sizes smaller than 10 nm (Figure 14a). Similarly, 20 nm particles demonstrated ten times more sensitivity compared with 25~40 nm particles (Figure 14b) [217]. In the case of small grains with narrow necks, this size is less than twice the thickness of the surface charge layer [218]. In metal oxide gas sensors, the size of the grains affects the mobility of free charge carriers, and therefore, the number of collisions that occur between them. Additional scattering centers are formed by adsorbed species, which influence carrier mobility as well [178]. As a result of this method, metal oxide gas sensors are significantly more sensitive [178,219–222]. It is worth noting that using a small crystal size did not always enhance the gas sensor's response [223]. Sensors fabricated with SnO_2 nanocrystals (50 nm) synthesized via gel combustion showed a faster response than those fabricated with SnO_2 nanocrystals (12–13 nm) synthesized via the hydrothermal method. In contrast with hydrothermally synthesized SnO_2 nanocrystals, which consist of small grains but tend to aggregate into large entities, gel-combustion-synthesized SnO_2 nanocrystals were more porous. As a result, tuning the grain size of metal-oxide-based gas sensors could enhance their performance. In addition to modulating structural stability, grain size affected the surface changes, as well as the catalytic activity [224].

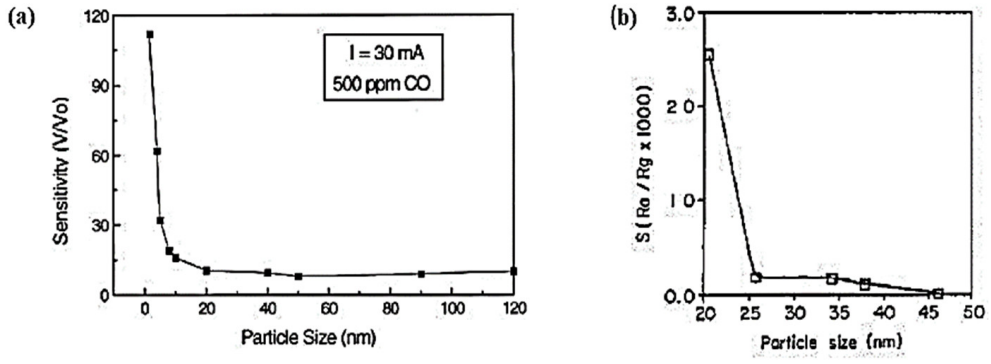

Figure 14. (**a**) Effect of particle size on CO gas sensitivity [225]; (**b**) effect of particle size on H_2 gas sensitivity [217].

4.3.4. Humidity and Temperature

A significant role was played by humidity in modulating the activity of metal-oxide-based gas sensors. A variety of humidity sensors based on metal oxides have been developed. In contrast, the mechanisms of sensing water vapor and CO, NO_2, and H_2S gases differed. It was the ionic humidity sensor that was most commonly used with metal-oxide-based humidity sensors. H^+ or H_3O^+ ions produced by the dissociation of adsorbed water on the surface are the conduction mechanism in metal-oxide-based humidity sensors. Recent works [226,227] studied and described the adsorption of water on metal oxide surfaces and the mechanism of sensing water vapor. As a result of water adsorption on metal oxide surfaces, humidity decreased the sensitivity of metal oxide sensors (Figure 15) [228,229].

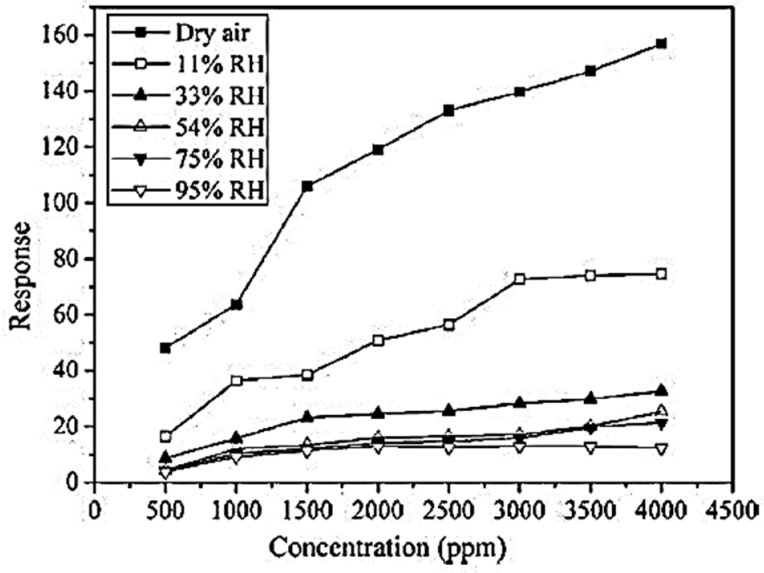

Figure 15. Response of Sm_2O_3 doped SnO_2 sensor for different concentrations of C_2H_2 at different relative humidity (RH) conditions [228].

Temperature is another important factor that affects the performance of metal oxide gas sensors. As shown in Figure 16, the sensor responses to different analytes show similar shapes as a function of temperature. The resultant shape depicted slow kinetics at low temperatures and increased desorption at high temperatures [216,230–234].

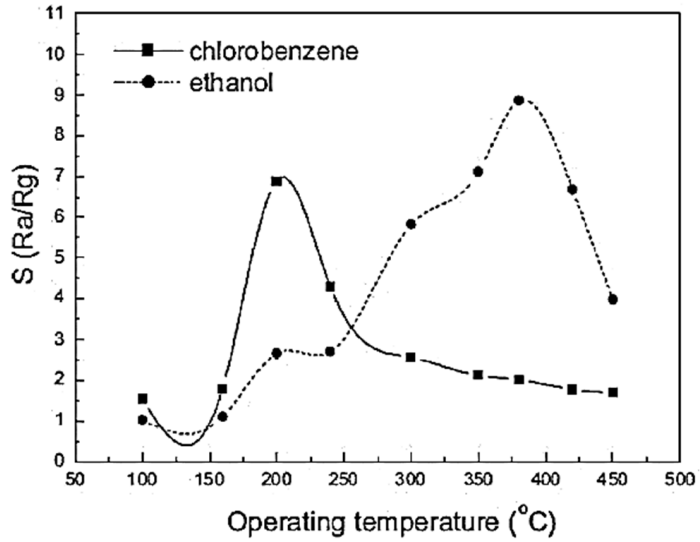

Figure 16. Response of a porous ZnO gas sensor as a function of operating temperatures [230].

4.3.5. Control Synthesis

The ability to detect gas depends on its composition, shape, size, and distribution. Depending on the crystallographic orientation of the metal oxide semiconductor, sensitivity is improved. A higher sensitivity is observed for ZnO with the crystallographic orientation (002) [235]. For the crystallographic orientation, a high surface-to-volume ratio is also crucial to achieving greater sensitivity. Furthermore, a well-organized pore structure and particle size contribute to a high surface-to-volume ratio. ZnO was characterized using a scanning electron microscope (SEM) after it was synthesized (Figure 17a,b). Surface morphology can be modified via chemical processing and variable annealing temperatures. As a result, hexagonal-shaped ZnO was developed (Figure 17b). A hexagonal shape with a high surface-to-volume ratio produces good sensitivity.

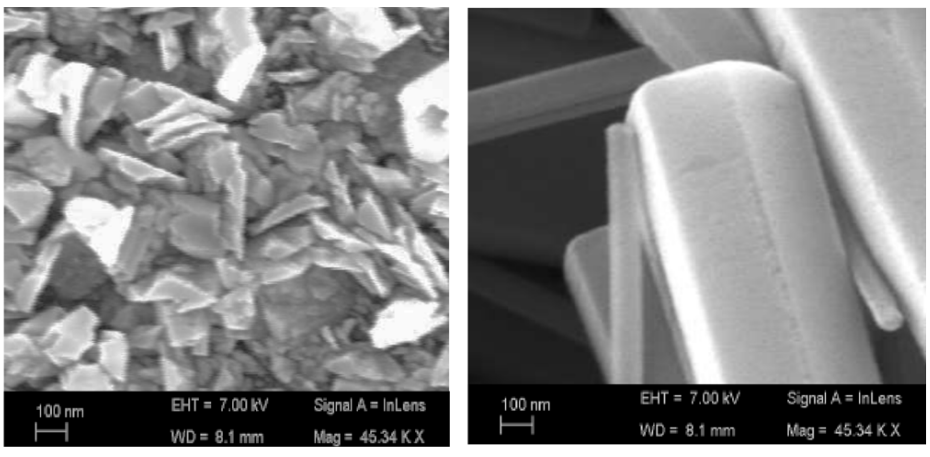

(a) **(b)**

Figure 17. SEM images of (**a**) ZnO before a chemical treatment and a (**b**) hexagonal ZnO nanorod [236].

4.3.6. Doping with a Noble Material

To assess conductivity, the effectiveness of catalytic reactions with target gas is measured on the surface of the sensing material. It is also important to improve catalytic activity in order to improve sensor performance. Undoped metal oxides exhibit significantly lower activity than doped ones [237]. Sputtering, thermal evaporation, or sol-gel doping could be used to dope semiconductors. A surface modification sometimes requires the combination of noble materials and MOxs (metal oxides). In addition to Pd, Ag, Au, and Pt nanopar-

ticles, second-phase nanoparticles with enhanced sensitivity were applied to host metal oxides [238]. As a result of the catalytic behaviour of noble metal nanoparticles, the chemical dissociation and reactions are increased [239]. The activity of Pd-functionalized SnO_2 is improved [216]. ZnO nanostructures decorated with PdO also demonstrate improved sensitivity [230].

4.4. SMOx-Based Gas Detection for Environmental Monitoring

Here, we discuss a few SMOx-based gas sensors for monitoring the toxicity of gases in the environment, industries, hospitals, health issues, etc.

4.4.1. Nitrogen Oxide Gas Detection

WO_3 sensors based on SMOx have been extensively used in gas sensors [240–245]. Most of the modified WO_3-based metal composites were used for NOx sensing [246–249]. Modified thermal evaporation techniques were used to obtain nanostructured WO_3 films with high surface roughness [240]. This technique produces high-response sensors with high selectivity and short response times, particularly at low temperatures (minimum 100 °C). Due to a high variation in electrical resistance, sensors at this temperature exhibited high sensitivity to NO_2 with a low detection limit (around 100 ppb). In contrast, low responses were observed when NH_3 (10 ppm) and CO (400 ppm) were present at high concentrations [240]. WO_3 sensing elements for high-temperature potentiometric NOx sensing were synthesized by Yang et al. using various synthetic methods. Mixed oxides based on WO_3 are also used for sensing. SMOx materials such as WO_3-Ti [246–248], WO_3-Pd, Pt, Au [249–252], WO_3-In_2O_3 [253], and WO_3-Bi_2O_3 [254] are used to fabricate selective and sensitive NOx gas sensors. Furthermore, TeO_2-based thin films were synthesized for NO_2 gas sensing [255,256]. As the NO_2 gas concentration increases, the response time decreases. A response time of about 6 min for 1 ppm of NO_2 gas and about 1.2 min for 120 ppm was reported. The recovery time was found to be longer than 8 min for each gas concentration [255].

The direct printing of numerous SMOxs, including ZnO, In_2O_3, SnO_2, and WO_3, was proposed by Kim and co-workers for the creation of an aligned network of NWs as the channel of a FET for NO_2 detection [257]. The diameters of the manufactured NWs, which had aggregates of grains between 5 and 15 nm, ranged from 100 to 2400 nm depending on the concentration of metallic precursor in the printing solution. It was investigated whether a ZnO FET could detect NO_2 at concentrations ranging from 1 to 5 ppm using an aligned network of NWs directly printed on Pt interdigitated source/drain electrodes. The sensing capabilities of a ZnO FET at concentrations ranging from 1 to 5 ppm were tested using an aligned network of NWs printed directly on Pt sensor electrodes. A rise (fall) in NW resistance was observed after the injection of 5 ppm of NO_2 (50 ppm of ethanol) due to the target gas acting as an electron acceptor (donor) on n-type NWs. The sensor calibration curve (resistance variation vs. NO_2 concentration) was linear in the tested range. An extrapolated LoD of 53.5 ppt was calculated. In response to 5 ppm of NO_2, the response and recovery periods were 67 and 11 s, respectively.

4.4.2. SO_2 Gas Detection

Sulfur dioxide (SO_2) is a common air pollutant that can be detected using sensors. Polymeric sensing films [258–260], as well as liquid and solid electrolytes, are used to make these sensors. SO_2 gas sensors based on SnO_2 [261], SnO_2 doped Pd [262], WO_3 doped with various metals [211,263,264], and vanadium oxide modified with TiO_2 [264] were also developed and tested. During the initial detection, Berger et al. examined the interaction mechanisms between SO_2 and the SnO_2 sensor interface [261]. As a catalytic additive, SnO_2-based gas sensors contained 0.05, 0.1, 1, and 3 mol% Pd. In recent years, thick-film technology has been used to increase the operating temperatures to 600 °C [262]. The magnetron sputtering method was used to fabricate active layers of pure and Pt-doped WO_3 on a micro hotplate substrate to detect sulfur compounds (SO_2 and H_2S). A compact

tubular SO_2 sensor based on a sodium superionic conductor and V_2O_5-doped TiO_2 sensing electrode was described by Liang et al. [265].

4.4.3. H_2S Gas Detection

Due to their excellent performance in detecting hydrogen sulfide (H_2S) gas, SMOx-based gas sensors caught the attention of researchers. H_2S is a toxic gas with a threshold limit of 10 ppm, and concentrations over 250 ppm cause serious health problems, including death. Metal oxides are a model-sensitive material for H_2S sensing [266,267] and other gases [36,268] because of their high sensitivity, quick response, and ease of integration. In contrast, SMOx-based sensors have low selectivity, are highly dependent on the relative humidity, and require high operating temperatures (above 100 °C). Metal oxides (MOx) are the most commonly used substance in chemo-resistive gas sensors, both in academic and industrial settings [36,268,269]. Hexagonal WO_3 nanoparticles show the best selectivity to 10 ppm H_2S at 200 °C, according to Szilagyi and co-workers [48]. If the operating temperature drops below a certain level, the response does not occur. Interlaced and condensed WO_3 nanofibers can detect H_2S gas at ppm levels, according to Niu and co-workers [31]. WO_3 is also hindered by low selectivity or high operating temperatures when used to detect H_2S gas [270].

These materials can be combined with CPs (conducting polymers) to improve their sensing capabilities while addressing some of their flaws, such as low selectivity and high temperature [271]. MOx/CP composites already demonstrated H_2S detection from 0.05 to 1000 ppm. By lowering the temperature of the sensor, hybridization with MOx significantly improves the response quality and operating conditions of the H_2S sensor. MOxs and CPs have a delicate synergetic effect due to the entanglement of their sensing mechanisms (from CPs, MOxs, and p-n heterojunctions), as well as numerous parameters that influence their effectiveness (e.g., synthesis, deposition, and morphology). Furthermore, environmental factors and long-term stability (>1 month) were too rarely studied, even though they are crucial for sensor applications [272]. Different SMOx-based H_2S gas sensors were successfully modified using the following materials: WO_3 and WO_3-based materials [273–277], SnO_2 [229,278–281], ZnO [282,283], copper oxide [280,284,285], platinum and palladium oxides [286,287], indium oxides [287,288], silver-based materials [289,290], titanium oxide [291], and cadmium oxide [292]. In dry and wet synthetic air with varying levels of humidity, WO_3-based SMOx sensors responded strongly to H_2S. The H_2S sensitivity of some WO_3 thin-film sensors is at the ppb level. A slight increase in conductance was also observed in the presence of humidity [276]. H_2S can also be detected at room temperature by ZnO-based sensors down to 0.05 ppm [282].

4.4.4. Amine Gas Detection

In many fields, like food processing, fertilizers, chemical technology, medical diagnosis, and environmental protection, it is extremely important to detect any trace amount of ammonia/amine. WO_3 [293,294], copper-based materials [293,295], ZnO [296], SnO_2 [297], iron oxide [298], and Cr_2O_3 [299] are well-known materials for functionalizing ammonia/amine detecting sensors. To produce ZnO films doped with various amounts of RuO_2, thick films of ZnO were immersed in an aqueous solution of 0.01 M ruthenium chloride (RuO_2) [296]. At operating temperatures between 100 and 350 °C, the doped ZnO sensor was exposed to 1000 ppm NH_3. With increasing operating temperature, the response increased.

4.4.5. Hydrogen Gas Detection

Among its potential uses are automobiles, electricity generation in fuel cells, medicine, space exploration, industrial chemical production, and food production. In the event hydrogen leaks into the air from storage tanks or valves, explosive mixtures can form, making hydrogen-monitoring devices necessary. Enhanced sensitivity and selectivity to H_2 gas were demonstrated with a nanostructured SnO_2 thin film doped with silver (Ag)

and platinum (Pt). At 100 °C, nanocrystalline SnO_2 shows a fast response time (around two seconds) and a quick recovery time (around ten seconds). In addition to their high sensitivity to H_2 gas, porous SnO_2 particles have a high surface area [300]. In today's world, chemo-resistive gas sensors based on the IOT (Internet of things) are used as H_2 sensors with low power consumption and a lower temperature [301]. A potential technique for SMOx-based gas sensors is self-heating, particularly for materials with NW shapes. Self-heating gas sensors can significantly reduce their power consumption from several W to nW levels. Power consumption reductions can significantly extend the life of sensors and save a lot of energy. This can be accomplished using single, arranged, and networked NWs. However, networked NWs are simpler to synthesize than single or ordered NWs, which makes them the most popular morphology for self-heating petrol sensors. The majority of self-heating MOx materials were reported to have NW morphology. In spite of the fact that self-heated gas sensors can display power consumption in the nW range, most of these sensors have very low response values [302].

MEMS gas sensors based on SMOxs have straightforward topologies, are easy to manufacture, and consume little energy. Using MEMS gas sensors results in both a reduction in gas sensor size and a reduction in power consumption for both gas sensors and electrical devices. In terms of power consumption, MEMS-based gas sensors trail self-heated gas sensors. As a result of gas sensing measurements still requiring high temperatures, MEMS gas sensors rely on an external heater. As a result, the problem remains difficult to solve. Despite the significant advances in the development of low-power-consumption-based gas sensors, there are still several challenges and issues to overcome in order to achieve high sensitivity, selectivity, long-term stability, and quick response/recovery times.

As a H_2-sensitive medium, tungsten oxides with palladium or platinum catalysts display a color change from pale green to blue when hydrogen reduces them to tungsten bronze [295,303].

4.4.6. Volatile Organic Compound Detection

Animals and plants are both affected by volatile organic compounds (VOCs) that cause chronic diseases, such as eye irritation, throat and lung problems, and cancer in humans. Many studies were carried out on modified SMOx sensing films for the detection of atmospheric VOCs, such as ethanol, acetone, hydrocarbon, and liquefied petroleum gas (LPG). Different materials are used to modify SMOx sensors, such as SnO_2 and SnO_2-based materials [228,304–307], WO_3 and WO_3-based materials [308–310], titanium oxides [310–312], zinc oxides [310–312], iron oxides [313,314], cobalt oxides [315], cerium oxide sensors [316], and copper-based materials [317]. By adding basic metal oxides, such as lanthanum oxide (La_2O_3), ethanol gas sensors can be made more sensitive. In the presence of La_2O_3 and WO_3, ethanol gas undergoes dehydrogenation and dehydration over SnO_2-based elements, respectively [318]. SnO_2 doped with cadmium oxide (CdO) shows enhanced sensitivity to C_2H_5OH and H_2 at 300 °C with a detection limit of several ppm in air [319]. Similar to MEMS/NEMS chemo-resistive gas sensors, the IoT also enhances C_2H_5OH sensitivity at low temperatures or room temperatures because of the high surface area and reduced power consumption. VOCs, such as acetylene, LPG, and aldehyde, can be detected by modified tin-oxide-based films. HCHO was reported to be stable and sensitive in a SnO_2–NiO composite material [320]. According to Qi and co-workers, SnO_2-based sensors modified with 6 wt% Sm_2O_3 were 16.8 times more responsive to C_2H_2 than SnO_2 sensors. As an excellent C_2H_2 sensor, the Sm_2O_3-doped SnO_2-based sensor showed a high sensitivity under various humid conditions [228]. It was also demonstrated that SnO_2-based sensors can successfully detect LPG [210,306]. In_2O_3 NW FETs doped with Yb were proposed by Jun and co-workers [321]. A 4 mol% Yb-doped In_2O_3 NW FET exhibited n = 6.67 cm^2 V^{-1} s^{-1} n-type behaviour. Based on the output characteristics of VTH = 3.27 V, SVTHSW = 0.5 V dec^{-1}, and Ion/Ioff = 10^7, linear and saturation zones were assessed. Undoped In_2O_3 NW FETs exhibited n-type behavior as well, with n = 10.82 cm2 V^{-1} s^1, VTH = 10.26 V, SVTHSW = 2.5 V dec^{-1}, and Ion/Ioff = 10^3. Over the

entire test range, the calibration curve of the 4 mol% Yb-doped In_2O_3 NW FET displayed linear performance. In_2O_3 NW FETs with undoped silicon were approximately three times less sensitive [6]. The following table illustrates the gas-sensing activity of SMOx-based nanomaterials, where t_{res} corresponds to the response time and t_{rec} corresponds to the recovery time. SMOx-based gas sensors are compared in Table 2 for comparison.

Table 2. Different gas-sensing activities of SMOx-based nanomaterials.

Analyte Gas	Layer Composition	Meas. Temp.	Concentration	Response	t_{res}	t_{rec}	Selective Agents	Ref.
CO	40% In_2O_3-SnO_2	250 °C	1000 ppm	16	NA	NA	NA	[322]
	SnO_2@In_2O_3	300 °C	200 ppm	1.9	135 s	460 s	NA	[323]
	SnO_2@NiO	250 °C	500 ppm	15.9	NA	NA	CH_4	[324]
	50 wt% Co_3O_4-SnO_2	100 °C	1000 ppm	175	NA	NA	H_2	[325]
	(3 wt% ZnO-SnO_2)@ CuO	235 °C	200 ppm	13.4	NA	NA	H_2	[326]
	20 wt% WO_3-MoO_3	200 °C	15 ppm	300	2 min	2 min	NA	[248]
H_2	(3 wt% ZnO-SnO_2)@CuO	305 °C	200 ppm	16	NA	NA	CO	[326]
	SnO_2@2.6mol% ZnO	350 °C	100 ppm	18.4	NA	NA	CO, NH_3, CH_4	[327]
	(0.005 mol MoO_3)-SnO_2	240 °C	1000 ppm	10	5 s	10 s	NA	[328]
	1 wt% Co_3O_4-SnO_2	250 °C	1000 ppm	9100	NA	NA	CO	[325]
	TiO_2/NiO	200 °C	10,000 ppm	70	NA	NA	NA	[329]
	ZnO@SnO_2	400 °C	500 ppm	70	NA	NA	NA	[330]
NO_2	SnO_2@ZnO	RT	5 ppm	0.4	~50 s	~450 s	NA	[331]
	40% ZnO-SnO_2	250 °C	500 ppm	34.5	NA	NA	NA	[332]
	20% WO_2-SnO_2	200 °C	200 ppm	186	NA	NA	NA	[333]
	40% In_2O_3-SnO_2	200 °C	1000 ppm	7.5	NA	NA	NA	[322]
	5% Eu_2O_3-ZnO	300 °C	3 ppm	16	3 min	3 min	CO	[334]
H_2S	Cu_2O/SnO_2	RT	50 ppm	45	NA	NA	Toluene, LPG	[335]
	6% CuO/SnO_2	150 °C	20 ppm	4300	3 s	NA	NA	[336]
	1 mol% CeO_2-SnO_2	300 °K	5 ppm	3	40 s	20 s	LPG, EtOH, NO_x, CO	[337]
	SnO_2@ZnO	350 °C	500 ppm	2.1	NA	NA	CO, CH_4	[324]
	(5 wt% ZnO-SnO_2)@ 3.68 wt% CuO	150 °C	50 ppm	60,443	15 s	7 min	NO_x, LPG, CO_2, CH_4	[338]
	SnO_2	350 °C	50 ppm	10	NA	NA	NA	[338]
	ZnO	100 °C	100 ppm	25	NA	NA	NH_3, MeOH, EtOH,butanol, acetone, ether	[339]
NH_3	ZnO@Cr_2O_3	RT	300 ppm	13.7	25 s	75 s	LPG, CO_2, EtOH, H_2, Cl_2	[299]
	2mol%α-Fe_2O_3-ZnO	RT	0.4 ppm	10,000	20 s	20 s	TMA, EtOH, MeOH	[340]
Ethanol	$ZnSnO_3$@SnO_2	270 °C	50 ppm	27.8	1 s	1.8 s	Acetone, benzene, chloroform, MeOH, formaldehyde, CO	[341]
	5 wt% La_2O_3-SnO_2	300 °C	1000 ppm	740	20 min	20 min	NA	[318]
	50 wt% SnO_2-ZnO	300 °C	200 ppm	4.69	72 s	NA	Acetone, CO, H_2, NO_2, C_3H_8	[342]

Table 2. *Cont.*

Analyte Gas	Layer Composition	Meas. Temp.	Concentration	Response	t_{res}	t_{rec}	Selective Agents	Ref.
	1.5 mol% Fe_2O_3-SnO_2	250 °C	10 ppm	24	NA	NA	NA	[343]
	ZnO	300 °C	100 ppm	7	NA	NA	NA	[344]
	ZnO@ZnS	210 °C	1000 ppm	23	15 s	15 s	NA	[345]
	ZnO@ZnS @Graphene	210 °C	1000 ppm	38	15 s	15 s	Acetone, formaldehyde, benzene, cyclohexane	[345]
	25 wt% SnO_2-ZnO	350 °C	100 ppb	~82	NA	NA	NA	[311]
	2:8 mol CuO: ZnO	115 °C	100 ppm	96	13 s	5 s	NA	[346]
	20 wt% SnO_2-TiO_2	553 °K	200 ppm	51	10–15 s	14–20 s	NA	[347]
	ZnO-Co_3O_4	170 °C	100 ppm	46	NA	NA	NA	[348]
Ethylene	0.3 wt% WO_3-SnO_2	300 °C	6 ppm	1.7	~10 min	~10 min	NA	[349]
O_3	MoO_3-TiO_2	300 °C	100 ppb	1.7	20 s	2 min	NA	[350]
SO_2	1 mol% NiO-SnO_2	25 °C	18 ppm	0.84	4.5 min	15 min	O_2, C_3H_8, NO_x	[351]
LPG	ZnO@0.47 wt% Cr_2O_3	350 °C	100 ppm	46	18 s	42 s	NH_3, CO_2, EtOH, H_2,	[352]
TMA	10 wt% ZnO-SnO_2	330 °C	50 ppm	126	2 s	5 s	NH_3, DMA, MA, EtOH, MeOH, Acetone	[353]

5. Chemical Sensing Applications

Chemical sensors convert chemical reactions into electrical, optical, or mechanical signals by using chemical-responsive layers. Chemical sensors are more specific than physical sensors because of their chemical-responsive layers. In order for these sensors to respond, a chemical-selective layer must interact with the target chemical, changing the transducer properties and resulting in a signal. Conductometric chemical sensors based on SMOx were previously reported. As part of this development, MOx was discovered to react with the surrounding atmosphere, and the first commercial gas sensor was developed [144,354,355]. Their low cost, simple preparation, and simple operation make SMOx-based chemical sensors a promising technology. Chemical sensors were classified by IUPAC in 1991 (Figure 18). A chemical sensor is a device that converts chemical information, such as the concentration of a specific chemical component or a composite, into useful analytical information [165].

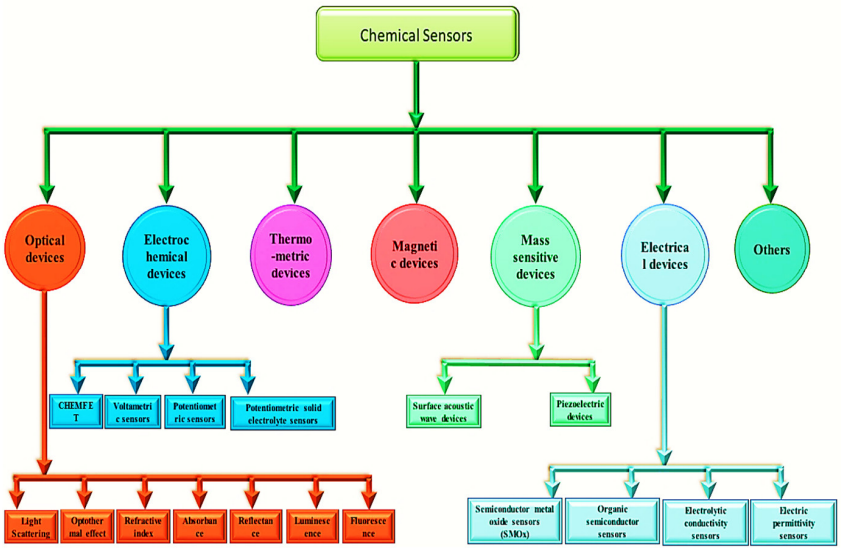

Figure 18. Schematic view of the classification of chemical sensors according to IUPAC [165].

Chemical sensors have improved the detection and quantification of various chemical substances. Medical, agricultural, industrial, and military applications are all possible with these sensors.

As illustrated in Figure 19, chemical sensors convert chemical information into quantitative or qualitative analytical signals through chemical interactions between the analyte gas or liquid and the sensor. Electric sensors produce signals through the exchange of electrons, which are electronic in nature. A chemical sensor consists of a physical transducer and a chemical-sensitive recognition layer. Stability, sensitivity, selectivity, response time, recovery, and saturation characterize them [155]. Due to their high sensitivity, compatibility with ambient conditions, and ease of fabrication, semiconductor metal oxides (SMOxs) are widely used as chemical sensing materials [163,356,357]. By exposing a metal oxide to elevated temperatures, the MOx reacts with surrounding gases, changing the surface potential and resistivity of the material.

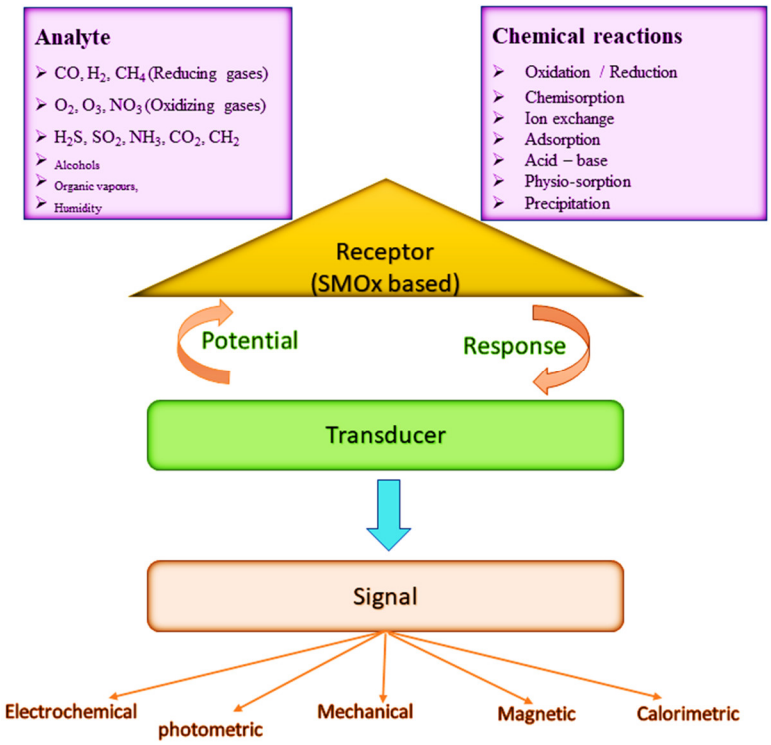

Figure 19. Schematic view of the principle of chemical sensors.

Based on the MOx materials used for specific target species, SMOx-based chemical sensors are categorized.

5.1. SnO_2-Based Chemical Sensors

SnO_2 is a highly sensitive and fast-responding material that is widely used as a chemical sensor. Various morphologies are available, including nanowires, hollow spheres, nanocrystals, and others, each with its own unique sensing properties. Wang and coworkers reported that nanowires based on SnO_2 were highly effective at detecting H_2 at concentrations between 10 and 100 parts per million [358]. In addition, SnO_2 nanowires, hollow nanospheres [359,360], nanocrystals [361], and nanocrystalline porous SnO_2 [362] exhibit CO-, NO_2-, and H_2-sensing abilities. Hierarchical three-dimensional SnO_2 nanospheres also exhibit excellent resistance to CO, methane, methanol, and ethanol [363]. Furthermore, SnO_2 nano polyhedrons are highly sensitive to methanol, ethanol, and acetone, as well as highly selective to acetone, with a fast response and recovery time (only several seconds for target gas concentrations up to 200 parts per million) [364].

SnO_2 is modified via doping and composite formation to enhance its sensing activity. In turn, this results in the development of highly sensitive and fast-responding SnO_2-based composites, like polypyrrole-coated SnO_2 hollow spheres, for the detection of ammonia [365]. Due to an increased concentration of oxygen vacancies on the surface of SnO_2 nanowires at low temperatures, plasma-modified SnO_2 nanowires [366] and Pt@SnO_2 nanorods [367] displayed high sensitivity to ethanol gas. Adding Pt to SnO_2 nanowires also enhances their chemical and electrical properties. For the detection of H_2 gas (5 ppm) at 320 °C, Wang and co-workers synthesized hetero-junction p-NiO/n-SnO_2 nanofiber-based sensors, which have excellent sensitivity and fast response recovery. Cu-doped SnO_2 and the adsorption properties of H_2S on the surface of SnO_2 were investigated by Wei et al. [368]. Pd-doped SnO_2-based CO gas sensors were recently described by Li et al. [369].

5.2. ZnO-Based Chemical Sensors

Since they are easy to synthesize and have unique optical, electrical, and chemical properties, ZnO-based chemical sensors have received considerable attention. Using ZnO material, Hahn and co-workers fabricated hydrazine electrochemical sensors (Figure 20) [370]. Detection limits of 0.2 mM were achieved with this sensor's high sensitivity (8.56 mA mM^{-1} cm^{-2}) and low response time (less than 5 s). ZnO nanorods and high aspect ratio ZnO nanowires were also used by these researchers to fabricate hydrazine sensors.

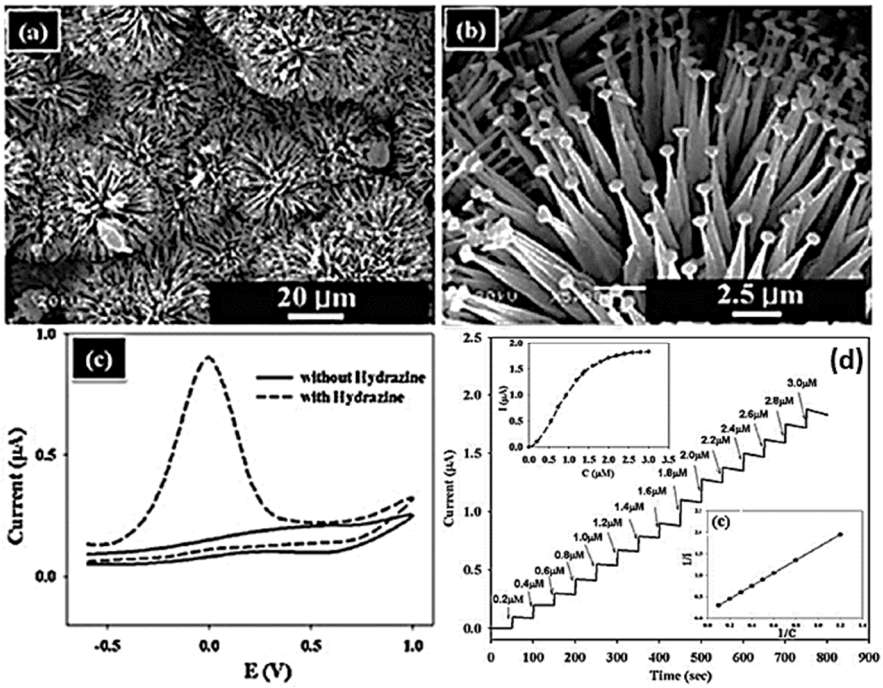

Figure 20. SEM images of ZnO material at (**a**) low magnification and (**b**) high magnification. (**c**) Cyclic voltammetry curve of a Nafion/ZnO/Au electrode in the absence of hydrazine (solid line) and presence of 1 mM N_2H_4 (dashed line) in 0.01 M phosphate − buffered saline (PBS) (pH = 7.4). The scan rate was 100 mV s^{-1}. (**d**) Amperometric response of a Nafion/ZnO/Au electrode in the presence of hydrazine. The inset shows the 1/i versus 1/C plot [370].

The electrical characteristics of aligned ZnO nanorod arrays (NRAs) were also described by Hahn and co-workers (Figure 21) [371]. H_2 was detected using ZnO NRAs. ZnO NRAs became more sensitive as the H_2 concentration increased. Chemical sensors based on ZnO nanowires were also used to detect multiple gases at room temperature, including H_2, NH_3, i-butane, and CH_4.

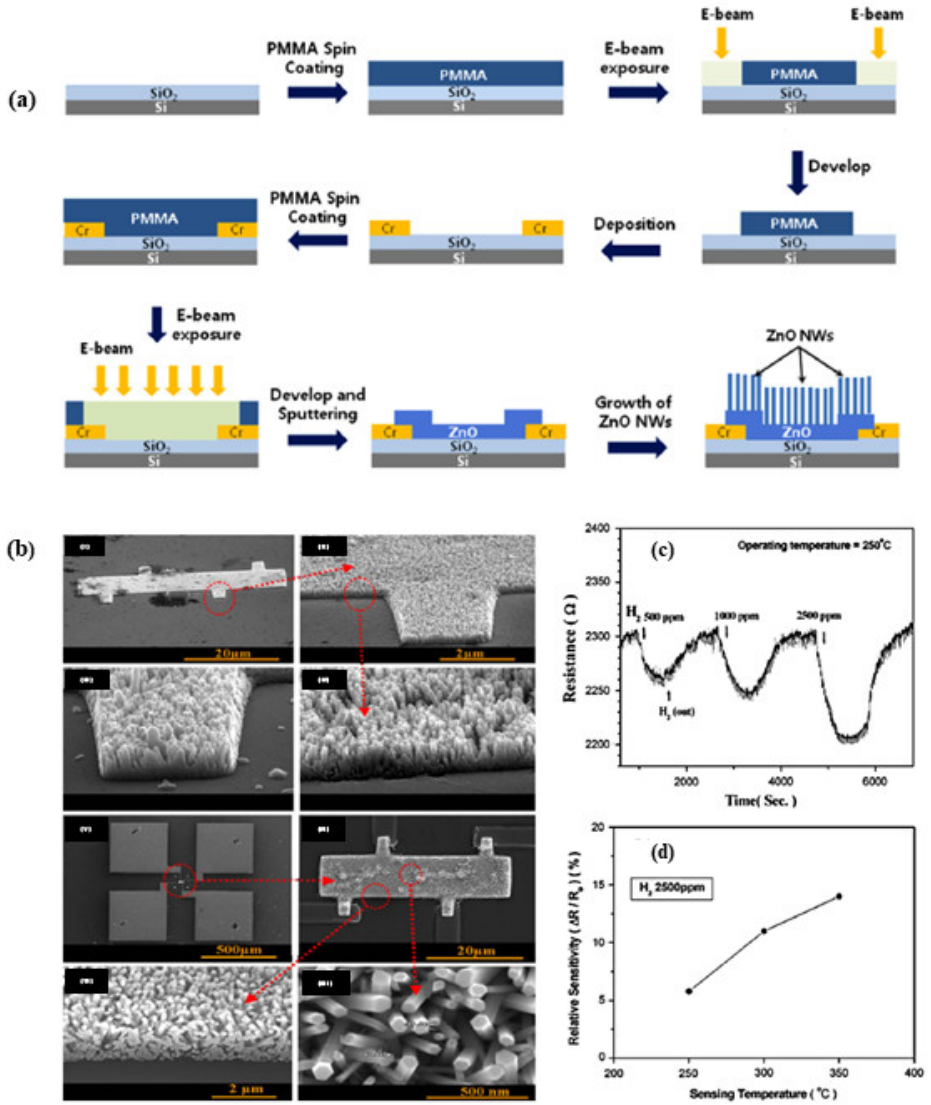

Figure 21. (**a**) Schematic view of the fabrication process of the electrode; (**b**) (i–iv) field emission scanning electron microscopy (FESEM) images of ZnO nanorod arrays (grown without electrode) and (v–viii) ZnO nanorod arrays grown directly on the probe; (**c**) dynamic responses of ZnO nanorod arrays to H_2 pulses at 250 °C; (**d**) demonstration of the sensitivity at various temperatures [371].

As shown in Figure 22a [372], Li and colleagues synthesized co-doped ZnO nanorods on ITO substrates at low temperatures. As shown in Figure 22b, these nanorods responded rapidly to varying CO concentrations. In this study, co-doped ZnO sensors performed better than pristine undoped ZnO sensors. By attaching impurities to SMOx-based semiconductors, the sensing properties were greatly enhanced. Pd nanodots were incorporated into ZnO nanowires by Choi and Kim, which enhanced the CO sensitivity. A combination of electronic and chemical sensitization could be responsible for this enhanced sensitivity [373].

5.3. Other SMOx-Based Chemical Sensors

Chemical sensors rely heavily on selectivity. There is a slight deficiency of oxygen and incomplete crystallinity in gallium oxide (Ga_2O_3), which are preferred for high-temperature sensing applications, such as chemical, environmental, and explosive gas sensing [374]. Gallium oxide is chemically and thermally stable with low cross-sensitivity to humidity. The use of mesoporous single-crystal Ga_2O_3 nanoplates for CO detection was described by Yan and co-workers [375].

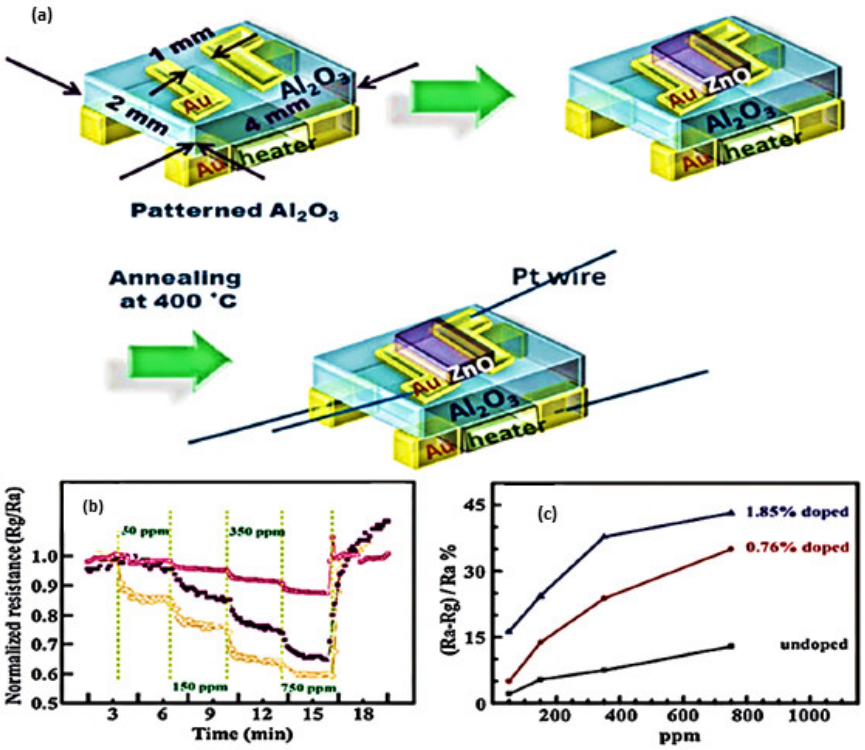

Figure 22. (**a**) Schematic view of the fabrication of a SMOx-based chemical sensor; (**b**) time-dependent resistance for continuous exposure of the sensor to CO at 350 °C; (**c**) sensitivity of undoped and 0.76% and 1.85% co-doped ZnO sensors exposed to different concentrations of CO [372].

Using $CoCl_2$ and urea precursors, crystalline mesoporous Co_3O_4 nanorod-based sensors were fabricated via facile hydrothermal methods. Benzene, acetone, and ethanol were detected using the sensor. In addition to its excellent stability, high sensitivity, rapid response, and recovery time, the SMOx-based sensor was particularly sensitive to acetone (Figure 23) [376]. The ethanol sensitivity of Fe_2O_3–TiO_2 tube-like nanostructures was also improved [377]. In_2O_3-based chemical sensors were used to detect NH_3, CO, H_2S, NOx, ethanol, formaldehyde, and alcohol [378–385]. In Table 3, we present a comparative analysis of SMOx-based chemical sensors.

Table 3. Different SMOx-based chemical sensors.

SMOx Composite Materials	Analyte Gas	Detection Limit (Conc.)	Senor Response/ Temperature	Response/Recovery Time	References
SnO_2 nanowire	H_2	10 ppm	~0.4/300 °C	N/A	[358]
SnO_2 hollow sphere	CO	50 ppm	-/300–350 °C	<1 min./30 min.	[360]
SnO_2 nanocrystals	NO_2	100 ppb	-/300 °C	N/A	[361]
SnO_2 porous NPs	H_2/CO	160/200 ppm	-/300 °C	NA	[362]
SnO_2 flower-like	CO	50 ppm	~2.13/350 °C	26 s/34 s	[362]
SnO_2 nanorods	H_2	100 ppm	~13/150 °C	N/A	[386]
Plasma-modified SnO_2 nanowire	Ethanol	100 ppm	-/250 °C	N/A	[366]
Pt@SnO_2 nanorods	Ethanol	10 ppm	3.7/300 °C	2 s/20 s	[367]
NiO-SnO_2 nanofibers	Ethanol	100 ppm	25.5/300 °C	2 s/3 s	[387]
p-NiO/n-SnO_2 heterojunction composite nanofibers	H_2	100 ppm	13.6/320 °C	~3 S/~3 S	[388]
ZnO nanorods	Ethanol	1 ppb	~10/300 °C	100 s/-	[389]
ZnO nanorod arrays	H_2	500 ppm	-/250 °C	6 min/17 min	[390,391]
ZnO nanowire	NO_2	0.5 ppm	-/225 °C	N/A	[392]

Table 3. *Cont.*

SMOx Composite Materials	Analyte Gas	Detection Limit (Conc.)	Senor Response/ Temperature	Response/Recovery Time	References
Pt adsorbed single crystalline ZnO nanowires	NH_3	1000 ppm	-/350 °C	100 s/100 s	[393]
Co-doped ZnO nanorods	CO	50 ppm	-/350 °C	N/A	[372]
Pd nanodots–functionalized ZnO nanowire	CO	100 ppb	1.02/20 °C	120 s/180 s	[373]
Ga_2O_3 nanowire	O_2	1% O2	4.75/300 °C	N/A	[394]
NiO nanotubes	Ethanol	200 ppm	22.6/250 °C	N/A	[395]
α-Fe_2O_3 hollow spheres	Ethanol	10 ppm	~5/RT	N/A	[396]
Fe_2TiO_5/α-Fe_2O_3 nanocomposite	Ethanol	10 ppm	~10/320 °C	28 s/21 s	[397]
Fe_2O_3–TiO_2 tube-like nanostructures	Ethanol	500 ppm	8.2/270 °C	N/A	[377]
In_2O_3 nanofibers	Ethanol	100 ppm	~14/300 °C	1 s/5 s	[378]
In_2O_3 nanoparticles	NO_x	200 ppm	~10,000/150 °C	N/A	[379]
Sn-doped In_2O_3 nanopowders	CO	50 ppm	4/250 °C	N/A	[380]
In_2O_3 hollow microspheres	Ethanol	100 ppm	137.2/400 °C	N/A	[381]
Ag-doped In_2O_3 nanoparticles	Alcohol vapors	100 ppm	-/150 °C	42 s/34 s	[383]
In_2O_3 nanorods	Formaldehyde	32 ppm	-/300 °C	276 s/65 s	[384]
Mesoporous In_2O_3 nanorods	Ethanol	500 ppb	1.71/290 °C	6 s/8 s	[385]
Pt/In_2O_3 nanofibers	H_2S	600 ppm	1490/200 °C	60 s/120 s	[398]
CuO nanoribbons	Methanol	5 ppm	~1.4/RT	2–4 s/3–7 s	[399]
Porous CuO nanowire	H_2	6% H_2	407%/250 °C	72 s/156 s	[400]
Co_3O_4 hollow spheres	Butanol	10 ppm	3/100 °C	1–3 s/4–8 s	[401]
WO_3 nanowires	H_2S	1 ppm	48/250 °C	-	[273]
WO_3 nanoplates	Ethanol	10 ppm	~1.9/300 °C	-	[402]

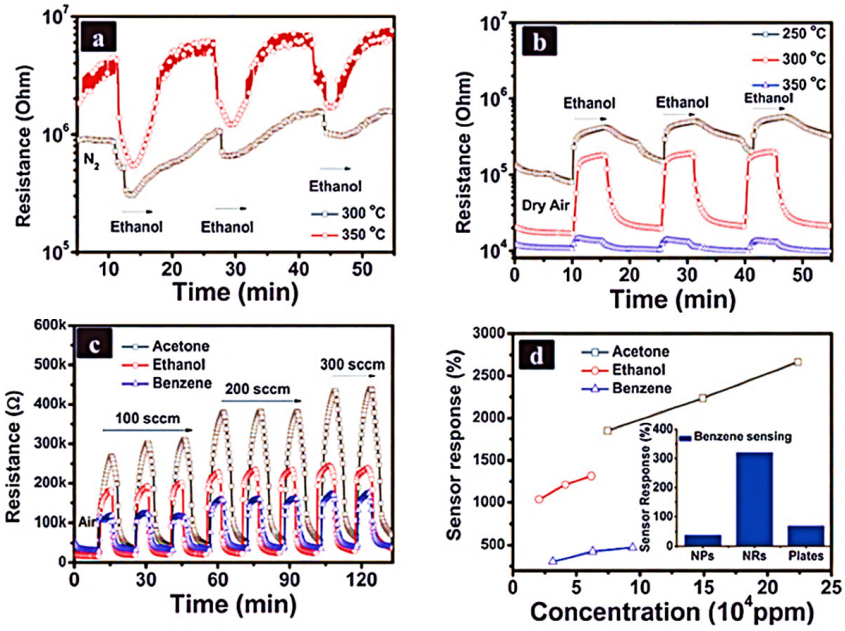

Figure 23. Gas-sensing performance of meso- and macroporous Co_3O_4 nanorod-based sensors. (**a**) ethanol sensing at different temperatures using N_2 as the reference. (**b**) Ethanol sensing at different temperatures using dry air as the reference. (**c**) gas-sensing property of porous Co_3O_4 nanorods to acetone, ethanol, and benzene at 300 °C. The sensor resistance changes in response to different concentrations of acetone, ethanol, and benzene. (**d**) Response of nanoparticles (NPs), meso-/macroporous nanorods (NRs), and porous plates to different concentrations of acetone, ethanol, and benzene [376].

6. Biosensing Applications

Because of their exceptional electrical properties, high electron mobility, excellent chemical resistance in liquids, transparency, and ease of fabrication, semiconductor metal oxide (SMOx)-based thin-film transistors (TFTs) are widely used in liquid crystal displays (LCDs), biosensors, and photosensors [403–408]. SMOx-based biosensors are highly effective at recording and communicating biomolecule progression statistics [409]. Its versatile morphology [410], chemical stability [411], physicochemical interfacial properties [412,413], light excitation, and ability to form composite structures [412] make SMOx materials potential candidates for biosensors. Electrochemically sensitive materials, such as TiO_2 [414], WO_3 [415], SnO_2 [416], and ZnO [417], are suitable for enzyme-based biosensors. In addition, these SMOx materials require a cost-effective synthesis procedure, including co-precipitation [416], chemical precipitation [418] thermal oxidation [419], chemical etching [420], polyol [421], hydrothermal [422], sol-gel [423], and sonochemistry [424], which allows for the formation of different architectural morphologies, including porous quasi-nanospheres [425], hollow nanospheres [426], nanorods [427], nanosheets [428], and flower-shaped particles. Additionally, SMOx materials can be combined with other materials to form heterostructures [429] hybrid structures [430], and composite structures [431]. Their advanced electrochemical properties make them ideal for specific biosensor applications. Biosensors require a sensing layer that reacts with a biomolecule, and this reaction is converted into optical, electrochemical, electrical, or other physical signals (Figure 24).

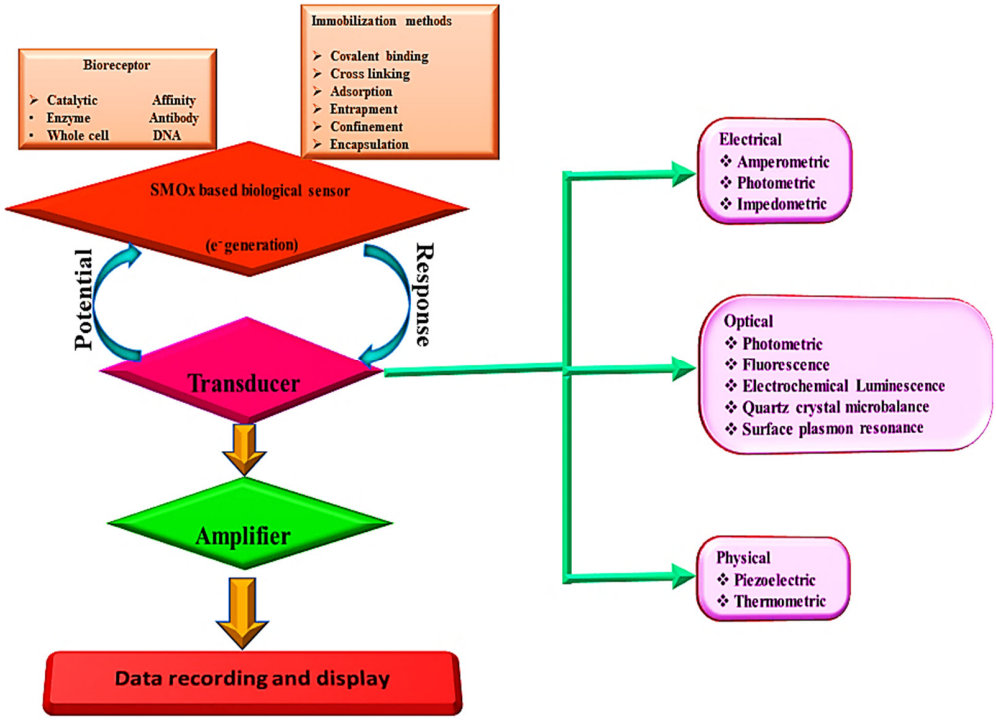

Figure 24. Schematic view of the principle of a biosensor.

For clinical diagnostics and personalized care, biosensors must be sensitive. There are several reasons why nanostructured SMOx materials have excellent sensing capabilities: (1) their increased surface-area-to-volume ratio enhances sensitivity to small analytes, as their size becomes comparable to the SMOx materials [432,433] (2) direct electron transfer enables increased sensitivity and heightened detection limit [434]; and (3) nanostructured particles close to the Debye length, which increases their sensitivity [219]. SMOx surfaces are typically attached to biomolecules via physical adsorption, entrapment, crosslinking, covalent coupling, or encapsulation. In a biocompatible environment, such interactions form a nano–bio interface that is highly stable and preserves the biomolecules. Through the

coupling of biomolecules with a bio-recognition layer, selectivity was achieved. A wearable biosensor continuously monitors physiological signals, collects sensor data, wirelessly transmits the data, and analyzes it in real time. Wearable biosensors have several advantages, including rapid continuous monitoring, detection of transient phenomena, ease of use, and accuracy. Following are a few promising nano-structured SMOx-based biosensors. Enzymes and other biomolecules are immobilized on the surfaces of these biosensors.

6.1. Enzyme-Immobilized Biosensors

Figure 25 illustrates the energy band diagram and crystal structure of different types of SMOx biosensors [435,436]. SMOx properties can be modulated by combining them with other metal nanoparticles or ions. The morphologies of SMOx materials include rods, stars, flowers, cones, and porous or dense films.

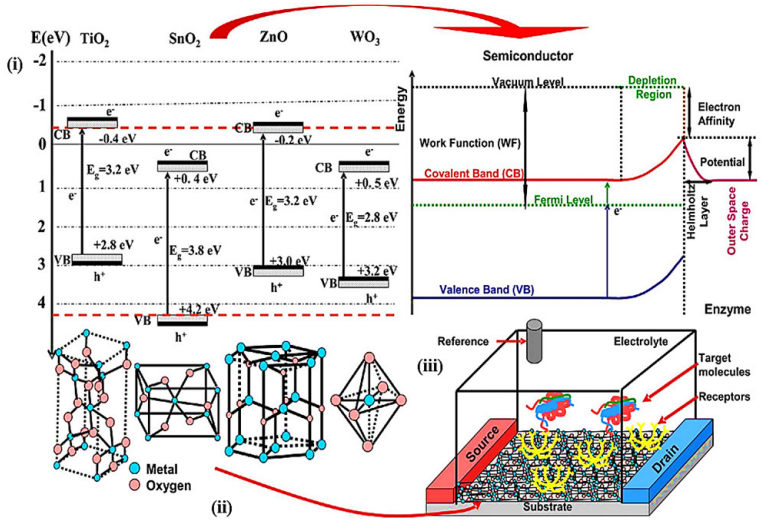

Figure 25. Mechanism of SMOx—based enzyme biosensors in three steps: (**i**) band energies; (**ii**) crystalline structure; (**iii**) configuration of an enzyme biosensor [32].

6.1.1. Glucose-Oxidase-Immobilized Biosensors

Due to a SMOx's high isoelectric point, glucose oxidase (GOx) with a low IEP of around 4.2 could be immobilized [437]. SMOx nanostructures and biopolymer composites also improved glucose biosensor activity. ZnO nanostructures have a high IEP (around 9.5), resulting in fast electron transfer rates and high enzyme loading activity [438–440]. An electrospun ZnO nanofiber glucose sensor exhibited a high and reproducible sensitivity of around 70.2 $mAmM^{-1}$ cm^{-2} for glucose at 20–85 °C (Figure 26) [438].

On a glassy carbon electrode (GCE), Fang et al. synthesized Nafion/GOx/ZnO hollow nanosphere composites. Since hollow nanosphere ZnO and GOx were adsorbed on the surface of the sensor [441,442], it exhibited high sensitivity (65.82 mA mM^{-1} cm^{-2}) and fast response time (5 s). The authors reported direct electron transfer at a rate of 0.67 s^{-1} in glucose biosensors fabricated with GOx-immobilized ZnO/Cu nanocomposites [442]. There has been a surge in the development of wearable biosensors for the non-invasive monitoring of blood glucose. Field-effect transistors (FETs) based on SMOx gained attention in this area [443–447]. An electrochemical biosensor based on a FET coated with In_2O_3 3.5 nm thick is shown in Figure 27. To monitor glucose levels in tears, this FET-based device was decorated with glucose oxidase [448]. Blood glucose concentrations are 70–180 mg/dL in a healthy individual, while tears contain 3–15 mg/dL glucose [448,449]. Through an ultra-thin In_2O_3 FET, the biosensor in Figure 27 could detect ultralow glucose concentrations in tears.

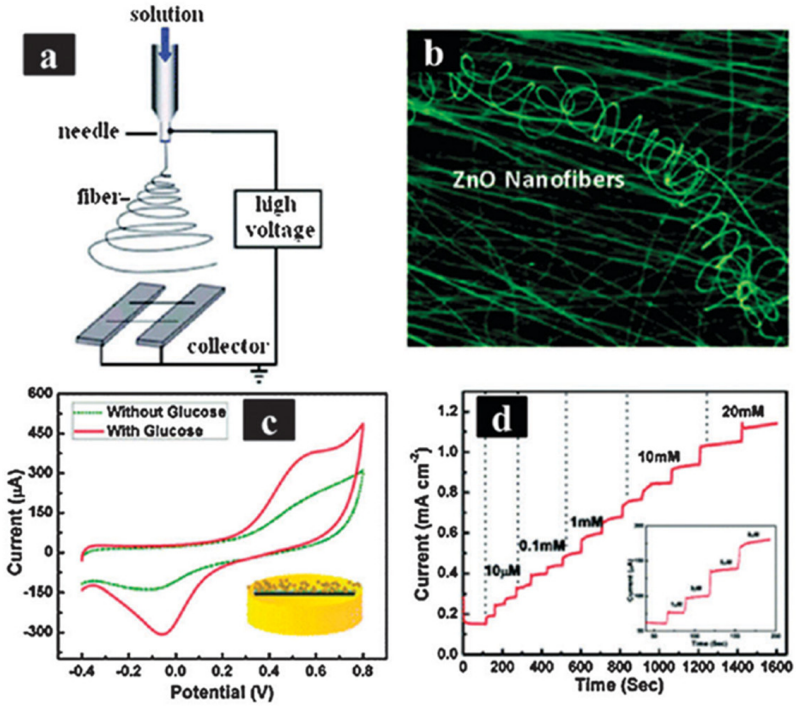

Figure 26. (**a**) Fabrication of zinc oxide nanoflowers; (**b**) SEM image of ZnO nanofibers; (**c**) cyclic voltammetry curves for a modified gold electrode without and with 100 mM glucose in PBS solution (pH = 7.0); (**d**) amperometric response of the ZnO nanoflower biosensor in different concentrations of glucose at 0.8 V in PBS solution (at pH = 7.0) [438].

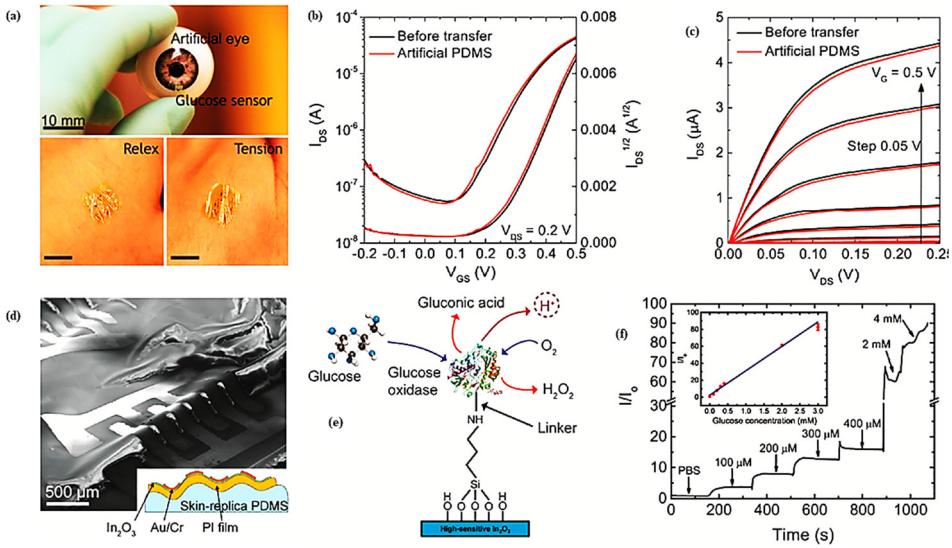

Figure 27. In_2O_3 FET− based biosensor. (**a**) Images of a contacted device on an artificial eye for glucose sensing in tears. Thin-film sensor contact with the skin during tension and relaxation; (**b**,**c**) device performance of thin-film In_2O_3 on a rigid substrate and flexible artificial PDMS skin, with the transfer of In_2O_3 FETs to replicas of skin under liquid gating with PBS solution at low voltage; (**d**) SEM image of In_2O_3 FET device on artificial PDMS skin replica; (**e**) enzymatic oxidation of D−glucose to generate gluconic acid and H_2O_2; (**f**) representation of In_2O_3 sensors for the concentration of D-glucose in a low range of human diabetic tears and high range of blood, with the standard deviation shown in the inset [448].

6.1.2. Cholesterol-Oxidase-Immobilized Biosensors

In order to fabricate an efficient and reliable cholesterol biosensor, SMOx was immobilized and stabilized with cholesterol oxidase (ChOx). This table outlines cholesterol biosensors constructed with different types of nanostructured modified electrodes [434,450]. At a low temperature, the Hahn group immobilized cholesterol oxidase on well-crystallized ZnO nanoflowers [434] and ZnO nanoparticles (NPs) [451]. It was shown that these biosensors had high reproducible sensitivity, a low detection limit, and a very fast response time (<5 s). ZnO nanofilms [452] and nano porous ZnO thin films [453] were also employed to fabricate cholesterol biosensors, which enhanced the electron transfer between cholesterol oxidase and electrodes. Composites, including platinum–gold-functionalized ZnO nanorods [454] and Pt-incorporated ZnO nanospheres [455], improved the sensitivity with low Km values. For the first time, Hahn et al. fabricated controlled ZnO nanorods directly on a silver electrode at 90 °C (Figure 28) [456]. The loaded cholesterol oxidase surface area of Malhotra and coworkers increased the electron transport between ChOx and the electrode, resulting in improved sensitivity [457]. SnO_2 nanoparticles and chitosan composite films were developed by Ansari and co-workers for enhanced cholesterol adsorption [458]. A CH-SnO_2/ITO nanocomposite was synthesized to improve the electrocatalytic activity and biocompatibility. SMOx-based highly-sensitive cholesterol biosensors were also developed using co-oxidase [459] and Fe_3O_4 nanoparticles [450].

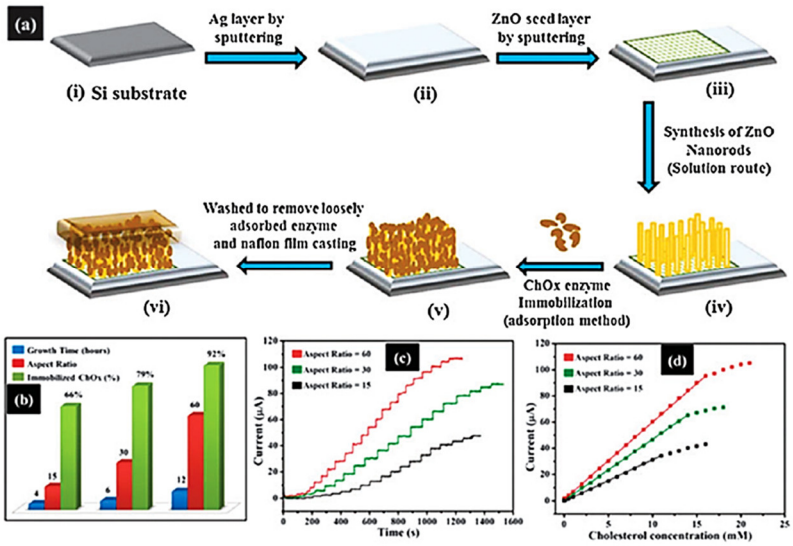

Figure 28. (**a**) Fabrication process flow for a cholesterol biosensor (i–vi); (**b**) relationship between the enzyme loading, the aspect ratio of ZnO nanorods, and growth time; (**c**) amperometric responses at an applied potential of +0.38 V for different aspect ratios of ZnO nanorods in the presence of cholesterol; (**d**) calibration curves of current response versus cholesterol concentration [456].

6.1.3. Urea- and Glutamate-Immobilized Biosensors

A urea biosensor based on ZnO nanowire arrays immobilized with urease (Urs) by Ali and co-workers had a sensitivity of about 52.8 mV per decade with linear response ranges (0.1–100 mM) [460]. Their bioelectrode also displayed a low response time (25 s), wide linear range (8 mM^{-3} mM), low detection limit (5.0 mM), and excellent stability [461]. Furthermore, Urs and glutamate dehydrogenase (GLDH) were combined to form a nanocomposite film on superparamagnetic Fe_3O_4 nanoparticles and chitosan that demonstrated a low Km value (0.56 mM) [462]. Nanostructured ZnO composites containing Urs and GLDH were reported to have a high sensitivity and a low detection limit of 13.5 mg dL^{-1}, with a Km value of 6.1 mg dL^{-1} [463].

6.1.4. Lipase-Immobilized Biosensors

It is also possible to form SMOx biosensors by immobilizing lipases. Solanki et al. describe a nanostructured cerium oxide film (35 nm) for lipase immobilization. With a linear range of 50–500 mg dL^{-1} and a detection limit of around 32.8 mg dL^{-1} at a low Km value (22.27 mg dL^{-1}), the film exhibited a high affinity for tributyrin [464].

6.1.5. Other Enzyme-Immobilized Biosensors

The TiO_2 nanoneedle film immobilized with cytochrome complex (cyt c) described by Luo et al. facilitated electron transfer between redox enzymes and electrodes [465]. Their goal was to improve the enzyme activity against H_2O_2 released from human liver cancer cells. The detection of choline was achieved by electrochemically depositing MnO_2 nanoparticles and nanowires, along with CH hydrogel and choline oxidase on GCE. MnO_2 effectively trapped the target analyte on the electrode surface because of its large specific area. The linear detection range for α-MnO_2 nanoparticles was 2.0–580 mM choline, while the linear detection range for β-MnO_2 nanowires was 1.0–790 mM choline. In addition, an electro-chemiluminescence (ECL) lactate biosensor was made from nano-hybrids of ZnO-multiwalled carbon nanotubes (MWCNTs) modified with lactate oxidase and Nafion. Human blood plasma samples were tested using this ECL lactate biosensor.

6.2. Nucleic-Acid-Immobilized Biosensors

For DNA detection, SMOx materials are immobilized with nucleic acids (Table 4) [466–470]. Among the applications of these DNA biosensors are disease detection, genetic disorder screening, drug discovery, and forensics [471]. For the detection of acute promyelocytic leukemia, Zhang et al. immobilized single-stranded DNA sequences of 18-mer PML/RARA oligonucleotides on a carbon ionic liquid electrode modified with nanosized ZnO. The detection range was 1×10^{-8} to 1×10^{-12} M, with a detection limit of 2.5×10^{-13} M [467]. A ZnO-nanowire-based DNA biosensor made with multiwalled carbon nanotubes (MWCNTs) and gold nanoparticles was described by Wang et al. Sequence-specific target DNA can be detected using this biosensor. A single-stranded DNA probe with a thiol group at the end (HS-ssDNA) was covalently immobilized on the Au nanoparticle surface. A DNA biosensor based on $[Ru(NH_3)_6]^{3+}$ as an intercalator [466] was capable of quantitatively detecting DNA in the range of 1.0×10^{-13} to 1.0×10^{-7} M. The 21-mer ssDNA of Mycobacterium tuberculosis was immobilized on a nano-ZrO_2 film electrochemically deposited on a gold surface. With a detection limit of 65 mg mL^{-1} [472], this biosensor showed rapid diagnosis within 60 s. The biosensor was developed via a V_2O_5 nanobelt, MWCNTs, and chitosan nanocomposite material that was modified onto a carbon ionic liquid electrode (CILE) and immobilized with ssDNA for Yersinia enterocolitica detection. The biosensor detected complementary DNA at concentrations between 0.01 and 1.000 nM, with a detection limit of 1.76 pM [473].

6.3. Antibody-Immobilized Biosensors

Immunosensor sensitivity and stability were affected by the orientation, surface density, and antigen-binding efficiency of antibodies when immobilized onto functionalized surfaces. A model antibody–antigen system that represents the complex matrix immuno sensors encountered in reality was used to improve various surface functionalization processes and assess their effectiveness. Protein A/G enhanced antibody loading on surfaces substantially more than boronate ester chemistry. In spite of the fact that both enhance antigen binding by assisting in orientation-specific immobilization of antibodies, using protein A/G enhanced the antibody surface density, which is crucial to obtaining maximum antigen recognition [474,475].

In immunoassays, electrochemical immunosensors are used to detect antigens, antibodies, or other biochemical targets related to health issues, such as cancer antigens in serum and bacteria in food [476]. A CH-MnO_2/MWNT-Ag composite impregnated with anti-AFP was electrodeposited on a CH-MnO_2/MWNT-Ag composite developed by Che

and co-workers [477]. Because of the high surface area and conductivity of the MWCNT-Ag, the detection range for AFP was 0.25–250 ng mL^{-1}. Anti-AFP antibody immobilization on a ZnO/PAC nanowire FET allows for real-time, label-free detection of liver cancer markers (Figure 29) [478]. In addition, it was demonstrated that the biosensor could be used as a pH sensor. In an electrochemical immune sensor, Wei and his team utilized dumbbell-like Au–Fe_3O_4 nanoparticles for detecting prostate-specific antigen (PSA), which is a cancer biomarker. PSA detection was achieved by immobilizing primary anti-PSA antibodies on graphene and secondary antibodies on Au–Fe_3O_4 nanoparticles [479]. The immune sensor has a wide linear range of detection (0.01–10 ng mL^{-1}), a low detection limit (5 pg mL^{-1}), and excellent reproducibility and stability.

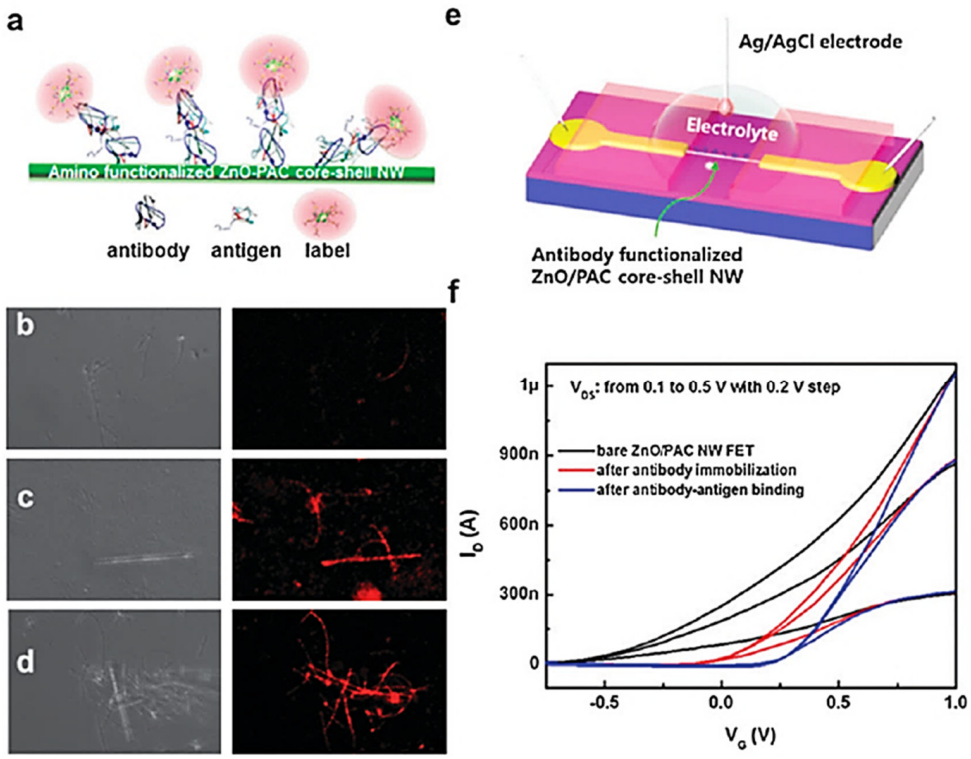

Figure 29. Electrical characterization of amino-functionalized ZnO/PAC nanowires for AFP detection. (**a**) Schematic view of anti−AFP immobilization via the sandwich binding method. The anti-AFP antibody was labeled with TRITC. Fluorescence microscopy images of an (**b**) untreated ZnO/PAC nanowire with AFP antigen, (**c**) an amino-functionalized ZnO/PAC nanowire with AFP antigen, and (**d**) an amino-functionalized ZnO/PAC nanowire with liver carcinoma. (**e**) Schematic view of an electrolyte-gated ZnO/PAC nanowire-based FET. (**f**) Current versus potential graph of a ZnO/PAC nanowire-based FET for sequential immobilizations [478].

6.4. Other Biomaterial-Immobilized Biosensors

Graham and coworkers demonstrated the fabrication of a SMOx-based bioelectrode for on-chip, long-term, and noninvasive cell culture assays and label-free high-content screening. In addition to detecting the fast electrical activity of neurons, the bioelectrode detected slow changes in impedance as the cells grew and divided. The team showed that a silver- and TiO_2-based biosensor could be used to analyze prokaryotic gene expression in real time [480] Table 4 compares SMOx-based biosensors.

Table 4. SMOx-based immobilized biosensors.

Target Biomolecule	Electrode	Sensitivity	Detection Limit (mM)	Linear Range (mM)	Response Time (s)/ Potential (V)	Ref.
Glucose	GCE/ZnO NF/PVA/GOx/L-Cys	70.2 mA mM^{-1} cm^{-2}	1	0.25–19	<4/+0.80	[438]
	GCE/ZnO-HNSPs/GOx/Nafion	65.82 mA mM^{-1} cm^{-2}	1	0.005–13.15	<5/+0.8	[441]
	GCE/ZnO NRs/GOx/CHIT	25.7 mA mM^{-1} cm^{-2}	10	0.01–0.25/0.3–0.7	<2/+0.8	[481]
	Au/ZnO NT/GOx/Nafion	21.7 mA mM^{-1} cm^{-2}	1	0.05–12.0	3/+0.8	[482]
	Au/ZnO nano-tetrapods/GOx/Nafion	25.3 mA mM^{-1} cm^{-2}	4	0.005–6.5	<6/+0.8	[483]
	ITO/ZnO NT arrays/GOx/Nafion	30.85 mA mM^{-1} cm^{-2}	10	0.01–4.2	<6/+0.80	[484]
	PET/Au/ZnO-NWs/GOx/Nafion	19.5 mA mM^{-1} cm^{-2}	<50	0.2–2.0	<5/+0.80	[485]
	PDDA/GOx/ZnO/MWNTs	50.2 mA mM^{-1} cm^{-2}	0.25	0.1–16	–/–	[486]
	ITO/Cu/ZnO/HRP-GOx/Con A/CS-Au	0.097 mA mM^{-1} cm^{-2}	40	1.0–15.0	<6/−0.39	[442]
	GCE/porous TiO_2/GOx/Nafion	0.3 mA mM^{-1} cm^{-2}	-	0.15–1.2	<10/−0.45	[487]
	GCE/TiO_2-GR/GOx	6.2 mA mM^{-1} cm^{-2}	-	0–8.0	–/−0.60	[488]
	Au/CuO/GOx/Nafion	47.19 mA mM^{-1} cm^{-2}	1.37	0.01–10.0	<5/-	[489]
	ITO/CeO_2 NRs/GOx	0.165 mA mM^{-1} cm^{-2}	100	2.0–26.0	1–2/+0.80	[490]
	Pt/GOx/Fe_3O_4/Chitosan/Nafion	11.54 mA mM^{-1} cm^{-2}	6	0.006–2.2	–/–	[491]
	Au/MgO/GOx/Nafion	31.6 mA mM^{-1} cm^{-2}	0.068	0.001–0.009	<5/	[492]
	Pt/NiO doped ZnONRs/GOx	61.78 mA mM^{-1} cm^{-2}	2.5	0.5–8.0	<5/+0.39	[439]
	GCE/NiO/GOx/CHIT	3.43 mA mM^{-1} cm^{-2}	47	1.5–7	<8/+0.	[440]
Cholesterol	Au/flower-shaped ZnO/ChOx/Nafion	61.7 mA mM^{-1} cm^{2}	0.012	1.0–15.0	<5/-	[434]
	Au/ZnO NPs/ChOx/Nafion	23.7 mA mM^{-1} cm^{2}	0.00037	0.001–0.5	<5/+0.355	[493]
	Ag/ZnO/ChOx	35.2 mV per decade	-	0.001–10.0	–/–	[494]
	ITO/NS-CeO_2/ChOx	2 mA mg dL^{-1} cm^{2}	-	0.26–10.36	~15/+0.50	[495]
	ITO/CH-SnO_2/ChOx	34.7 mA mg dL^{-1} cm^{2}	130	0.26–10.36	0.5/-	[458]
	ITO/NanoFe_3O_4/ChOx	86 Ω mg^{-1} dL cm^{-2}	6.5	0.0065–10.36	25/+0.06	[450]
Nucleic acid	ssDNA/ZnO/MWNTs/CHIT/GCE	-	2.8×10^{-12} mol L^{-1}	$1.0 \times 10^{-11} - 1.0 \times 10^{-6}$ mol L^{-1}	-	[496]
	ssDNA/AuNPs/MWNTs/ ZnO NWs/GCE	-	3.5×10^{-14} M	$1.0 \times 10^{-13} - 1.0 \times 10^{-7}$ M	-	[466]
	ssDNA/ZnO/CILE	-	2.5×10^{-13} mol L^{-1}	$1.0 \times 10^{-12} - 1.0 \times 10^{-8}$ mol L^{-1}	-	[467]
	ssDNA/Cu_2O/CPE	-	1.0×10^{-10} mol L^{-1}	$1.0 \times 10^{-10} - 1 \times 10^{-6}$ mol L^{-1}	-	[469]
	ssDNA/CeO_2-SWNTs BMIMPF6/GCE	-	2.3×10^{-13} mol L^{-1}	$1.0 \times 10^{-12} - 1.0 \times 10^{-7}$ mol L^{-1}	-	[497]
	ssCT-DNA/CH-Fe_3O_4/ITO	-	0.0025 ppm	1–300 ppm	-	[462]
	PNA/Fe_3O_4-GOPS/ITO	-	0.1×10^{-15} M	$0.1 \times 10^{-15} - 50.0 \times 10^{-15}$ M	-	[470]

Table 4. *Cont.*

Target Biomolecule	Electrode	Sensitivity	Detection Limit (mM)	Linear Range (mM)	Response Time (s)/ Potential (V)	Ref.
Antibody	BSA/anti-AFP/CH-MnO_2/ MWNT-Ag/GCE	-	0.08 ng mL^{-1}	0.25–250 ng mL^{-1}	-	[477]
	BSA/r-IgGs/Nano-ZnO/ITO	189 Ω nM^{-1} dm^{-3} cm^{-2}	0.006 nM dm^{-3}	0.006–0.01 nM dm^{-3}	-	[498]
	Anti-CEA/Fe_3O_4 NRs/CPE	-	0.9 ng mL^{-1}	1.5–80 ng mL^{-1}	-	[499]
	HRP-anti-hIgGAu/SiO_2 NPs PTHGCE	-	0.035 ng mL^{-1}	0.1–200 ng mL^{-1}	-	[500]

6.5. Non-Enzymatic Biosensors

The direct electrochemistry of glucose (oxidation or reduction) was used for non-enzymatic glucose sensing, which was quick and inexpensive [501]. The direct oxidation of glucose using noble metal electrodes, however, has three significant drawbacks [502,503]: (1) limited glucose sensitivity due to the slow electrooxidation kinetics of glucose with conventional electrodes, (2) low selectivity because several sugars can be oxidized in the same potential range as glucose, and (3) decreased electrode activity due to ion contamination. An increased electrode surface area enabled more glucose to come into contact with the electrode surface, thus eliminating the sensitivity and selectivity limitations. In the non-enzymatic process of glucose oxidation, hydrogen atoms are abstracted concurrently with organic species adsorption [504]. This is the rate-determining step in the glucose electrooxidation catalytic process. IHOAM is a hypothesis put forth by Bruke et al. to explain the intricate electrocatalytic process of glucose [504].

Metals, particularly noble metals, were investigated as electrode materials for non-enzymatic glucose biosensors [501,502]. Several metal alloys and hybrid materials have been developed as a result of advances in materials science in order to improve the properties of noble metals and metal oxides alone. Xiao et al. developed a flexible electrochemical glucose sensor by incorporating the nanocomposite PtAu alloy and MnO_2 into graphene paper [505]. As a result of electrodeposition on graphene paper, a PtAu-MnO_2 nanocomposite was developed with tight contact between the PtAu alloy and the MnO_2. This glucose sensor had a linear range of 0.1 mM to 30 mM and a high sensitivity of 58.54 μA mM^{-1} cm^{-2} [505]. Lee et al. created a disposable non-enzymatic blood glucose sensor strip using microporous Pt as an electrode material and poly(vinyl acetate) as a binding material. The mixture was then applied to a polyimide film surface with a conducting circuit screen printed on it. In whole human blood, the sensor showed acceptable stabilization for 30 days with a sensitivity of 0.0054 μA cm^{-2} $mgdL^{-1}$ [506]. An electrode fabricated from nanoporous Cu (NPC) was used by Chen et al. to make a portable micro glucose sensor [507]. In this non-enzymatic sensor, CuO nanocoral arrays had high conductivity and high glucose catalytic activity. It had a linear range of 0.0005 to 5 mM and a sensitivity of 1621 μA mM^{-1} cm^{-2}. Liu et al. combined a wet chemical process with an annealing procedure to create 3D copper oxide nanowire arrays (CuONWAs). In the end, the CuONWA/CF platform served as a glucose sensor [508]. Because the copper foam and nanowire arrays increase the surface area of the device, its sensitivity is improved. By using tellurium microtubes, Guascito et al. altered the surface of a Pt electrode using a drop-casting technique. It was found that the non-enzymatic glucose sensor was more sensitive, stable, and reproducible when compared with a Pt electrode that had not been modified [509].

7. Conclusions

A SMOx-based sensor translates a response into an electrical signal by using a receptor-transducer device. A wide range of applications, such as the detection of diseases and

illnesses, environmental monitoring, water and food quality monitoring, and drug delivery, prompted scientists and researchers to develop more sensitive and selective sensors. SMOx-based sensors need to capture recognition signals efficiently and convert them into electrochemical, electrical, optical, gravimetric, or acoustic signals (transduction process). Increasing transducer performance is another challenge, as it allows for increased sensitivity, faster response times, reproducibility, and lowering detection limits, even to detect single molecules and miniaturization of the sensing devices. Combining sensing technology with nano-SMOx-based devices, like zero- to three-dimensional FETs and IoT, with high surface-to-volume ratios, good conductivities, shock-bearing properties, and colour tuning can overcome these challenges. In this review, we provide an overview of the development of SMOx-based sensors.

In this review, we discussed, the recent advancements in semiconductor metal oxides (SMOx) for gas sensing, chemical sensing, and biosensing applications. The unique intrinsic chemical, physical, optical, and electronic properties of SMOxs entail low detection limits, high sensitivity, and fast response time, making SMOx materials a popular choice for sensing applications. Over the past few decades, the synthesis of SMOx-based nanomaterials in varying sizes, structures, and crystal morphologies has enabled the detection of gases, such as H_2, CO, O_2, SO_2, NO_2, and H_2S, and various chemicals and biomolecules like glucose, cholesterol, nucleic acids, and other important biomolecules. SMOx materials possess a large specific surface area, superior electron transport rate, extraordinary permeability, and active reaction sites, making them well-suited for stable sensing of specific gases, chemicals, and biomolecules at room temperature. Different architectural morphologies of nano-SMOxs are used to accelerate the rate of electron transport, resulting in improved sensitivity.

This review also highlights the improvement of sensing properties through various strategies, such as loading with nanomaterials, doping with elements, and constructing heterojunctions with other functional materials. The sensing properties of SMOx-based nanoparticles were found to be extensively improved by decorating their surfaces with nanomaterials, which change electron accumulation and enhance their catalytic effect through electronic and chemical excitation, respectively. The incorporation of a large number of dopants into the lattice of SMOx changes their crystal and electronic structure, reducing the bandwidth and increasing the active sites on the surface, which affects the sensitivity and selectivity. The formation of heterojunctions effectively rectifies electron transfer on the surface between two materials, resulting in improved sensitivity. The composites of SMOx with other functional materials also enhance the sensitivity and response rate at low temperatures due to possible synergistic effects and defect structures. These developments in SMOx composites have the potential to enable their practical applications.

8. Future Aspects

Despite the significant advancements in the development of semiconductor metal oxide (SMOx)-based sensors, there is still room for improvement in terms of selectivity, sensitivity, and working temperature. Recent studies highlighted the potential use of nanostructured SMOx-based sensors for their applications in sensing fields, specifically as gas, chemical, and biological sensors. However, new materials and heterostructure designs require special attention for further development mechanisms, including influencing the sensing activity. The future of SMOx-based sensor research can focus on (1) developing new materials and new heterojunction interfaces and (2) exploring the mechanisms that influence sensing activity and improving selectivity and sensitivity for the detection of gas, chemical, and biological molecules. The implementation of new strategies, such as doping with electronically active materials, functionalization of SMOxs with unique functional groups, and development of sensing materials, is crucial in fabricating more sensitive novel sensors. The use of SMOx-based sensors was found to offer several advantages over traditional sensors, including higher sensitivity, exceptional selectivity, quick response time, low detection limits, and compact size. The objective of this review was to aid in

the development of a new generation of sensing tools that can identify a wide variety of molecules in a variety of contexts, such as environmental danger gases and therapeutic biomolecules. Rapid and precise detection of gases, chemicals, and biological materials is crucial for an effective response. Therefore, to achieve this goal, a hybrid sensor system might be highly desirable. Moreover, integrated sensors for the detection of hybridized gas; chemicals; a mixture of toxic gases; and hazardous biological substances, like pathogenic microorganisms, bacteria, and viruses, can be realized with SMOx materials. These unique SMOx-based sensors can be utilized in a wide range of applications, such as in hospitals, defense areas, or war zones; for pharmaceutical, pesticide, textile, and meat industries; and in houses. These sensors also detect the growing threat of natural infectious diseases or industrial accidents. In summary, SMOx-based sensors have the potential to uncover new opportunities for the detection, identification, and quantification of toxic gases in various settings, such as food, hospitals, and the ocean. These new and innovative approaches must be highly selective, sensitive, reliable, fast-responding, and capable of autonomous screening. Moreover, they should be able to transmit information securely and wirelessly in real time. Also, SMOxs can be used for different types of optical sensor fabrications, including fiber optics and waveguide-based sensors, and have a lot of advantages over other types of sensors [508].

Author Contributions: S.K.M., T.D. and S.T. discussed the plan and agreed on it. T.D., S.K.M. and S.T. drafted designs for the manuscript. The manuscript was written by T.D., T.N., S.T. and S.K.M. They all reviewed and commented on the original draft of the manuscript. All authors have read and agreed to the published version of the manuscript.

Funding: This material is based upon work supported by ST's National Science Foundation award under Grant No. ECCS-2138701 and VentureWell Grant 21716-20.

Institutional Review Board Statement: Not applicable.

Informed Consent Statement: Not applicable.

Data Availability Statement: Not applicable.

Conflicts of Interest: The authors declare no conflict of interest.

References

1. Dey, A. Semiconductor metal oxide gas sensors: A review. *Mater. Sci. Eng. B* **2018**, *229*, 206–217. [CrossRef]
2. Usha, S.P.; Mishra, S.K.; Gupta, B.D. Fiber optic hydrogen sulfide gas sensors utilizing ZnO thin film/ZnO nanoparticles A comparison of surface plasmon resonance and lossy mode resonance. *Sens. Actuators B Chem.* **2015**, *218*, 196–204. [CrossRef]
3. Amoah, P.K.; Hassan, Z.M.; Lin, P.; Redel, E.; Baumgart, H.; Obeng, Y.S. Broadband dielectric spectroscopic detection of ethanol: A side-by-side comparison of ZnO and HKUST-1 MOFs as sensing media. *Chemosensors* **2022**, *10*, 241. [CrossRef]
4. Tabassum, R.; Mishra, S.K.; Gupta, B.D. Surface plasmon resonance-based fiber optic hydrogen sulphide gas sensor utilizing Cu–ZnO thin films. *Phys. Chem. Chem. Phys.* **2013**, *15*, 11868–11874. [CrossRef]
5. Mirzaei, A.; Leonardi, S.; Neri, G. Detection of hazardous volatile organic compounds (VOCs) by metal oxide nanostructures-based gas sensors: A review. *Ceram. Int.* **2016**, *42*, 15119–15141. [CrossRef]
6. Paghi, A.; Mariani, S.; Barillaro, G. 1D and 2D Field Effect Transistors in Gas Sensing: A Comprehensive Review. *Small* **2023**, *19*, 2206100. [CrossRef]
7. Mishra, S.K.; Rani, S.; Gupta, B.D. Surface plasmon resonance based fiber optic hydrogen sulphide gas sensor utilizing nickel oxide doped ITO thin film. *Sens. Actuators B Chem.* **2014**, *195*, 215–222. [CrossRef]
8. Usha, S.P.; Mishra, S.K.; Gupta, B.D. Fabrication and characterization of a SPR based fiber optic sensor for the detection of chlorine gas using silver and zinc oxide. *Materials* **2015**, *8*, 2204–2216. [CrossRef]
9. He, H. Metal oxide semiconductors and conductors. In *Solution Processed Metal Oxide Thin Films for Electronic Applications*; Elsevier: Amsterdam, The Netherlands, 2020; pp. 7–30.
10. Mishra, S.K.; Gupta, B.D. Surface plasmon resonance-based fiber optic chlorine gas sensor utilizing indium-oxide-doped tin oxide film. *J. Light. Technol.* **2015**, *33*, 2770–2776. [CrossRef]
11. Doan, T.H.P.; Hong, W.G.; Noh, J.-S. Palladium nanoparticle-decorated multi-layer $Ti_3C_2T_x$ dual-functioning as a highly sensitive hydrogen gas sensor and hydrogen storage. *RSC Adv.* **2021**, *11*, 7492–7501. [CrossRef]
12. Barsan, N.; Koziej, D.; Weimar, U. Metal oxide-based gas sensor research: How to? *Sens. Actuators B Chem.* **2007**, *121*, 18–35. [CrossRef]

13. Franke, M.E.; Koplin, T.J.; Simon, U. Metal and metal oxide nanoparticles in chemiresistors: Does the nanoscale matter? *Small* **2006**, *2*, 36–50. [CrossRef] [PubMed]
14. Usha, S.P.; Mishra, S.K.; Gupta, B.D. Zinc oxide thin film/nanorods based lossy mode resonance hydrogen sulphide gas sensor. *Mater. Res. Express* **2015**, *2*, 095003. [CrossRef]
15. Mishra, A.K.; Mishra, S.K. MgF_2 prism/rhodium/graphene: Efficient refractive index sensing structure in optical domain. *J. Phys. Condens. Matter* **2017**, *29*, 145001. [CrossRef] [PubMed]
16. Mishra, A.K.; Mishra, S.K.; Gupta, B.D. Gas-clad two-way fiber optic SPR sensor: A novel approach for refractive index sensing. *Plasmonics* **2015**, *10*, 1071–1076. [CrossRef]
17. Chen, X.; Shen, S.; Guo, L.; Mao, S.S. Semiconductor-based photocatalytic hydrogen generation. *Chem. Rev.* **2010**, *110*, 6503–6570. [CrossRef]
18. Mishra, S.; Mishra, A.; Misra, K.; Verma, R. Detection of alcohol content in food products by lossy mode resonance technique. *J. Electrochem. Soc.* **2022**, *169*, 077504.
19. Yamazoe, N.; Sakai, G.; Shimanoe, K. Oxide semiconductor gas sensors. *Catal. Surv. Asia* **2003**, *7*, 63–75. [CrossRef]
20. Degler, D.; Weimar, U.; Barsan, N. Current understanding of the fundamental mechanisms of doped and loaded semiconducting metal-oxide-based gas sensing materials. *ACS Sens.* **2019**, *4*, 2228–2249. [CrossRef]
21. Moseley, P.T. Progress in the development of semiconducting metal oxide gas sensors: A review. *Meas. Sci. Technol.* **2017**, *28*, 082001. [CrossRef]
22. Mishra, S.K.; Verma, R.K.; Mishra, A.K. Versatile Sensing Structure: GaP/Au/Graphene/Silicon. *Photonics* **2021**, *8*, 547. [CrossRef]
23. Gaur, D.S.; Purohit, A.; Mishra, S.K.; Mishra, A.K. An Interplay between Lossy Mode Resonance and Surface Plasmon Resonance and Their Sensing Applications. *Biosensors* **2022**, *12*, 721. [CrossRef] [PubMed]
24. Batzill, M. Surface science studies of gas sensing materials: SnO_2. *Sensors* **2006**, *6*, 1345–1366. [CrossRef]
25. Barsan, N.; Schweizer-Berberich, M.; Göpel, W. Fundamental and practical aspects in the design of nanoscaled SnO_2 gas sensors: A status report. *Fresenius' J. Anal. Chem.* **1999**, *365*, 287–304. [CrossRef]
26. Batzill, M.; Diebold, U. The surface and materials science of tin oxide. *Prog. Surf. Sci.* **2005**, *79*, 47–154. [CrossRef]
27. Lu, J.G.; Chang, P.; Fan, Z. Quasi-one-dimensional metal oxide materials—Synthesis, properties and applications. *Mater. Sci. Eng. R Rep.* **2006**, *52*, 49–91. [CrossRef]
28. Rothschild, A.; Komem, Y. On the relationship between the grain size and gas-sensitivity of chemo-resistive metal-oxide gas sensors with nanosized grains. *J. Electroceramics* **2004**, *13*, 697–701. [CrossRef]
29. Comini, E.; Baratto, C.; Faglia, G.; Ferroni, M.; Vomiero, A.; Sberveglieri, G. Quasi-one dimensional metal oxide semiconductors: Preparation, characterization and application as chemical sensors. *Prog. Mater. Sci.* **2009**, *54*, 1–67. [CrossRef]
30. Korotcenkov, G. Gas response control through structural and chemical modification of metal oxide films: State of the art and approaches. *Sens. Actuators B Chem.* **2005**, *107*, 209–232. [CrossRef]
31. Eranna, G.; Joshi, B.; Runthala, D.; Gupta, R. Oxide materials for development of integrated gas sensors—A comprehensive review. *Crit. Rev. Solid State Mater. Sci.* **2004**, *29*, 111–188. [CrossRef]
32. Şerban, I.; Enesca, A. Metal oxides-based semiconductors for biosensors applications. *Front. Chem.* **2020**, *8*, 354. [CrossRef] [PubMed]
33. Sato, H.; Minami, T.; Takata, S.; Yamada, T. Transparent conducting p-type NiO thin films prepared by magnetron sputtering. *Thin Solid Film* **1993**, *236*, 27–31. [CrossRef]
34. Kumbhakar, P.; Chowde Gowda, C.; Mahapatra, P.L.; Mukherjee, M.; Malviya, K.D.; Chaker, M.; Chandra, A.; Lahiri, B.; Ajayan, P.M.; Jariwala, D.; et al. Emerging 2D metal oxides and their applications. *Mater. Today* **2021**, *45*, 142–168. [CrossRef]
35. Chavali, M.S.; Nikolova, M.P. Metal oxide nanoparticles and their applications in nanotechnology. *SN Appl. Sci.* **2019**, *1*, 607. [CrossRef]
36. Korotcenkov, G.; Cho, B. Metal oxide composites in conductometric gas sensors: Achievements and challenges. *Sens. Actuators B Chem.* **2017**, *244*, 182–210. [CrossRef]
37. Usha, S.P.; Shrivastav, A.M.; Gupta, B.D. Semiconductor metal oxide/polymer based fiber optic lossy mode resonance sensors: A contemporary study. *Opt. Fiber Technol.* **2018**, *45*, 146–166. [CrossRef]
38. Espid, E.; Taghipour, F.J.C.R.i.S.S.; Sciences, M. UV-LED Photo-activated Chemical Gas Sensors: A Review. *Crit. Rev. Solid State Mater. Sci.* **2017**, *42*, 416–432. [CrossRef]
39. Wetchakun, K.; Samerjai, T.; Tamaekong, N.; Liewhiran, C.; Siriwong, C.; Kruefu, V.; Wisitsoraat, A.; Tuantranont, A.; Phanichphant, S. Semiconducting metal oxides as sensors for environmentally hazardous gases. *Sens. Actuators B Chem.* **2011**, *160*, 580–591. [CrossRef]
40. Balamurugan, C.; Song, S.-J.; Kim, H.-S.; Balamurugan, C.; Song, S.-J.; Kim, H.-S. Enhancing gas response characteristics of mixed metal oxide gas sensors. *J. Korean Ceram. Soc.* **2018**, *55*, 1–20. [CrossRef]
41. Kanan, S.M.; El-Kadri, O.M.; Abu-Yousef, I.A.; Kanan, M.C. Semiconducting metal oxide based sensors for selective gas pollutant detection. *Sensors* **2009**, *9*, 8158–8196. [CrossRef]
42. Tomchenko, A.A.; Harmer, G.P.; Marquis, B.T.; Allen, J.W. Semiconducting metal oxide sensor array for the selective detection of combustion gases. *Sens. Actuators B Chem.* **2003**, *93*, 126–134. [CrossRef]
43. Afzal, A.; Cioffi, N.; Sabbatini, L.; Torsi, L. NO_x sensors based on semiconducting metal oxide nanostructures: Progress and perspectives. *Sens. Actuators B Chem.* **2012**, *171*, 25–42. [CrossRef]

44. Huang, J.; Wan, Q. Gas sensors based on semiconducting metal oxide one-dimensional nanostructures. *Sensors* **2009**, *9*, 9903–9924. [CrossRef]
45. Pinna, N.; Neri, G.; Antonietti, M.; Niederberger, M. Nonaqueous synthesis of nanocrystalline semiconducting metal oxides for gas sensing. *Angew. Chem.* **2004**, *116*, 4445–4449. [CrossRef]
46. Concina, I.; Ibupoto, Z.H.; Vomiero, A. Semiconducting metal oxide nanostructures for water splitting and photovoltaics. *Adv. Energy Mater.* **2017**, *7*, 1700706. [CrossRef]
47. Wagner, T.; Waitz, T.; Roggenbuck, J.; Fröba, M.; Kohl, C.-D.; Tiemann, M. Ordered mesoporous ZnO for gas sensing. *Thin Solid Film.* **2007**, *515*, 8360–8363. [CrossRef]
48. Szilágyi, I.M.; Saukko, S.; Mizsei, J.; Tóth, A.L.; Madarász, J.; Pokol, G. Gas sensing selectivity of hexagonal and monoclinic WO_3 to H_2S. *Solid State Sci.* **2010**, *12*, 1857–1860. [CrossRef]
49. Brezesinski, T.; Fattakhova Rohlfing, D.; Sallard, S.; Antonietti, M.; Smarsly, B.M. Highly crystalline WO_3 thin films with ordered 3D mesoporosity and improved electrochromic performance. *Small* **2006**, *2*, 1203–1211. [CrossRef]
50. Cheng, J.; Wang, J.; Li, Q.; Liu, H.; Li, Y. A review of recent developments in tin dioxide composites for gas sensing application. *J. Ind. Eng. Chem.* **2016**, *44*, 1–22. [CrossRef]
51. Cheng, J.; Liu, L.; Zhang, J.; Liu, F.; Zhang, X. Influences of anion exchange and phase transformation on the supercapacitive properties of α-Co (OH) 2. *J. Electroanal. Chem.* **2014**, *722*, 23–31. [CrossRef]
52. Yang, X.; Cao, C.; Hohn, K.; Erickson, L.; Maghirang, R.; Hamal, D.; Klabunde, K. Highly visible-light active C-and V-doped TiO_2 for degradation of acetaldehyde. *J. Catal.* **2007**, *252*, 296–302. [CrossRef]
53. Waitz, T.; Becker, B.; Wagner, T.; Sauerwald, T.; Kohl, C.-D.; Tiemann, M. Ordered nanoporous SnO_2 gas sensors with high thermal stability. *Sens. Actuators B Chem.* **2010**, *150*, 788–793. [CrossRef]
54. Zhou, X.; Cao, Q.; Huang, H.; Yang, P.; Hu, Y. Study on sensing mechanism of CuO–SnO_2 gas sensors. *Mater. Sci. Eng. B* **2003**, *99*, 44–47. [CrossRef]
55. Choi, K.S.; Park, S.; Chang, S.-P. Enhanced ethanol sensing properties based on SnO2 nanowires coated with Fe_2O_3 nanoparticles. *Sens. Actuators B Chem.* **2017**, *238*, 871–879. [CrossRef]
56. Liu, H.; Chen, S.; Wang, G.; Qiao, S.Z. Ordered Mesoporous Core/Shell SnO_2/C Nanocomposite as High-Capacity Anode Material for Lithium-Ion Batteries. *Chem. A Eur. J.* **2013**, *19*, 16897–16901. [CrossRef] [PubMed]
57. Zhao, X.; Zhou, R.; Hua, Q.; Dong, L.; Yu, R.; Pan, C. Recent progress in ohmic/Schottky-contacted ZnO nanowire sensors. *J. Nanomater.* **2015**, *2015*, 7. [CrossRef]
58. Eto, T.; Endo, S.; Imai, M.; Katayama, Y.; Kikegawa, T. Crystal structure of NiO under high pressure. *Phys. Rev. B* **2000**, *61*, 14984. [CrossRef]
59. Gomaa, M.M.; Sayed, M.H.; Patil, V.L.; Boshta, M.; Patil, P.S. Gas sensing performance of sprayed NiO thin films toward NO_2 gas. *J. Alloys Compd.* **2021**, *885*, 160908. [CrossRef]
60. Simion, C.E.; Ghica, C.; Mihalcea, C.G.; Ghica, D.; Mercioniu, I.; Somacescu, S.; Florea, O.G.; Stanoiu, A. Insights about CO Gas-Sensing Mechanism with NiO-Based Gas Sensors—The Influence of Humidity. *Chemosensors* **2021**, *9*, 244. [CrossRef]
61. Li, Q.; Zeng, W.; Li, Y. NiO-Based Gas Sensors for Ethanol Detection: Recent Progress. *Sensors* **2022**, *2022*, 1855493. [CrossRef]
62. Reddy, G.; Reddy, S.; Swamy, B.E.K.; Kumar, M.; Harish, K.N.; Naveen, C.S.; Kumar, G.R.; Aravinda, T. Electrochemical Detection of Uric Acid by using NiO Nanoparticles *Anal. Bioanal. Electrochem.* **2022**, *14*, 432–443.
63. Amin, S.; Tahira, A.; Solangi, A.; Mazzaro, R.; Ibupoto, Z.H.; Vomiero, A. A sensitive enzyme-free lactic acid sensor based on NiO nanoparticles for practical applications. *Anal. Methods* **2019**, *11*, 3578–3583. [CrossRef]
64. Gomaa, M.M.; RezaYazdi, G.; Rodner, M.; Greczynski, G.; Boshta, M.; Osman, M.B.S.; Khranovskyy, V.; Eriksson, J.; Yakimova, R. Exploring NiO nanosize structures for ammonia sensing. *J. Mater. Sci. Mater. Electron.* **2018**, *29*, 11870–11877. [CrossRef]
65. Yang, H.; Hu, Y.; Yin, X.; Huang, J.; Qiao, C.; Hu, Z.; He, C.; Huo, D.; Hou, C. A disposable and sensitive non-enzymatic glucose sensor based on a 3D-Mn-doped NiO nanoflower-modified flexible electrode. *Analyst* **2023**, *148*, 153–162. [CrossRef]
66. Jauch, W.; Reehuis, M.; Bleif, H.; Kubanek, F.; Pattison, P. Crystallographic symmetry and magnetic structure of CoO. *Phys. Rev. B* **2001**, *64*, 052102. [CrossRef]
67. Logothetis, E.M.; Park, K.; Meitzler, A.H.; Laud, K.R. Oxygen sensors using CoO ceramics. *Appl. Phys. Lett.* **2008**, *26*, 209–211. [CrossRef]
68. Dai, C.; Chen, M.; Lin, Y.; Qi, R.; Luo, C.; Peng, H.; Lin, H. High performance gas sensors based on layered cobaltite nanoflakes with moisture resistance. *Appl. Surf. Sci.* **2022**, *604*, 154487. [CrossRef]
69. Ma, A.; Park, H.J.; Seo, J.H.; Jang, K.Y.; Lee, H.K.; Kim, D.Y.; Lee, J.E.; Nam, K.M.; Lee, D.-S. Phase transition of non-equilibrium wurtzite CoO: Spontaneous deposition of sensing material for ultrasensitive detection of acetone. *Sens. Actuators B Chem.* **2020**, *308*, 127698. [CrossRef]
70. Duan, J.; Yang, S.; Liu, H.; Gong, J.; Huang, H.; Zhao, X.; Zhang, R.; Du, Y. Single crystal SnO2 zigzag nanobelts. *J. Am. Chem. Soc.* **2005**, *127*, 6180–6181. [CrossRef]
71. Masuda, Y. Recent advances in SnO_2 nanostructure based gas sensors. *Sens. Actuators B Chem.* **2022**, *364*, 131876. [CrossRef]
72. Liu, P.; Wang, J.; Jin, H.; Ge, M.; Zhang, F.; Wang, C.; Sun, Y.; Dai, N. SnO_2 mesoporous nanoparticle-based gas sensor for highly sensitive and low concentration formaldehyde detection. *RSC Adv.* **2023**, *13*, 2256–2264. [CrossRef] [PubMed]
73. Mei, L.; Chen, Y.; Ma, J. Gas Sensing of SnO_2 Nanocrystals Revisited: Developing Ultra-Sensitive Sensors for Detecting the H_2S Leakage of Biogas. *Sci. Rep.* **2014**, *4*, 6028. [CrossRef] [PubMed]

74. Choi, P.G.; Izu, N.; Shirahata, N.; Masuda, Y. SnO_2 Nanosheets for Selective Alkene Gas Sensing. *ACS Appl. Nano Mater.* **2019**, *2*, 1820–1827. [CrossRef]
75. Li, B.; Zhou, Q.; Peng, S.; Liao, Y. Recent Advances of SnO2-Based Sensors for Detecting Volatile Organic Compounds. *Sec. Nanosci.* **2020**, *8*, 321. [CrossRef]
76. Choi, P.G.; Izu, N.; Shirahata, N.; Masuda, Y. Fabrication and H2-Sensing Properties of SnO_2 Nanosheet Gas Sensors. *ACS Omega* **2018**, *3*, 14592–14596. [CrossRef]
77. Li, M.; Gu, Y.; Zhang, Y.; Gao, X.; Ge, S.; Wei, G. Quantitative prediction of ternary mixed gases based on an SnO_2 sensor array and an SSA-BP neural network model. *Phys. Chem. Chem. Phys.* **2023**, *25*, 10935–10945. [CrossRef]
78. Khatoon, Z.; Fouad, H.; Alothman, O.Y.; Hashem, M.; Ansari, Z.A.; Ansari, S.A. Doped SnO2 Nanomaterials for E-Nose Based Electrochemical Sensing of Biomarkers of Lung Cancer. *ACS Omega* **2020**, *5*, 27645–27654. [CrossRef]
79. Mahajan, S.; Jagtap, S. Metal-oxide semiconductors for carbon monoxide (CO) gas sensing: A review. *Appl. Mater. Today* **2020**, *18*, 100483. [CrossRef]
80. Bârsan, N.; Weimar, U. Understanding the fundamental principles of metal oxide based gas sensors; the example of CO sensing with SnO_2 sensors in the presence of humidity. *J. Phys. Condens. Matter* **2003**, *15*, R813. [CrossRef]
81. Kim, J.-H.; Kim, J.-Y.; Mirzaei, A.; Kim, H.W.; Kim, S.S. Synergistic effects of SnO2 and Au nanoparticles decorated on WS2 nanosheets for flexible, room-temperature CO gas sensing. *Sens. Actuators B Chem.* **2021**, *332*, 129493. [CrossRef]
82. Aarik, J.; Aidla, A.; Uustare, T.; Sammelselg, V. Morphology and structure of TiO2 thin films grown by atomic layer deposition. *J. Cryst. Growth* **1995**, *148*, 268–275. [CrossRef]
83. Tian, X.; Cui, X.; Lai, T.; Ren, J.; Yang, Z.; Xiao, M.; Wang, B.; Xiao, X.; Wang, Y. Gas sensors based on TiO2 nanostructured materials for the detection of hazardous gases: A review. *Nano Mater. Sci.* **2021**, *3*, 390–403. [CrossRef]
84. Nunes, D.; Fortunato, E.; Martins, R. Flexible nanostructured TiO_2-based gas and UV sensors: A review. *Discov. Mater.* **2022**, *2*, 2. [CrossRef]
85. Shooshtari, M.; Vollebregt, S.; Vaseghi, Y.; Rajati, M.; Pahlavan, S. The sensitivity enhancement of TiO_2-based VOCs sensor decorated by gold at room temperature. *Nanotechnology* **2023**, *34*, 255501. [CrossRef]
86. Chen, Y.; Liu, B.; Chen, Z.; Zuo, X. Innovative Electrochemical Sensor Using TiO_2 Nanomaterials to Detect Phosphopeptides. *Anal. Chem.* **2021**, *93*, 10635–10643. [CrossRef]
87. Kaur, N.; Singh, M.; Moumen, A.; Duina, G.; Comini, E. 1D Titanium Dioxide: Achievements in Chemical Sensing. *Materials* **2020**, *13*, 2974. [CrossRef]
88. Rattu, G.; Krishna, P.M. TiO2 nanoparticles reagent based nonenzymatic label-free optical sensor for the rapid detection of L-lactate in apple juice. *Sens. Actuators Rep.* **2021**, *3*, 100067. [CrossRef]
89. Hajareh Haghighi, F.; Mercurio, M.; Cerra, S.; Salamone, T.A.; Bianymotlagh, R.; Palocci, C.; Romano Spica, V.; Fratoddi, I. Surface modification of TiO_2 nanoparticles with organic molecules and their biological applications. *J. Mater. Chem. B* **2023**, *11*, 2334–2366. [CrossRef]
90. Amri, F.; Septiani, N.L.W.; Rezki, M.; Iqbal, M.; Yamauchi, Y.; Golberg, D.; Kaneti, Y.V.; Yuliarto, B. Mesoporous TiO2-based architectures as promising sensing materials towards next-generation biosensing applications. *J. Mater. Chem. B* **2021**, *9*, 1189–1207. [CrossRef]
91. Yoshio, K.; Onodera, A.; Satoh, H.; Sakagami, N.; Yamashita, H. Crystal structure of ZnO: Li at 293 K and 19 K by x-ray diffraction. *Ferroelectrics* **2001**, *264*, 133–138. [CrossRef]
92. Bragg, W.L. LXII. The crystalline structure of zinc oxide. *Lond. Edinb. Dublin Philos. Mag. J. Sci.* **1920**, *39*, 647–651. [CrossRef]
93. Franco, M.A.; Conti, P.P.; Andre, R.S.; Correa, D.S. A review on chemiresistive ZnO gas sensors. *Sens. Actuators Rep.* **2022**, *4*, 100100. [CrossRef]
94. Zhou, S.; Yan, W.; Ling, M.; Liang, C. High-response H_2 sensing performances of ZnO nanosheets modulated by oxygen vacancies. *Inorg. Chem. Front.* **2023**, *10*, 3255–3262. [CrossRef]
95. Sha, R.; Basak, A.; Maity, P.C.; Badhulika, S. ZnO nano-structured based devices for chemical and optical sensing applications. *Sens. Actuators Rep.* **2022**, *4*, 100098. [CrossRef]
96. Fallatah, A.; Kuperus, N.; Almomtan, M.; Padalkar, S. Sensitive Biosensor Based on Shape-Controlled ZnO Nanostructures Grown on Flexible Porous Substrate for Pesticide Detection. *Sensors* **2022**, *22*, 3522. [CrossRef]
97. Krishna, M.S.; Singh, S.; Batool, M.; Fahmy, H.M.; Seku, K.; Shalan, A.E.; Lanceros-Mendez, S.; Zafar, M.N. A review on 2D-ZnO nanostructure based biosensors: From materials to devices. *Mater. Adv.* **2023**, *4*, 320–354. [CrossRef]
98. Zoubir, J.; Bakas, I.; Qourzal, S.; Tamimi, M.; Assabbane, A. Electrochemical sensor based on a ZnO-doped graphitized carbon for the electrocatalytic detection of the antibiotic hydroxychloroquine. *Application: Tap water and human urine. J. Appl. Electrochem.* **2023**, *53*, 1279–1294. [CrossRef]
99. Jarosch, D. Crystal structure refinement and reflectance measurements of hausmannite, Mn_3O_4. *Mineral. Petrol.* **1987**, *37*, 15–23. [CrossRef]
100. Bigiani, L.; Zappa, D.; Maccato, C.; Gasparotto, A.; Sada, C.; Comini, E.; Barreca, D. Hydrogen Gas Sensing Performances of p-Type Mn_3O_4 Nanosystems: The Role of Built-in Mn_3O_4/Ag and Mn_3O_4/SnO_2 Junctions. *Nanomaterials* **2020**, *10*, 511. [CrossRef]

101. Lupan, O.; Ursaki, V.; Chai, G.; Chow, L.; Emelchenko, G.A.; Tiginyanu, I.; Gruzintsev, A.N.; Redkin, A.J.S.; Chemical, A.B. Selective hydrogen gas nanosensor using individual ZnO nanowire with fast response at room temperature. *Sens. Actuators B Chem.* **2010**, *144*, 56–66. [CrossRef]
102. Zakrzewska, K. Gas sensing mechanism of TiO_2-based thin films. *Vacuum* **2004**, *74*, 335–338. [CrossRef]
103. Jimenez, I.; Arbiol, J.; Dezanneau, G.; Cornet, A.; Morante, J.J.S. Crystalline structure, defects and gas sensor response to NO_2 and H_2S of tungsten trioxide nanopowders. *Sens. Actuators B Chem.* **2003**, *93*, 475–485. [CrossRef]
104. Zhang, Y.-H.; Chen, Y.-B.; Zhou, K.-G.; Liu, C.-H.; Zeng, J.; Zhang, H.-L.; Peng, Y. Improving gas sensing properties of graphene by introducing dopants and defects: A first-principles study. *Nanotechnology* **2009**, *20*, 185504. [CrossRef] [PubMed]
105. Kim, K.; Lee, H.-B.-R.; Johnson, R.W.; Tanskanen, J.T.; Liu, N.; Kim, M.-G.; Pang, C.; Ahn, C.; Bent, S.F.; Bao, Z. Selective metal deposition at graphene line defects by atomic layer deposition. *Nat. Commun.* **2014**, *5*, 4781. [CrossRef] [PubMed]
106. Ahn, M.-W.; Park, K.-S.; Heo, J.-H.; Park, J.-G.; Kim, D.-W.; Choi, K.J.; Lee, J.-H.; Hong, S.-H. Gas sensing properties of defect-controlled ZnO-nanowire gas sensor. *Appl. Phys. Lett.* **2008**, *93*, 263103. [CrossRef]
107. Hübner, M.; Simion, C.E.; Tomescu-Stănoiu, A.; Pokhrel, S.; Bârsan, N.; Weimar, U. Influence of humidity on CO sensing with p-type CuO thick film gas sensors. *Sens. Actuators B Chem.* **2011**, *153*, 347–353. [CrossRef]
108. Rothschild, A.; Litzelman, S.J.; Tuller, H.L.; Menesklou, W.; Schneider, T.; Ivers-Tiffée, E. Temperature-independent resistive oxygen sensors based on SrTi1− $_x$Fe$_x$O$_3$− δ solid solutions. *Sens. Actuators B Chem.* **2005**, *108*, 223–230. [CrossRef]
109. Zaleska, A. Doped-TiO_2: A review. *Recent Pat. Eng.* **2008**, *2*, 157–164. [CrossRef]
110. Li, S.-S.; Xia, J.-B. Electronic states of a hydrogenic donor impurity in semiconductor nano-structures. *Phys. Lett. A* **2007**, *366*, 120–123. [CrossRef]
111. Waldrop, J.; Grant, R. Semiconductor heterojunction interfaces: Nontransitivity of energy-band discontiuities. *Phys. Rev. Lett.* **1979**, *43*, 1686. [CrossRef]
112. Walsh, A.; Da Silva, J.L.; Wei, S.-H.; Körber, C.; Klein, A.; Piper, L.; DeMasi, A.; Smith, K.E.; Panaccione, G.; Torelli, P. Nature of the Band Gap of In_2O_3 Revealed by First-Principles Calculations and X-Ray Spectroscopy. *Phys. Rev. Lett.* **2022**, *100*, 167402. [CrossRef] [PubMed]
113. Anothainart, K.; Burgmair, M.; Karthigeyan, A.; Zimmer, M.; Eisele, I. Light enhanced NO_2 gas sensing with tin oxide at room temperature: Conductance and work function measurements. *Sens. Actuators B Chem.* **2003**, *93*, 580–584. [CrossRef]
114. Heyd, J.; Peralta, J.E.; Scuseria, G.E.; Martin, R.L. Energy band gaps and lattice parameters evaluated with the Heyd-Scuseria-Ernzerhof screened hybrid functional. *J. Chem. Phys.* **2005**, *123*, 174101. [CrossRef] [PubMed]
115. White, S.; Sham, L. Electronic properties of flat-band semiconductor heterostructures. *Phys. Rev. Lett.* **1981**, *47*, 879. [CrossRef]
116. Sadeghi, E. Impurity binding energy of excited states in spherical quantum dot. *Phys. E Low Dimens. Syst. Nanostructures* **2009**, *41*, 1319–1322. [CrossRef]
117. Zhuravlev, M.Y.; Tsymbal, E.Y.; Vedyayev, A. Impurity-assisted interlayer exchange coupling across a tunnel barrier. *Phys. Rev. Lett.* **2005**, *94*, 026806. [CrossRef]
118. Langer, J.M.; Heinrich, H. Deep-level impurities: A possible guide to prediction of band-edge discontinuities in semiconductor heterojunctions. *Phys. Rev. Lett.* **1985**, *55*, 1414. [CrossRef]
119. Batzill, M.; Diebold, U. Surface studies of gas sensing metal oxides. *Phys. Chem. Chem. Phys.* **2007**, *9*, 2307–2318. [CrossRef]
120. Basu, S.; Bhattacharyya, P. Recent developments on graphene and graphene oxide based solid state gas sensors. *Sens. Actuators B Chem.* **2012**, *173*, 1–21. [CrossRef]
121. Bittencourt, C.; Felten, A.; Espinosa, E.; Ionescu, R.; Llobet, E.; Correig, X.; Pireaux, J.-J. WO_3 films modified with functionalised multi-wall carbon nanotubes: Morphological, compositional and gas response studies. *Sens. Actuators B Chem.* **2006**, *115*, 33–41. [CrossRef]
122. Cui, S.; Pu, H.; Wells, S.A.; Wen, Z.; Mao, S.; Chang, J.; Hersam, M.C.; Chen, J. Ultrahigh sensitivity and layer-dependent sensing performance of phosphorene-based gas sensors. *Nat. Commun.* **2015**, *6*, 8632. [CrossRef] [PubMed]
123. de Lacy Costello, B.; Ledochowski, M.; Ratcliffe, N.M. The importance of methane breath testing: A review. *J. Breath Res.* **2013**, *7*, 024001. [CrossRef] [PubMed]
124. Dong, C.; Liu, X.; Han, B.; Deng, S.; Xiao, X.; Wang, Y. Nonaqueous synthesis of Ag-functionalized In_2O_3/ZnO nanocomposites for highly sensitive formaldehyde sensor. *Sens. Actuators B Chem.* **2016**, *224*, 193–200. [CrossRef]
125. Comini, E. Metal oxide nano-crystals for gas sensing. *Anal. Chim. Acta* **2006**, *568*, 28–40. [CrossRef] [PubMed]
126. Artzi-Gerlitz, R.; Benkstein, K.D.; Lahr, D.L.; Hertz, J.L.; Montgomery, C.B.; Bonevich, J.E.; Semancik, S.; Tarlov, M.J. Fabrication and gas sensing performance of parallel assemblies of metal oxide nanotubes supported by porous aluminum oxide membranes. *Sens. Actuators B Chem.* **2009**, *136*, 257–264. [CrossRef]
127. da Silva, L.F.; M'peko, J.-C.; Catto, A.C.; Bernardini, S.; Mastelaro, V.R.; Aguir, K.; Ribeiro, C.; Longo, E. UV-enhanced ozone gas sensing response of ZnO-SnO_2 heterojunctions at room temperature. *Sens. Actuators B Chem.* **2017**, *240*, 573–579. [CrossRef]
128. Dhawale, D.; Salunkhe, R.; Patil, U.; Gurav, K.; More, A.; Lokhande, C. Room temperature liquefied petroleum gas (LPG) sensor based on p-polyaniline/n-TiO_2 heterojunction. *Sens. Actuators B Chem.* **2008**, *134*, 988–992. [CrossRef]
129. Fergus, J.W. Perovskite oxides for semiconductor-based gas sensors. *Sens. Actuators B Chem.* **2007**, *123*, 1169–1179. [CrossRef]
130. Han, C.; Li, X.; Shao, C.; Li, X.; Ma, J.; Zhang, X.; Liu, Y. Composition-controllable p-CuO/n-ZnO hollow nanofibers for high-performance H_2S detection. *Sens. Actuators B Chem.* **2019**, *285*, 495–503. [CrossRef]

131. Dhawale, D.S.; Gujar, T.P.; Lokhande, C.D. TiO2 nanorods decorated with Pd nanoparticles for enhanced liquefied petroleum gas sensing performance. *Anal. Chem.* **2017**, *89*, 8531–8537. [CrossRef]
132. Shinde, V.; Gujar, T.; Lokhande, C. LPG sensing properties of ZnO films prepared by spray pyrolysis method: Effect of molarity of precursor solution. *Sens. Actuators B Chem.* **2007**, *120*, 551–559. [CrossRef]
133. Mitra, P.; Chatterjee, A.P.; Maiti, H.S. ZnO thin film sensor. *Mater. Lett.* **1998**, *35*, 33–38. [CrossRef]
134. Lee, J.E.; Lim, C.K.; Park, H.J.; Song, H.; Choi, S.-Y.; Lee, D.-S. ZnO–CuO core-hollow cube nanostructures for highly sensitive acetone gas sensors at the ppb level. *ACS Appl. Mater. Interfaces* **2020**, *12*, 35688–35697. [CrossRef]
135. Rai, P.; Majhi, S.; Yu, Y.; Lee, J. Noble metal oxide semiconductor shell nano-architectures as a new platform for gas sensor applications. *RSC Adv.* **2015**, *5*, 76229–76248. [CrossRef]
136. Nakate, U.T.; Patil, P.; Ghule, B.G.; Ekar, S.; Al-Osta, A.; Jadhav, V.V.; Mane, R.S.; Kale, S.; Naushad, M.; O'Dwyer, C. Gold sensitized sprayed SnO2 nanostructured film for enhanced LPG sensing. *J. Anal. Appl. Pyrolysis* **2017**, *124*, 362–368. [CrossRef]
137. Li, Y.; Chen, N.; Deng, D.; Xing, X.; Xiao, X.; Wang, Y. Formaldehyde detection: SnO2 microspheres for formaldehyde gas sensor with high sensitivity, fast response/recovery and good selectivity. *Sens. Actuators B Chem.* **2017**, *238*, 264–273. [CrossRef]
138. Gutpa, J.; Shaik, H.; Kumar, K.N.; Sattar, S.A. PVD techniques proffering avenues for fabrication of porous tungsten oxide (WO3) thin films: A review. *Mater. Sci. Semicond. Process.* **2022**, *143*, 106534. [CrossRef]
139. Saruhan, B.; Lontio Fomekong, R.; Nahirniak, S. Influences of semiconductor metal oxide properties on gas sensing characteristics. *Front. Sens.* **2021**, *2*, 657931. [CrossRef]
140. Hussain, S.; Javed, M.S.; Ullah, N.; Shaheen, A.; Aslam, N.; Ashraf, I.; Abbas, Y.; Wang, M.; Liu, G.; Qiao, G. Unique hierarchical mesoporous $LaCrO_3$ perovskite oxides for highly efficient electrochemical energy storage applications. *Ceram. Int.* **2019**, *45*, 15164–15170. [CrossRef]
141. Li, T.; Zeng, W.; Wang, Z. Quasi-one-dimensional metal-oxide-based heterostructural gas-sensing materials: A review. *Sens. Actuators B Chem.* **2015**, *221*, 1570–1585. [CrossRef]
142. Zhang, J.; Qin, Z.; Zeng, D.; Xie, C. Metal-oxide-semiconductor based gas sensors: Screening, preparation, and integration. *Phys. Chem. Chem. Phys.* **2017**, *19*, 6313–6329. [CrossRef] [PubMed]
143. Sahay, P.J.P. Multifunctional metal oxide nanomaterials for chemical gas sensing. *Procedia Eng.* **2017**, *215*, 145–151. [CrossRef]
144. Seiyama, T.; Kato, A.; Fujiishi, K.; Nagatani, M.J.A.C. A new detector for gaseous components using semiconductive thin films. 1962, 34, 1502–1503. *Anal. Chem.* **1962**, *34*, 1502–1503. [CrossRef]
145. Hoa, N.D.; Duy, N.V.; El-Safty, S.A.; Hieu, N.V. Meso-/nanoporous semiconducting metal oxides for gas sensor applications. *J. Nanomater.* **2015**, *16*, 186. [CrossRef]
146. Lewis, A.; Edwards, P. Validate personal air-pollution sensors. *Nature* **2016**, *535*, 29–31. [CrossRef]
147. Kalantar-Zadeh, K.; Berean, K.J.; Ha, N.; Chrimes, A.F.; Xu, K.; Grando, D.; Ou, J.Z.; Pillai, N.; Campbell, J.L.; Brkljača, R. A human pilot trial of ingestible electronic capsules capable of sensing different gases in the gut. *Nat. Electron.* **2018**, *1*, 79–87. [CrossRef]
148. Nugroho, F.A.; Darmadi, I.; Cusinato, L.; Susarrey-Arce, A.; Schreuders, H.; Bannenberg, L.J.; da Silva Fanta, A.B.; Kadkhodazadeh, S.; Wagner, J.B.; Antosiewicz, T.J. Metal–polymer hybrid nanomaterials for plasmonic ultrafast hydrogen detection. *Nat. Mater.* **2019**, *18*, 489–495. [CrossRef]
149. van den Broek, J.; Abegg, S.; Pratsinis, S.E.; Güntner, A.T. Highly selective detection of methanol over ethanol by a handheld gas sensor. *Nat. Commun.* **2019**, *10*, 4220. [CrossRef]
150. Tao, N. Challenges and promises of metal oxide nanosensors. *ACS Sens.* **2019**, *4*, 780. [CrossRef]
151. Williams, D.E. Low cost sensor networks: How do we know the data are reliable? *ACS Sens.* **2019**, *4*, 2558–2565. [CrossRef]
152. Hunter, G.W.; Akbar, S.; Bhansali, S.; Daniele, M.; Erb, P.D.; Johnson, K.; Liu, C.-C.; Miller, D.; Oralkan, O.; Hesketh, P.J. Editors' choice—Critical review—A critical review of solid state gas sensors. *J. Electrochem. Soc.* **2020**, *167*, 037570. [CrossRef]
153. Ihokura, K.; Watson, J. *The Stannic Oxide Gas Sensorprinciples and Applications*; CRC Press: Boca Raton, FL, USA, 2017.
154. Staerz, A.; Suzuki, T.; Weimar, U.; Barsan, N. SnO2: The most important base material for semiconducting metal oxide-based materials. In *Tin Oxide Materials*; Elsevier: Amsterdam, The Netherlands, 2020; pp. 345–377.
155. Stetter, J.R.; Penrose, W.R.; Yao, S. Sensors, chemical sensors, electrochemical sensors, and ECS. *J. Electrochem. Soc.* **2003**, *150*, S11. [CrossRef]
156. Yamazoe, N. Toward innovations of gas sensor technology. *Sens. Actuators B Chem.* **2005**, *108*, 2–14. [CrossRef]
157. Shankar, P.; Rayappan, J.B.B. Gas sensing mechanism of metal oxides: The role of ambient atmosphere, type of semiconductor and gases—A review. *Sci. Lett. J* **2015**, *4*, 126.
158. Hussain, S.; Yang, X.; Aslam, M.K.; Shaheen, A.; Javed, M.S.; Aslam, N.; Aslam, B.; Liu, G.; Qiao, G. Robust TiN nanoparticles polysulfide anchor for Li–S storage and diffusion pathways using first principle calculations. *Chem. Eng. J.* **2020**, *391*, 123595. [CrossRef]
159. Tiemann, M. Porous Metal Oxides as Gas Sensors. *Chem. Eur.* **2007**, *13*, 8376–8388. [CrossRef]
160. Korotcenkov, G. Metal oxides for solid-state gas sensors: What determines our choice? *Mater. Sci. Eng. B* **2007**, *139*, 1–23. [CrossRef]
161. Moseley, P.T.; Norris, J.O.; Williams, D.E. *Techniques and Mechanisms in Gas Sensing*; Adam Hilger: Bristol, UK, 1991; Volume 234.
162. Lu, Z.; Kanan, S.M.; Tripp, C.P. Synthesis of high surface area monoclinic WO_3 particles using organic ligands and emulsion based methods. *J. Mater. Chem.* **2002**, *12*, 983–989. [CrossRef]

163. Williams, D.E. Semiconducting oxides as gas-sensitive resistors. *Sens. Actuators B Chem.* **1999**, *57*, 1–16. [CrossRef]
164. Van de Krol, R.; Tuller, H. Electroceramics—The role of interfaces. *Solid State Ion* **2002**, *150*, 167–179. [CrossRef]
165. Hulanicki, A.; Glab, S.; Ingman, F. Chemical sensors: Definitions and classification. *Pure Appl. Chem.* **1991**, *63*, 1247–1250. [CrossRef]
166. Barsan, N.; Simion, C.; Heine, T.; Pokhrel, S.; Weimar, U. Modeling of sensing and transduction for p-type semiconducting metal oxide based gas sensors. *J. Electroceramics* **2010**, *25*, 11–19. [CrossRef]
167. Barsan, N.; Gauglitz, G.; Oprea, A.; Ostertag, E.; Proll, G.; Rebner, K.; Schierbaum, K.; Schleifenbaum, F.; Weimar, U. Chemical and biochemical sensors, 1. Fundamentals. In *Ullmann's Encyclopedia of Industrial Chemistry*; John Wiley&Sons: Hoboken, NJ, USA, 2000; pp. 1–81. [CrossRef]
168. Kuru, C.; Choi, C.; Kargar, A.; Choi, D.; Kim, Y.J.; Liu, C.H.; Yavuz, S.; Jin, S. MoS_2 nanosheet–Pd nanoparticle composite for highly sensitive room temperature detection of hydrogen. *Adv. Sci.* **2015**, *2*, 1500004. [CrossRef] [PubMed]
169. Henrich, V.E.; Cox, P.A. *The Surface Science of Metal Oxides*; Cambridge University Press: Cambridge, UK, 1996.
170. Dorenbos, P. The Eu3+ charge transfer energy and the relation with the band gap of compounds. *J. Lumin.* **2005**, *111*, 89–104. [CrossRef]
171. Ueda, M.; Ohtsuka, T. Luminescence from band-gap photo-excitation of titanium anodic oxide films. *Corros. Sci.* **2002**, *44*, 1633–1638. [CrossRef]
172. Palankovski, V.; Kaiblinger-Grujin, G.; Selberherr, S. Study of dopant-dependent band gap narrowing in compound semiconductor devices. *Mater. Sci. Eng. B* **1999**, *66*, 46–49. [CrossRef]
173. Ducéré, J.M.; Hemeryck, A.; Estève, A.; Rouhani, M.D.; Landa, G.; Ménini, P.; Tropis, C.; Maisonnat, A.; Fau, P.; Chaudret, B. A computational chemist approach to gas sensors: Modeling the response of SnO_2 to CO, O_2, and H_2O Gases. *J. Comput. Chem.* **2012**, *33*, 247–258. [CrossRef]
174. Wang, X.; Qin, H.; Chen, Y.; Hu, J. Sensing mechanism of SnO_2 surface to CO: Density functional theory calculations. *J. Phys. Chem. C* **2014**, *118*, 28548–28561. [CrossRef]
175. Chen, Y.; Wang, X.; Shi, C.; Li, L.; Qin, H.; Hu, J. Sensing mechanism of SnO2 (1 1 0) surface to H_2: Density functional theory calculations. *Sens. Actuators B Chem.* **2015**, *220*, 279–287. [CrossRef]
176. Schierbaum, K.; Weimar, U.; Göpel, W.; Kowalkowski, R. Conductance, work function and catalytic activity of SnO2-based gas sensors. *Sens. Actuators B Chem.* **1991**, *3*, 205–214. [CrossRef]
177. Morrison, S.R. Semiconductor gas sensors. *Sens. Actuators* **1981**, *2*, 329–341. [CrossRef]
178. Barsan, N.; Weimar, U. Conduction model of metal oxide gas sensors. *J. Electroceramics* **2001**, *7*, 143–167. [CrossRef]
179. Kim, I.-D.; Rothschild, A.; Tuller, H.L. Advances and new directions in gas-sensing devices. *Acta Mater.* **2013**, *61*, 974–1000. [CrossRef]
180. Rebholz, J.; Bonanati, P.; Weimar, U.; Barsan, N. Grain shape influence on semiconducting metal oxide based gas sensor performance: Modeling versus experiment. *Anal. Bioanal. Chem.* **2014**, *406*, 3977–3983. [CrossRef] [PubMed]
181. Yamazoe, N.; Shimanoe, K. Roles of shape and size of component crystals in semiconductor gas sensors: I. Response to oxygen. *J. Electrochem. Soc.* **2008**, *155*, J85. [CrossRef]
182. Kim, H.-J.; Lee, J.-H. Highly sensitive and selective gas sensors using p-type oxide semiconductors: Overview. *Sens. Actuators B Chem.* **2014**, *192*, 607–627. [CrossRef]
183. Cho, N.G.; Hwang, I.-S.; Kim, H.-G.; Lee, J.-H.; Kim, I.-D. Gas sensing properties of p-type hollow NiO hemispheres prepared by polymeric colloidal templating method. *Sens. Actuators B Chem.* **2011**, *155*, 366–371. [CrossRef]
184. Li, D.; Hu, J.; Wu, R.; Lu, J.G. Conductometric chemical sensor based on individual CuO nanowires. *Nanotechnology* **2010**, *21*, 485502. [CrossRef]
185. Choi, S.-W.; Park, J.Y.; Kim, S.S. Growth behavior and sensing properties of nanograins in CuO nanofibers. *Chem. Eng. J.* **2011**, *172*, 550–556. [CrossRef]
186. Yamazoe, N. New approaches for improving semiconductor gas sensors. *Sens. Actuators B Chem.* **1991**, *5*, 7–19. [CrossRef]
187. Matsushima, S.; Teraoka, Y.; Miura, N.; Yamazoe, N. Electronic interaction between metal additives and tin dioxide in tin dioxide-based gas sensors. *Jpn. J. Appl. Phys.* **1988**, *27*, 1798. [CrossRef]
188. Yamazoe, N.; Kurokawa, Y.; Seiyama, T. Effects of additives on semiconductor gas sensors. *Sens. Actuators* **1983**, *4*, 283–289. [CrossRef]
189. Müller, S.A.; Degler, D.; Feldmann, C.; Türk, M.; Moos, R.; Fink, K.; Studt, F.; Gerthsen, D.; Bârsan, N.; Grunwaldt, J.D. Exploiting synergies in catalysis and gas sensing using noble metal-loaded oxide composites. *ChemCatChem* **2018**, *10*, 864–880. [CrossRef]
190. Staerz, A.; Kim, T.-H.; Lee, J.-H.; Weimar, U.; Barsan, N. Nanolevel control of gas sensing characteristics via p–n heterojunction between Rh_2O_3 clusters and WO_3 crystallites. *J. Phys. Chem. C* **2017**, *121*, 24701–24706. [CrossRef]
191. Korotcenkov, G.; Brinzari, V.; Gulina, L.; Cho, B. The influence of gold nanoparticles on the conductivity response of SnO_2-based thin film gas sensors. *Appl. Surf. Sci.* **2015**, *353*, 793–803. [CrossRef]
192. Marikutsa, A.V.; Rumyantseva, M.N.; Frolov, D.D.; Morozov, I.V.; Boltalin, A.I.; Fedorova, A.A.; Petukhov, I.A.; Yashina, L.V.; Konstantinova, E.A.; Sadovskaya, E.M. Role of PdO_x and RuO_y clusters in oxygen exchange between nanocrystalline tin dioxide and the gas phase. *J. Phys. Chem. C* **2013**, *117*, 23858–23867. [CrossRef]
193. Morrison, S.R. Selectivity in semiconductor gas sensors. *Sens. Actuators* **1987**, *12*, 425–440. [CrossRef]

194. Miller, D.R.; Akbar, S.A.; Morris, P.A. Nanoscale metal oxide-based heterojunctions for gas sensing: A review. *Sens. Actuators B Chem.* **2014**, *204*, 250–272. [CrossRef]
195. Liu, C.; Kuang, Q.; Xie, Z.; Zheng, L. The effect of noble metal (Au, Pd and Pt) nanoparticles on the gas sensing performance of SnO_2-based sensors: A case study on the {221} high-index faceted SnO_2 octahedra. *CrystEngComm* **2015**, *17*, 6308–6313. [CrossRef]
196. Marikutsa, A.V.; Rumyantseva, M.N.; Konstantinova, E.A.; Shatalova, T.B.; Gaskov, A.M. Active sites on nanocrystalline tin dioxide surface: Effect of palladium and ruthenium oxides clusters. *J. Phys. Chem. C* **2014**, *118*, 21541–21549. [CrossRef]
197. Degler, D.; Rank, S.; Müller, S.; Pereira de Carvalho, H.W.; Grunwaldt, J.-D.; Weimar, U.; Barsan, N. Gold-loaded tin dioxide gas sensing materials: Mechanistic insights and the role of gold dispersion. *ACS Sens.* **2016**, *1*, 1322–1329. [CrossRef]
198. Morrison, S. *Roy the Chemical Physics of Surfaces*; Plenum Press: New York, NY, USA; London, UK, 1977.
199. Rebholz, J.; Dee, C.; Weimar, U.; Barsan, N. A self-doping surface effect and its influence on the sensor performance of undoped SnO_2 based gas sensors. *Procedia Eng.* **2015**, *120*, 83–87. [CrossRef]
200. Göpel, W.; Schierbaum, K.D. SnO_2 sensors: Current status and future prospects. *Sens. Actuators B Chem.* **1995**, *26*, 1–12. [CrossRef]
201. Yu, J.H.; Choi, G.M. Electrical and CO gas sensing properties of ZnO–SnO_2 composites. *Sens. Actuators B Chem.* **1998**, *52*, 251–256.
202. de Lacy Costello, B.; Ewen, R.; Jones, P.; Ratcliffe, N.; Wat, R. A study of the catalytic and vapour-sensing properties of zinc oxide and tin dioxide in relation to 1-butanol and dimethyldisulphide. *Sens. Actuators B Chem.* **1999**, *61*, 199–207. [CrossRef]
203. Zhu, C.; Chen, Y.; Wang, R.; Wang, L.; Cao, M.; Shi, X. Synthesis and enhanced ethanol sensing properties of α-Fe_2O_3/ZnO heteronanostructures. *Sens. Actuators B Chem.* **2009**, *140*, 185–189. [CrossRef]
204. Yoon, D.H.; Yu, J.H.; Choi, G.M. CO gas sensing properties of ZnO–CuO composite. *Sens. Actuators B Chem.* **1998**, *46*, 15–23. [CrossRef]
205. Cobianu, C.; Serban, B.-C.; Dumbravescu, N.; Buiu, O.; Avramescu, V.; Pachiu, C.; Bita, B.; Bumbac, M.; Nicolescu, C.-M.; Cobianu, C. Organic–inorganic ternary nanohybrids of single-walled carbon nanohorns for room temperature chemiresistive ethanol detection. *Nanomaterials* **2020**, *10*, 2552. [CrossRef]
206. Serban, B.-C.; Cobianu, C.; Buiu, O.; Bumbac, M.; Dumbravescu, N.; Avramescu, V.; Nicolescu, C.M.; Brezeanu, M.; Radulescu, C.; Craciun, G. Quaternary Holey Carbon Nanohorns/SnO_2/ZnO/PVP Nano-Hybrid as Sensing Element for Resistive-Type Humidity Sensor. *Coatings* **2021**, *11*, 1307. [CrossRef]
207. Haridas, D.; Gupta, V.; Sreenivas, K. Enhanced catalytic activity of nanoscale platinum islands loaded onto SnO_2 thin film for sensitive LPG gas sensors. *Bull. Mater. Sci.* **2008**, *31*, 397–400. [CrossRef]
208. Lu, Y.; Li, J.; Han, J.; Ng, H.-T.; Binder, C.; Partridge, C.; Meyyappan, M. Room temperature methane detection using palladium loaded single-walled carbon nanotube sensors. *Chem. Phys. Lett.* **2004**, *391*, 344–348. [CrossRef]
209. Wang, D.; Ma, Z.; Dai, S.; Liu, J.; Nie, Z.; Engelhard, M.H.; Huo, Q.; Wang, C.; Kou, R. Low-temperature synthesis of tunable mesoporous crystalline transition metal oxides and applications as Au catalyst supports. *J. Phys. Chem. C* **2008**, *112*, 13499–13509. [CrossRef]
210. Haridas, D.; Sreenivas, K.; Gupta, V. Improved response characteristics of SnO_2 thin film loaded with nanoscale catalysts for LPG detection. *Sens. Actuators B Chem.* **2008**, *133*, 270–275. [CrossRef]
211. Shimizu, Y.; Matsunaga, N.; Hyodo, T.; Egashira, M. Improvement of SO_2 sensing properties of WO_3 by noble metal loading. *Sens. Actuators B Chem.* **2001**, *77*, 35–40. [CrossRef]
212. Ruiz, A.M.; Cornet, A.; Shimanoe, K.; Morante, J.R.; Yamazoe, N. Effects of various metal additives on the gas sensing performances of TiO_2 nanocrystals obtained from hydrothermal treatments. *Sens. Actuators B Chem.* **2005**, *108*, 34–40. [CrossRef]
213. Henry, C.; Chapon, C.; Duriez, C. Precursor state in the chemisorption of CO on supported palladium clusters. *J. Chem. Phys.* **1991**, *95*, 700–705. [CrossRef]
214. Tsu, K.; Boudart, M. Recombination of atoms at the surface of thermocouple probes. *Can. J. Chem.* **1961**, *39*, 1239–1246. [CrossRef]
215. Boudart, M. On the nature of spilt-over hydrogen'. *J. Mol. Catal. A Chem.* **1999**, *138*, 319–321. [CrossRef]
216. Kolmakov, A.; Klenov, D.; Lilach, Y.; Stemmer, S.; Moskovits, M. Enhanced gas sensing by individual SnO2 nanowires and nanobelts functionalized with Pd catalyst particles. *Nano Lett.* **2005**, *5*, 667–673. [CrossRef]
217. Ansari, S.; Boroojerdian, P.; Sainkar, S.; Karekar, R.; Aiyer, R.; Kulkarni, S. Grain size effects on H_2 gas sensitivity of thick film resistor using SnO_2 nanoparticles. *Thin Solid Film.* **1997**, *295*, 271–276. [CrossRef]
218. Korotcenkov, G. The role of morphology and crystallographic structure of metal oxides in response of conductometric-type gas sensors. *Mater. Sci. Eng. R: Rep.* **2008**, *61*, 1–39. [CrossRef]
219. Xu, C.; Tamaki, J.; Miura, N.; Yamazoe, N. Grain size effects on gas sensitivity of porous SnO_2-based elements. *Sens. Actuators B Chem.* **1991**, *3*, 147–155. [CrossRef]
220. Timmer, B.; Olthuis, W.; Van Den Berg, A. Ammonia sensors and their applications—A review. *Sens. Actuators B Chem.* **2005**, *107*, 666–677. [CrossRef]
221. Wang, X.; Yee, S.S.; Carey, W.P. Transition between neck-controlled and grain-boundary-controlled sensitivity of metal-oxide gas sensors. *Sens. Actuators B Chem.* **1995**, *25*, 454–457. [CrossRef]
222. Barsan, N. Conduction models in gas-sensing SnO_2 layers: Grain-size effects and ambient atmosphere influence. *Sens. Actuators B Chem.* **1994**, *17*, 241–246. [CrossRef]
223. Liu, H.; Gong, S.; Hu, Y.; Liu, J.; Zhou, D. Properties and mechanism study of SnO_2 nanocrystals for H_2S thick-film sensors. *Sens. Actuators B Chem.* **2009**, *140*, 190–195. [CrossRef]

224. Rao, C.; Kulkarni, G.; Thomas, P.J.; Edwards, P.P. Size-dependent chemistry: Properties of nanocrystals. *Chem. A Eur. J.* **2002**, *8*, 28–35. [CrossRef]
225. Lu, F.; Liu, Y.; Dong, M.; Wang, X. Nanosized tin oxide as the novel material with simultaneous detection towards CO, H_2 and CH_4. *Sens. Actuators B Chem.* **2000**, *66*, 225–227. [CrossRef]
226. Serban, B.-C.; Cobianu, C.; Buiu, O.; Bumbac, M.; Dumbravescu, N.; Avramescu, V.; Nicolescu, C.M.; Brezeanu, M.; Pachiu, C.; Craciun, G. Ternary nanocomposites based on oxidized carbon nanohorns as sensing layers for room temperature resistive humidity sensing. *Materials* **2021**, *14*, 2705. [CrossRef]
227. Serban, B.-C.; Buiu, O.; Bumbac, M.; Marinescu, R.; Dumbravescu, N.; Avramescu, V.; Cobianu, C.; Nicolescu, C.M.; Brezeanu, M.; Radulescu, C. Ternary Oxidized Carbon Nanohorns/TiO_2/PVP Nanohybrid as Sensitive Layer for Chemoresistive Humidity Sensor. *Chem. Proc.* **2021**, *5*, 12.
228. Qi, Q.; Zhang, T.; Zheng, X.; Fan, H.; Liu, L.; Wang, R.; Zeng, Y. Electrical response of Sm_2O_3-doped SnO_2 to C_2H_2 and effect of humidity interference. *Sens. Actuators B Chem.* **2008**, *134*, 36–42. [CrossRef]
229. Gong, J.; Chen, Q.; Lian, M.-R.; Liu, N.-C.; Stevenson, R.G.; Adami, F. Micromachined nanocrystalline silver doped SnO_2 H_2S sensor. *Sens. Actuators B Chem.* **2006**, *114*, 32–39. [CrossRef]
230. Jing, Z.; Zhan, J. Fabrication and gas-sensing properties of porous ZnO nanoplates. *Adv. Mater.* **2008**, *20*, 4547–4551. [CrossRef]
231. Malyshev, V.; Pislyakov, A. Investigation of gas-sensitivity of sensor structures to hydrogen in a wide range of temperature, concentration and humidity of gas medium. *Sens. Actuators B Chem.* **2008**, *134*, 913–921. [CrossRef]
232. Kim, I.-D.; Rothschild, A.; Lee, B.H.; Kim, D.Y.; Jo, S.M.; Tuller, H.L. Ultrasensitive chemiresistors based on electrospun TiO_2 nanofibers. *Nano Lett.* **2006**, *6*, 2009–2013. [CrossRef]
233. Cao, M.; Wang, Y.; Chen, T.; Antonietti, M.; Niederberger, M. A highly sensitive and fast-responding ethanol sensor based on $CdIn_2O_4$ nanocrystals synthesized by a nonaqueous sol−gel route. *Chem. Mater.* **2008**, *20*, 5781–5786. [CrossRef]
234. Van Duy, N.; Van Hieu, N.; Huy, P.T.; Chien, N.D.; Thamilselvan, M.; Yi, J. Mixed SnO_2/TiO_2 included with carbon nanotubes for gas-sensing application. *Phys. E: Low-Dimens. Syst. Nanostruct.* **2008**, *41*, 258–263. [CrossRef]
235. Hasan, M.N.; Maity, S.; Sarkar, A.; Bhunia, C.T.; Acharjee, D.; Joseph, A.M. Simulation and fabrication of SAW-based gas sensor with modified surface state of active layer and electrode orientation for enhanced H_2 gas sensing. *J. Electron. Mater.* **2017**, *46*, 679. [CrossRef]
236. Sarkar, S.M.A.; Chakraborty, P.; Chakraborty, S.K. Factors Influencing on Sensitivity of the Metal Oxide Gas Sensors. *Int. J. Sci. Res.* **2017**, *6*, 372–376.
237. Chang, C.; Hon, M.; Leu, I. Influence of size and density of Au nanoparticles on ZnO nanorod arrays for sensing reducing gases. *J. Electrochem. Soc.* **2013**, *160*, B170. [CrossRef]
238. Liu, X.; Zhang, J.; Guo, X.; Wang, S.; Wu, S. Core–shell α–Fe_2O_3@ SnO_2/Au hybrid structures and their enhanced gas sensing properties. *RSC Adv.* **2012**, *2*, 1650–1655. [CrossRef]
239. Kim, H.R.; Haensch, A.; Kim, I.D.; Barsan, N.; Weimar, U.; Lee, J.H. The role of NiO doping in reducing the impact of humidity on the performance of SnO_2-Based gas sensors: Synthesis strategies, and phenomenological and spectroscopic studies. *Adv. Funct. Mater.* **2011**, *21*, 4456–4463. [CrossRef]
240. Ponzoni, A.; Comini, E.; Ferroni, M.; Sberveglieri, G. Nanostructured WO_3 deposited by modified thermal evaporation for gas-sensing applications. *Thin Solid Film* **2005**, *490*, 81–85. [CrossRef]
241. Boulova, M.; Gaskov, A.; Lucazeau, G. Tungsten oxide reactivity versus CH_4, CO and NO_2 molecules studied by Raman spectroscopy. *Sens. Actuators B Chem.* **2001**, *81*, 99–106. [CrossRef]
242. Tamaki, J.; Miyaji, A.; Makinodan, J.; Ogura, S.; Konishi, S. Effect of micro-gap electrode on detection of dilute NO_2 using WO_3 thin film microsensors. *Sens. Actuators B Chem.* **2005**, *108*, 202–206. [CrossRef]
243. Vallejos, S.; Khatko, V.; Calderer, J.; Gracia, I.; Cané, C.; Llobet, E.; Correig, X. Micro-machined WO_3-based sensors selective to oxidizing gases. *Sens. Actuators B Chem.* **2008**, *132*, 209–215. [CrossRef]
244. Siciliano, T.; Tepore, A.; Micocci, G.; Serra, A.; Manno, D.; Filippo, E. WO_3 gas sensors prepared by thermal oxidization of tungsten. *Sens. Actuators B Chem.* **2008**, *133*, 321–326. [CrossRef]
245. Yang, J.-C.; Dutta, P.K.J.S. Solution-based synthesis of efficient WO3 sensing electrodes for high temperature potentiometric NOx sensors. *Sens. Actuators B Chem.* **2009**, *136*, 523–529. [CrossRef]
246. Ferroni, M.; Boscarino, D.; Comini, E.; Gnani, D.; Guidi, V.; Martinelli, G.; Nelli, P.; Rigato, V.; Sberveglieri, G. Nanosized thin films of tungsten-titanium mixed oxides as gas sensors. *Sens. Actuators B Chem.* **1999**, *58*, 289–294. [CrossRef]
247. Guidi, V.; Boscarino, D.; Comini, E.; Faglia, G.; Ferroni, M.; Malagu, C.; Martinelli, G.; Rigato, V.; Sberveglieri, G. Preparation and characterisation of titanium–tungsten sensors. *Sens. Actuators B Chem.* **2000**, *65*, 264–266. [CrossRef]
248. Comini, E.; Ferroni, M.; Guidi, V.; Faglia, G.; Martinelli, G.; Sberveglieri, G.J.S. Nanostructured mixed oxides compounds for gas sensing applications. *Sens. Actuators B Chem.* **2002**, *84*, 26–32. [CrossRef]
249. Xia, H.; Wang, Y.; Kong, F.; Wang, S.; Zhu, B.; Guo, X.; Zhang, J.; Wang, Y.; Wu, S. Au-doped WO_3-based sensor for NO_2 detection at low operating temperature. *Sens. Actuators B Chem.* **2008**, *134*, 133–139. [CrossRef]
250. Marquis, B.T.; Vetelino, J.F. A semiconducting metal oxide sensor array for the detection of NO_x and NH_3. *Sens. Actuators B Chem.* **2001**, *77*, 100–110. [CrossRef]
251. Penza, M.; Martucci, C.; Cassano, G. NOx gas sensing characteristics of WO_3 thin films activated by noble metals (Pd, Pt, Au) layers. *Sens. Actuators B Chem.* **1998**, *50*, 52–59. [CrossRef]

252. Kawasaki, H.; Ueda, T.; Suda, Y.; Ohshima, T. Properties of metal doped tungsten oxide thin films for NO_x gas sensors grown by PLD method combined with sputtering process. *Sens. Actuators B Chem.* **2004**, *100*, 266–269. [CrossRef]
253. Filippini, D.; Fraigi, L.; Aragón, R.; Weimar, U. Thick film Au-gate field-effect devices sensitive to NO_2. *Sens. Actuators B Chem.* **2002**, *81*, 296–300. [CrossRef]
254. Yang, J.-C.; Dutta, P.K. Promoting selectivity and sensitivity for a high temperature YSZ-based electrochemical total NOx sensor by using a Pt-loaded zeolite Y filter. *Sens. Actuators B Chem.* **2007**, *125*, 30–39. [CrossRef]
255. Siciliano, T.; Di Giulio, M.; Tepore, M.; Filippo, E.; Micocci, G.; Tepore, A. Tellurium sputtered thin films as NO_2 gas sensors. *Sens. Actuators B Chem.* **2008**, *135*, 250–254. [CrossRef]
256. Siciliano, T.; Di Giulio, M.; Tepore, M.; Filippo, E.; Micocci, G.; Tepore, A. Room temperature NO_2 sensing properties of reactively sputtered TeO_2 thin films. *Sens. Actuators B Chem.* **2009**, *137*, 644–648. [CrossRef]
257. Kim, T.-S.; Lee, Y.; Xu, W.; Kim, Y.H.; Kim, M.; Min, S.-Y.; Kim, T.H.; Jang, H.W.; Lee, T.-W. Direct-printed nanoscale metal-oxide-wire electronics. *Nano Energy* **2019**, *58*, 437–446. [CrossRef]
258. Matsuguchi, M.; Tamai, K.; Sakai, Y. SO_2 gas sensors using polymers with different amino groups. *Sens. Actuators B Chem.* **2001**, *77*, 363–367. [CrossRef]
259. Dultsev, F.; Sveshnikova, L. The use of the substituted imidazoline radical as a receptor for sulphur dioxide gas sensor. *Sens. Actuators B Chem.* **2007**, *120*, 434–438. [CrossRef]
260. Benmakroha, F.; Boudjerda, T.; Boufenar, R.; Allag, H.; Djerboua, F.; McCallum, J.J. Monitoring of sulfur dioxide using a piezoelectric crystal based controller. *Analyst* **1993**, *118*, 401–406. [CrossRef]
261. Berger, F.; Fromm, M.; Chambaudet, A.; Planade, R. Tin dioxide-based gas sensors for SO_2 detection: A chemical interpretation of the increase in sensitivity obtained after a primary detection. *Sens. Actuators B Chem.* **1997**, *45*, 175–181. [CrossRef]
262. Torvela, H.; Huusko, J.; Lantto, V. Reduction of the interference caused by NO and SO_2 in the CO response of Pd-catalysed SnO_2 combustion gas sensors. *Sens. Actuators B Chem.* **1991**, *4*, 479–484. [CrossRef]
263. Stankova, M.; Vilanova, X.; Calderer, J.; Llobet, E.; Ivanov, P.; Gràcia, I.; Cané, C.; Correig, X. Detection of SO_2 and H_2S in CO_2 stream by means of WO_3-based micro-hotplate sensors. *Sens. Actuators B Chem.* **2004**, *102*, 219–225. [CrossRef]
264. Penza, M.; Cassano, G.; Tortorella, F. Gas recognition by activated WO_3 thin-film sensors array. *Sens. Actuators B Chem.* **2001**, *81*, 115–121. [CrossRef]
265. Liang, X.; Zhong, T.; Quan, B.; Wang, B.; Guan, H. Solid-state potentiometric SO_2 sensor combining NASICON with V_2O_5-doped TiO_2 electrode. *Sens. Actuators B Chem.* **2008**, *134*, 25–30. [CrossRef]
266. Guo, Z.; Chen, G.; Zeng, G.; Liu, L.; Zhang, C. Metal oxides and metal salt nanostructures for hydrogen sulfide sensing: Mechanism and sensing performance. *RSC Adv.* **2015**, *5*, 54793–54805. [CrossRef]
267. Mirzaei, A.; Kim, S.S.; Kim, H.W. Resistance-based H_2S gas sensors using metal oxide nanostructures: A review of recent advances. *J. Hazard. Mater.* **2018**, *357*, 314–331. [CrossRef]
268. Joshi, N.; Hayasaka, T.; Liu, Y.; Liu, H.; Oliveira, O.N.; Lin, L. A review on chemiresistive room temperature gas sensors based on metal oxide nanostructures, graphene and 2D transition metal dichalcogenides. *Microchim. Acta* **2018**, *185*, 213. [CrossRef] [PubMed]
269. Llobet, E.; Brunet, J.; Pauly, A.; Ndiaye, A.; Varenne, C. Nanomaterials for the selective detection of hydrogen sulfide in air. *Sensors* **2017**, *17*, 391. [CrossRef] [PubMed]
270. He, M.; Xie, L.; Zhao, X.; Hu, X.; Li, S.; Zhu, Z.-G. Highly sensitive and selective H_2S gas sensors based on flower-like WO_3/CuO composites operating at low/room temperature. *J. Alloys Compd.* **2019**, *788*, 36–43. [CrossRef]
271. Hangarter, C.M.; Chartuprayoon, N.; Hernández, S.C.; Choa, Y.; Myung, N.V. Hybridized conducting polymer chemiresistive nano-sensors. *Nano Today* **2013**, *8*, 39–55. [CrossRef]
272. Duc, C.; Boukhenane, M.-L.; Wojkiewicz, J.-L.; Redon, N. Hydrogen Sulfide Detection by Sensors Based on Conductive Polymers: A Review. *Front. Mater.* **2020**, *7*, 215. [CrossRef]
273. Rout, C.S.; Hegde, M.; Rao, C.R. H_2S sensors based on tungsten oxide nanostructures. *Sens. Actuators B Chem.* **2008**, *128*, 488–493. [CrossRef]
274. Tao, W.-H.; Tsai, C.-H. H2S sensing properties of noble metal doped WO_3 thin film sensor fabricated by micromachining. *Sens. Actuators B Chem.* **2002**, *81*, 237–247. [CrossRef]
275. Solis, J.; Saukko, S.; Kish, L.; Granqvist, C.; Lantto, V. Nanocrystalline tungsten oxide thick-films with high sensitivity to H_2S at room temperature. *Sens. Actuators B Chem.* **2001**, *77*, 316–321. [CrossRef]
276. Ruokamo, I.; Kärkkäinen, T.; Huusko, J.; Ruokanen, T.; Blomberg, M.; Torvela, H.; Lantto, V. H_2S response of WO_3 thin-film sensors manufactured by silicon processing technology. *Sens. Actuators B Chem.* **1994**, *19*, 486–488. [CrossRef]
277. Frühberger, B.; Grunze, M.; Dwyer, D. Surface chemistry of H_2S-sensitive tungsten oxide films. *Sens. Actuators B Chem.* **1996**, *31*, 167–174. [CrossRef]
278. Vuong, D.D.; Sakai, G.; Shimanoe, K.; Yamazoe, N. Hydrogen sulfide gas sensing properties of thin films derived from SnO_2 sols different in grain size. *Sens. Actuators B Chem.* **2005**, *105*, 437–442. [CrossRef]
279. Shuping, G.; Jing, X.; Jianqiao, L.; Dongxiang, Z.J.S.; Chemical, A.B. Highly sensitive SnO_2 thin film with low operating temperature prepared by sol–gel technique. *Sens. Actuators B Chem.* **2008**, *134*, 57–61. [CrossRef]
280. Ghimbeu, C.M.; Lumbreras, M.; Siadat, M.; van Landschoot, R.C.; Schoonman, J. Electrostatic sprayed SnO_2 and Cu-doped SnO_2 films for H_2S detection. *Sens. Actuators B Chem.* **2008**, *133*, 694–698. [CrossRef]

281. Liang, X.; He, Y.; Liu, F.; Wang, B.; Zhong, T.; Quan, B.; Lu, G. Solid-state potentiometric H_2S sensor combining NASICON with Pr_6O_{11}-doped SnO_2 electrode. *Sens. Actuators B Chem.* **2007**, *125*, 544–549. [CrossRef]
282. Wang, C.; Chu, X.; Wu, M. Detection of H2S down to ppb levels at room temperature using sensors based on ZnO nanorods. *Sens. Actuators B Chem.* **2006**, *113*, 320–323. [CrossRef]
283. Liu, Z.; Fan, T.; Zhang, D.; Gong, X.; Xu, J. Hierarchically porous ZnO with high sensitivity and selectivity to H_2S derived from biotemplates. *Sens. Actuators B Chem.* **2009**, *136*, 499–509. [CrossRef]
284. Wallace, K.J.; Cordero, S.R.; Tan, C.P.; Lynch, V.M.; Anslyn, E.V. A colorimetric response to hydrogen sulfide. *Sens. Actuators B Chem.* **2007**, *120*, 362–367. [CrossRef]
285. Jain, G.; Patil, L. CuO-doped BSST thick film resistors for ppb level H_2S gas sensing at room temperature. *Sens. Actuators B Chem.* **2007**, *123*, 246–253. [CrossRef]
286. Wang, Y.; Wang, S.; Zhao, Y.; Zhu, B.; Kong, F.; Wang, D.; Wu, S.; Huang, W.; Zhang, S. H_2S sensing characteristics of Pt-doped α-Fe_2O_3 thick film sensors. *Sens. Actuators B Chem.* **2007**, *125*, 79–84. [CrossRef]
287. Kapse, V.; Ghosh, S.; Raghuwanshi, F.; Kapse, S. Enhanced H2S sensing characteristics of La-doped In_2O_3: Effect of Pd sensitization. *Sens. Actuators B Chem.* **2009**, *137*, 681–686. [CrossRef]
288. Kaur, M.; Jain, N.; Sharma, K.; Bhattacharya, S.; Roy, M.; Tyagi, A.; Gupta, S.; Yakhmi, J. Room-temperature H_2S gas sensing at ppb level by single crystal In_2O_3 whiskers. *Sens. Actuators B Chem.* **2008**, *133*, 456–461. [CrossRef]
289. Wang, Y.; Wang, Y.; Cao, J.; Kong, F.; Xia, H.; Zhang, J.; Zhu, B.; Wang, S.; Wu, S. Low-temperature H_2S sensors based on Ag-doped α-Fe_2O_3 nanoparticles. *Sens. Actuators B Chem.* **2008**, *131*, 183–189. [CrossRef]
290. Fam, D.W.H.; Tok, A.I.Y.; Palaniappan, A.; Nopphawan, P.; Lohani, A.; Mhaisalkar, S.J.S.; Chemical, A.B. Selective sensing of hydrogen sulphide using silver nanoparticle decorated carbon nanotubes. *Sens. Actuators B Chem.* **2009**, *138*, 189–192. [CrossRef]
291. Jain, G.; Patil, L.; Wagh, M.; Patil, D.; Patil, S.; Amalnerkar, D. Surface modified $BaTiO_3$ thick film resistors as H_2S gas sensors. *Sens. Actuators B Chem.* **2006**, *117*, 159–165. [CrossRef]
292. Sarma, T.; Tao, S. An active core fiber optic sensor for detecting trace H_2S at high temperature using a cadmium oxide doped porous silica optical fiber as a transducer. *Sens. Actuators B Chem.* **2007**, *127*, 471–479. [CrossRef]
293. Morazzoni, F.; Scotti, R.; Origoni, L.; D'Arienzo, M.; Jimenez, I.; Cornet, A.; Morante, J. Mechanism of NH3 interaction with transition metal-added nanosized WO_3 for gas sensing: In situ electron paramagnetic resonance study. *Catal. Today* **2007**, *126*, 169–176. [CrossRef]
294. Tong, M.; Dai, G.; Gao, D. WO3 thin film sensor prepared by sol–gel technique and its low-temperature sensing properties to trimethylamine. *Mater. Chem. Phys.* **2001**, *69*, 176–179. [CrossRef]
295. Bendahan, M.; Lauque, P.; Seguin, J.-L.; Aguir, K.; Knauth, P. Development of an ammonia gas sensor. *Sens. Actuators B Chem.* **2003**, *95*, 170–176. [CrossRef]
296. Wagh, M.; Jain, G.; Patil, D.; Patil, S.; Patil, L. Modified zinc oxide thick film resistors as NH_3 gas sensor. *Sens. Actuators B Chem.* **2006**, *115*, 128–133. [CrossRef]
297. Wang, Y.-D.; Wu, X.-H.; Su, Q.; Li, Y.-F.; Zhou, Z.-L. Ammonia-sensing characteristics of Pt and SiO_2 doped SnO_2 materials. *Solid-State Electron.* **2001**, *45*, 347–350. [CrossRef]
298. Suryawanshi, D.; Patil, D.; Patil, L. Fe_2O_3-activated Cr_2O_3 thick films as temperature dependent gas sensors. *Sens. Actuators B Chem.* **2008**, *134*, 579–584. [CrossRef]
299. Patil, D.; Patil, L.; Patil, P. Cr_2O_3-activated ZnO thick film resistors for ammonia gas sensing operable at room temperature. *Sens. Actuators B Chem.* **2007**, *126*, 368–374. [CrossRef]
300. Li, G.-J.; Kawi, S. Synthesis, characterization and sensing application of novel semiconductor oxides. *Talanta* **1998**, *45*, 759–766. [CrossRef] [PubMed]
301. Sunny, A.I.; Zhao, A.; Li, L.; Sakiliba, S.K. Low-cost IoT-based sensor system: A case study on harsh environmental monitoring. *Sensors* **2020**, *21*, 214. [CrossRef]
302. Majhi, S.M.; Mirzaei, A.; Kim, H.W.; Kim, S.S.; Kim, T.W. Recent advances in energy-saving chemiresistive gas sensors: A review. *Nano Energy* **2021**, *79*, 105369. [CrossRef] [PubMed]
303. Sekimoto, S.; Nakagawa, H.; Okazaki, S.; Fukuda, K.; Asakura, S.; Shigemori, T.; Takahashi, S. A fiber-optic evanescent-wave hydrogen gas sensor using palladium-supported tungsten oxide. *Sens. Actuators B Chem.* **2000**, *66*, 142–145. [CrossRef]
304. Hellegouarch, F.; Arefi-Khonsari, F.; Planade, R.; Amouroux, J. PECVD prepared SnO_2 thin films for ethanol sensors. *Sens. Actuators B Chem.* **2001**, *73*, 27–34. [CrossRef]
305. Pourfayaz, F.; Khodadadi, A.; Mortazavi, Y.; Mohajerzadeh, S. CeO_2 doped SnO_2 sensor selective to ethanol in presence of CO, LPG and CH_4. *Sens. Actuators B Chem.* **2005**, *108*, 172–176. [CrossRef]
306. Jain, K.; Pant, R.; Lakshmikumar, S. Effect of Ni doping on thick film SnO_2 gas sensor. *Sens. Actuators B Chem.* **2006**, *113*, 823–829. [CrossRef]
307. Wagh, M.; Jain, G.; Patil, D.; Patil, S.; Patil, L. Surface customization of SnO_2 thick films using RuO_2 as a surfactant for the LPG response. *Sens. Actuators B Chem.* **2007**, *122*, 357–364. [CrossRef]
308. Ionescu, R.; Hoel, A.; Granqvist, C.; Llobet, E.; Heszler, P. Ethanol and H_2S gas detection in air and in reducing and oxidising ambience: Application of pattern recognition to analyse the output from temperature-modulated nanoparticulate WO_3 gas sensors. *Sens. Actuators B Chem.* **2005**, *104*, 124–131. [CrossRef]

309. Khadayate, R.; Sali, J.; Patil, P. Acetone vapor sensing properties of screen printed WO_3 thick films. *Talanta* **2007**, *72*, 1077–1081. [CrossRef] [PubMed]
310. Cao, X.; Wu, W.; Chen, N.; Peng, Y.; Liu, Y. An ether sensor utilizing cataluminescence on nanosized $ZnWO_4$. *Sens. Actuators B Chem.* **2009**, *137*, 83–87. [CrossRef]
311. de Lacy Costello, B.; Ewen, R.; Guernion, N.; Ratcliffe, N. Highly sensitive mixed oxide sensors for the detection of ethanol. *Sens. Actuators B Chem.* **2002**, *87*, 207–210. [CrossRef]
312. Xu, J.; Han, J.; Zhang, Y.; Sun, Y.A.; Xie, B. Studies on alcohol sensing mechanism of ZnO based gas sensors. *Sens. Actuators B Chem.* **2008**, *132*, 334–339. [CrossRef]
313. Zhao, S.; Sin, J.K.; Xu, B.; Zhao, M.; Peng, Z.; Cai, H. A high performance ethanol sensor based on field-effect transistor using a $LaFeO_3$ nano-crystalline thin-film as a gate electrode. *Sens. Actuators B Chem.* **2000**, *64*, 83–87. [CrossRef]
314. Liu, X.; Cheng, B.; Hu, J.; Qin, H.; Jiang, M. Preparation, structure, resistance and methane-gas sensing properties of nominal $La_{1-x}Mg_xFeO_3$. *Sens. Actuators B Chem.* **2008**, *133*, 340–344. [CrossRef]
315. Ajami, S.; Mortazavi, Y.; Khodadadi, A.; Pourfayaz, F.; Mohajerzadeh, S. Highly selective sensor to CH_4 in presence of CO and ethanol using $LaCoO_3$ perovskite filter with Pt/SnO_2. *Sens. Actuators B Chem.* **2006**, *117*, 420–425. [CrossRef]
316. Xuan, Y.; Hu, J.; Xu, K.; Hou, X.; Lv, Y. Development of sensitive carbon disulfide sensor by using its cataluminescence on nanosized-CeO_2. *Sens. Actuators B Chem.* **2009**, *136*, 218–223. [CrossRef]
317. Kida, T.; Minami, T.; Kishi, S.; Yuasa, M.; Shimanoe, K.; Yamazoe, N. Planar-type $BiCuVO_x$ solid electrolyte sensor for the detection of volatile organic compounds. *Sens. Actuators B Chem.* **2009**, *137*, 147–153. [CrossRef]
318. Jinkawa, T.; Sakai, G.; Tamaki, J.; Miura, N.; Yamazoe, N. Relationship between ethanol gas sensitivity and surface catalytic property of tin oxide sensors modified with acidic or basic oxides. *J. Mol. Catal. A: Chem.* **2000**, *155*, 193–200. [CrossRef]
319. Tianshu, Z.; Hing, P.; Li, Y.; Jiancheng, Z. Selective detection of ethanol vapor and hydrogen using Cd-doped SnO_2-based sensors. *Sens. Actuators B Chem.* **1999**, *60*, 208–215. [CrossRef]
320. Lv, P.; Tang, Z.A.; Yu, J.; Zhang, F.T.; Wei, G.F.; Huang, Z.X.; Hu, Y. Study on a micro-gas sensor with SnO_2–NiO sensitive film for indoor formaldehyde detection. *Sens. Actuators B Chem.* **2008**, *132*, 74–80. [CrossRef]
321. Jun, L.; Chen, Q.; Fu, W.; Yang, Y.; Zhu, W.; Zhang, J. Electrospun Yb-doped In_2O_3 nanofiber field-effect transistors for highly sensitive ethanol sensors. *ACS Appl. Mater. Interfaces* **2020**, *12*, 38425–38434. [CrossRef]
322. Chen, A.; Huang, X.; Tong, Z.; Bai, S.; Luo, R.; Liu, C.C. Preparation, characterization and gas-sensing properties of SnO_2–In_2O_3 nanocomposite oxides. *Sens. Actuators B Chem.* **2006**, *115*, 316–321. [CrossRef]
323. Her, Y.-C.; Chiang, C.-K.; Jean, S.-T.; Huang, S.-L. Self-catalytic growth of hierarchical In_2O_3 nanostructures on SnO_2 nanowires and their CO sensing properties. *CrystEngComm* **2012**, *14*, 1296–1300. [CrossRef]
324. Kuang, Q.; Lao, C.-S.; Li, Z.; Liu, Y.-Z.; Xie, Z.-X.; Zheng, L.-S.; Wang, Z.L. Enhancing the photon-and gas-sensing properties of a single SnO_2 nanowire based nanodevice by nanoparticle surface functionalization. *J. Phys. Chem. C* **2008**, *112*, 11539–11544. [CrossRef]
325. Choi, U.-S.; Sakai, G.; Shimanoe, K.; Yamazoe, N. Sensing properties of Au-loaded SnO_2–Co_3O_4 composites to CO and H_2. *Sens. Actuators B Chem.* **2005**, *107*, 397–401. [CrossRef]
326. Moon, W.J.; Yu, J.H.; Choi, G.M. The CO and H_2 gas selectivity of CuO-doped SnO_2–ZnO composite gas sensor. *Sens. Actuators B Chem.* **2002**, *87*, 464–470. [CrossRef]
327. Huang, H.; Gong, H.; Chow, C.L.; Guo, J.; White, T.J.; Tse, M.S.; Tan, O.K. Low-temperature growth of SnO_2 nanorod arrays and tunable n–p–n sensing response of a ZnO/SnO_2 heterojunction for exclusive hydrogen sensors. *Adv. Funct. Mater.* **2011**, *21*, 2680–2686. [CrossRef]
328. Ansari, Z.; Ansari, S.; Ko, T.; Oh, J.-H. Effect of MoO_3 doping and grain size on SnO_2-enhancement of sensitivity and selectivity for CO and H2 gas sensing. *Sens. Actuators B Chem.* **2002**, *87*, 105–114. [CrossRef]
329. Kosc, I.; Hotovy, I.; Rehacek, V.; Griesseler, R.; Predanocy, M.; Wilke, M.; Spiess, L. Sputtered TiO_2 thin films with NiO additives for hydrogen detection. *Appl. Surf. Sci.* **2013**, *269*, 110–115. [CrossRef]
330. Tien, L.; Norton, D.; Gila, B.; Pearton, S.; Wang, H.-T.; Kang, B.; Ren, F. Detection of hydrogen with SnO_2-coated ZnO nanorods. *Appl. Surf. Sci.* **2007**, *253*, 4748–4752. [CrossRef]
331. Choi, S.-W.; Park, J.Y.; Kim, S.S. Synthesis of SnO_2–ZnO core–shell nanofibers via a novel two-step process and their gas sensing properties. *Nanotechnology* **2009**, *20*, 465603. [CrossRef]
332. Liangyuan, C.; Shouli, B.; Guojun, Z.; Dianqing, L.; Aifan, C.; Liu, C.C. Synthesis of ZnO–SnO_2 nanocomposites by microemulsion and sensing properties for NO_2. *Sens. Actuators B Chem.* **2008**, *134*, 360–366. [CrossRef]
333. Bai, S.; Li, D.; Han, D.; Luo, R.; Chen, A.; Chung, C.L. Preparation, characterization of WO_3–SnO_2 nanocomposites and their sensing properties for NO_2. *Sens. Actuators B Chem.* **2010**, *150*, 749–755. [CrossRef]
334. Somacescu, S.; Dinescu, A.; Stanoiu, A.; Simion, C.E.; Moreno, J.M.C. Hydrothermal synthesis of ZnO–Eu_2O_3 binary oxide with straight strips morphology and sensitivity to NO_2 gas. *Mater. Lett.* **2012**, *89*, 219–222. [CrossRef]
335. Cui, G.; Zhang, M.; Zou, G. Resonant tunneling modulation in quasi-2D Cu_2O/SnO_2 p-n horizontal-multi-layer heterostructure for room temperature H_2S sensor application. *Sci. Rep.* **2013**, *3*, 1250. [CrossRef]
336. Verma, M.K.; Gupta, V. SnO2–CuO nanocomposite thin film sensor for fast detection of H_2S gas. *J. Exp. Nanosci.* **2013**, *8*, 326–331. [CrossRef]

337. Fang, G.; Liu, Z.; Liu, C.; Yao, K.-L. Room temperature H2S sensing properties and mechanism of CeO_2–SnO_2 sol–gel thin films. *Sens. Actuators B Chem.* **2000**, *66*, 46–48. [CrossRef]
338. Wagh, M.; Patil, L.; Seth, T.; Amalnerkar, D. Surface cupricated SnO_2–ZnO thick films as a H_2S gas sensor. *Mater. Chem. Phys.* **2004**, *84*, 228–233. [CrossRef]
339. Wang, L.; Kang, Y.; Wang, Y.; Zhu, B.; Zhang, S.; Huang, W.; Wang, S. CuO nanoparticle decorated ZnO nanorod sensor for low-temperature H2S detection. *Mater. Sci. Eng. C* **2012**, *32*, 2079–2085. [CrossRef] [PubMed]
340. Tang, H.; Yan, M.; Zhang, H.; Li, S.; Ma, X.; Wang, M.; Yang, D. A selective NH_3 gas sensor based on Fe_2O_3–ZnO nanocomposites at room temperature. *Sens. Actuators B Chem.* **2006**, *114*, 910–915. [CrossRef]
341. Zeng, Y.; Bing, Y.-F.; Liu, C.; Zheng, W.-T.; Zou, G.-T. Self-assembly of hierarchical $ZnSnO_3$-SnO_2 nanoflakes and their gas sensing properties. *Trans. Nonferrous Met. Soc. China* **2012**, *22*, 2451–2458. [CrossRef]
342. Kim, K.-W.; Cho, P.-S.; Kim, S.-J.; Lee, J.-H.; Kang, C.-Y.; Kim, J.-S.; Yoon, S.-J. The selective detection of C_2H_5OH using SnO_2–ZnO thin film gas sensors prepared by combinatorial solution deposition. *Sens. Actuators B Chem.* **2007**, *123*, 318–324. [CrossRef]
343. Rumyantseva, M.; Kovalenko, V.; Gaskov, A.; Makshina, E.; Yuschenko, V.; Ivanova, I.; Ponzoni, A.; Faglia, G.; Comini, E. Nanocomposites SnO_2/Fe_2O_3: Sensor and catalytic properties. *Sens. Actuators B Chem.* **2006**, *118*, 208–214. [CrossRef]
344. Zhang, X.-J.; Qiao, G.-J. High performance ethanol sensing films fabricated from ZnO and In_2O_3 nanofibers with a double-layer structure. *Appl. Surf. Sci.* **2012**, *258*, 6643–6647. [CrossRef]
345. Yu, X.; Zhang, G.; Cao, H.; An, X.; Wang, Y.; Shu, Z.; An, X.; Hua, F. ZnO@ ZnS hollow dumbbells–graphene composites as high-performance photocatalysts and alcohol sensors. *New J. Chem.* **2012**, *36*, 2593–2598. [CrossRef]
346. Hu, Y.; Zhou, X.; Han, Q.; Cao, Q.; Huang, Y. Sensing properties of CuO–ZnO heterojunction gas sensors. *Mater. Sci. Eng. B* **2003**, *99*, 41–43. [CrossRef]
347. Zeng, W.; Liu, T.; Wang, Z. Sensitivity improvement of TiO_2-doped SnO_2 to volatile organic compounds. *Phys. E Low Dimens. Syst. Nanostructures* **2010**, *43*, 633–638. [CrossRef]
348. Liu, Y.; Zhu, G.; Chen, J.; Xu, H.; Shen, X.; Yuan, A. Co_3O_4/ZnO nanocomposites for gas-sensing applications. *Appl. Surf. Sci.* **2013**, *265*, 379–384. [CrossRef]
349. Pimtong-Ngam, Y.; Jiemsirilers, S.; Supothina, S. Preparation of tungsten oxide–tin oxide nanocomposites and their ethylene sensing characteristics. *Sens. Actuators A Phys.* **2007**, *139*, 7–11. [CrossRef]
350. Galatsis, K.; Li, Y.; Wlodarski, W.; Comini, E.; Sberveglieri, G.; Cantalini, C.; Santucci, S.; Passacantando, M.J.S.; Chemical, A.B. Comparison of single and binary oxide MoO_3, TiO_2 and WO_3 sol–gel gas sensors. *Sens. Actuators B Chem.* **2002**, *83*, 276–280. [CrossRef]
351. Hidalgo, P.; Castro, R.H.; Coelho, A.C.; Gouvêa, D. Surface segregation and consequent SO_2 sensor response in SnO_2- NiO. *Chem. Mater.* **2005**, *17*, 4149–4153. [CrossRef]
352. Patil, D.; Patil, L. Cr_2O_3-modified ZnO thick film resistors as LPG sensors. *Talanta* **2009**, *77*, 1409–1414. [CrossRef] [PubMed]
353. Zhang, W.-H.; Zhang, W.-D. Fabrication of SnO_2–ZnO nanocomposite sensor for selective sensing of trimethylamine and the freshness of fishes. *Sens. Actuators B Chem.* **2008**, *134*, 403–408. [CrossRef]
354. Heiland, G. Zum Einfluß von adsorbiertem Sauerstoff auf die elektrische Leitfähigkeit von Zinkoxydkristallen. *Z. Für Phys.* **1954**, *138*, 459–464. [CrossRef]
355. Bielański, A.; Dereń, J.; Haber, J. Electric conductivity and catalytic activity of semiconducting oxide catalysts. *Nature* **1957**, *179*, 668–669. [CrossRef]
356. Shimizu, Y.; Egashira, M. Basic aspects and challenges of semiconductor gas sensors. *MRS Bull.* **1999**, *24*, 18–24. [CrossRef]
357. Strässler, S.; Reis, A. Simple models for n-type metal oxide gas sensors. *Sens. Actuators* **1983**, *4*, 465–472. [CrossRef]
358. Wang, B.; Zhu, L.; Yang, Y.; Xu, N.; Yang, G. Fabrication of a SnO_2 nanowire gas sensor and sensor performance for hydrogen. *J. Phys. Chem. C* **2008**, *112*, 6643–6647. [CrossRef]
359. Sysoev, V.; Schneider, T.; Goschnick, J.; Kiselev, I.; Habicht, W.; Hahn, H.; Strelcov, E.; Kolmakov, A.J.S.; Chemical, A.B. Percolating SnO_2 nanowire network as a stable gas sensor: Direct comparison of long-term performance versus SnO_2 nanoparticle films. *Sens. Actuators B Chem.* **2009**, *139*, 699–703. [CrossRef]
360. Gyger, F.; Hübner, M.; Feldmann, C.; Barsan, N.; Weimar, U. Nanoscale SnO_2 hollow spheres and their application as a gas-sensing material. *Chem. Mater.* **2010**, *22*, 4821–4827. [CrossRef]
361. Epifani, M.; Prades, J.D.; Comini, E.; Pellicer, E.; Avella, M.; Siciliano, P.; Faglia, G.; Cirera, A.; Scotti, R.; Morazzoni, F. The role of surface oxygen vacancies in the NO_2 sensing properties of SnO_2 nanocrystals. *J. Phys. Chem. C* **2008**, *112*, 19540–19546. [CrossRef]
362. Li, L.-L.; Zhang, W.-M.; Yuan, Q.; Li, Z.-X.; Fang, C.-J.; Sun, L.-D.; Wan, L.-J.; Yan, C.-H. Room temperature ionic liquids assisted green synthesis of nanocrystalline porous SnO_2 and their gas sensor behaviors. *Cryst. Growth Des.* **2008**, *8*, 4165–4172. [CrossRef]
363. Wang, Q.; Zhang, L.-S.; Wu, J.-F.; Wang, W.D.; Song, W.-G.; Wang, W. A parallel solid-state NMR and sensor property study on flower-like nanostructured SnO_2. *J. Phys. Chem. C* **2010**, *114*, 22671–22676. [CrossRef]
364. Chen, D.; Xu, J.; Xie, Z.; Shen, G. Nanowires assembled SnO_2 nanopolyhedrons with enhanced gas sensing properties. *ACS Appl. Mater. Interfaces* **2011**, *3*, 2112–2117. [CrossRef]
365. Zhang, J.; Wang, S.; Xu, M.; Wang, Y.; Xia, H.; Zhang, S.; Guo, X.; Wu, S. Polypyrrole-coated SnO_2 hollow spheres and their application for ammonia sensor. *J. Phys. Chem. C* **2009**, *113*, 1662–1665. [CrossRef]
366. Pan, J.; Ganesan, R.; Shen, H.; Mathur, S. Plasma-modified SnO_2 nanowires for enhanced gas sensing. *J. Phys. Chem. C* **2010**, *114*, 8245–8250. [CrossRef]

367. Xue, X.; Chen, Z.; Ma, C.; Xing, L.; Chen, Y.; Wang, Y.; Wang, T. One-step synthesis and gas-sensing characteristics of uniformly loaded Pt@ SnO_2 nanorods. *J. Phys. Chem. C* **2010**, *114*, 3968–3972. [CrossRef]
368. Wei, W.; Dai, Y.; Huang, B. Role of Cu doping in SnO_2 sensing properties toward H_2S. *J. Phys. Chem.* **2011**, *115*, 18597–18602. [CrossRef]
369. Li, W.; Shen, C.; Wu, G.; Ma, Y.; Gao, Z.; Xia, X.; Du, G. New model for a Pd-doped SnO_2-based CO gas sensor and catalyst studied by online in-situ X-ray photoelectron spectroscopy. *J. Phys. Chem. C* **2011**, *115*, 21258–21263. [CrossRef]
370. Umar, A.; Rahman, M.M.; Kim, S.H.; Hahn, Y.-B. Zinc oxide nanonail based chemical sensor for hydrazine detection. *Chem. Commun.* **2007**, *2*, 166–168. [CrossRef] [PubMed]
371. Ahsanulhaq, Q.; Kim, J.; Lee, J.; Hahn, Y. Electrical and gas sensing properties of ZnO nanorod arrays directly grown on a four-probe electrode system. *Electrochem. Commun.* **2010**, *12*, 475–478. [CrossRef]
372. Li, Y.-J.; Li, K.-M.; Wang, C.-Y.; Kuo, C.-I.; Chen, L.-J. Low-temperature electrodeposited Co-doped ZnO nanorods with enhanced ethanol and CO sensing properties. *Sens. Actuators B Chem.* **2012**, *161*, 734–739. [CrossRef]
373. Choi, S.-W.; Kim, S.S. Room temperature CO sensing of selectively grown networked ZnO nanowires by Pd nanodot functionalization. *Sens. Actuators B Chem.* **2012**, *168*, 8–13. [CrossRef]
374. Arnold, S.; Prokes, S.; Perkins, F.; Zaghloul, M. Design and performance of a simple, room-temperature Ga_2O_3 nanowire gas sensor. *Appl. Phys. Lett.* **2009**, *95*, 10. [CrossRef]
375. Yan, S.; Wan, L.; Li, Z.; Zhou, Y.; Zou, Z. Synthesis of a mesoporous single crystal Ga 2 O 3 nanoplate with improved photoluminescence and high sensitivity in detecting CO. *Chem. Commun.* **2010**, *46*, 6388–6390. [CrossRef]
376. Nguyen, H.; El-Safty, S.A. Meso-and macroporous Co_3O_4 nanorods for effective VOC gas sensors. *J. Phys. Chem. C* **2011**, *115*, 8466–8474. [CrossRef]
377. Zhu, C.-L.; Yu, H.-L.; Zhang, Y.; Wang, T.-S.; Ouyang, Q.-Y.; Qi, L.-H.; Chen, Y.-J.; Xue, X.-Y. Fe_2O_3/TiO_2 tube-like nanostructures: Synthesis, structural transformation and the enhanced sensing properties. *ACS Appl. Mater. Interfaces* **2012**, *4*, 665–671. [CrossRef]
378. Zheng, W.; Lu, X.; Wang, W.; Li, Z.; Zhang, H.; Wang, Y.; Wang, Z.; Wang, C. A highly sensitive and fast-responding sensor based on electrospun In_2O_3 nanofibers. *Sens. Actuators B Chem.* **2009**, *142*, 61–65. [CrossRef]
379. Wang, C.Y.; Ali, M.; Kups, T.; Röhlig, C.-C.; Cimalla, V.; Stauden, T.; Ambacher, O. NO_x sensing properties of In_2O_3 nanoparticles prepared by metal organic chemical vapor deposition. *Sens. Actuators B Chem.* **2008**, *130*, 589–593. [CrossRef]
380. Neri, G.; Bonavita, A.; Micali, G.; Rizzo, G.; Callone, E.; Carturan, G. Resistive CO gas sensors based on In_2O_3 and $InSnO_x$ nanopowders synthesized via starch-aided sol–gel process for automotive applications. *Sens. Actuators B Chem.* **2008**, *132*, 224–233. [CrossRef]
381. Kim, S.-J.; Hwang, I.-S.; Choi, J.-K.; Kang, Y.C.; Lee, J.-H. Enhanced C_2H_5OH sensing characteristics of nano-porous In_2O_3 hollow spheres prepared by sucrose-mediated hydrothermal reaction. *Sens. Actuators B Chem.* **2011**, *155*, 512–518. [CrossRef]
382. Guo, L.; Shen, X.; Zhu, G.; Chen, K. Preparation and gas-sensing performance of In_2O_3 porous nanoplatelets. *Sens. Actuators B Chem.* **2011**, *155*, 752–758. [CrossRef]
383. Zhang, Y.; Zheng, Z.; Yang, F. Highly sensitive and selective alcohol sensors based on Ag-doped In_2O_3 coating. *Ind. Eng. Chem. Res.* **2010**, *49*, 3539–3543. [CrossRef]
384. Lai, X.; Wang, D.; Han, N.; Du, J.; Li, J.; Xing, C.; Chen, Y.; Li, X. Ordered arrays of bead-chain-like In_2O_3 nanorods and their enhanced sensing performance for formaldehyde. *Chem. Mater.* **2010**, *22*, 3033–3042. [CrossRef]
385. Ye, Z.; Bardelli, S.; Wu, K.; Sarkar, A.; Swindle, A.; Wang, J. Synthesis, crystal growth, electronic properties and optical properties of Y6IV2. 5S14 (IV= Si, Ge). *Z. Für Anorg. Und Allg. Chem.* **2022**, *648*, e202100271.
386. Huang, H.; Lee, Y.; Tan, O.; Zhou, W.; Peng, N.; Zhang, Q. High sensitivity SnO_2 single-nanorod sensors for the detection of H_2 gas at low temperature. *Nanotechnology* **2009**, *20*, 115501. [CrossRef]
387. Liu, L.; Li, S.; Wang, L.; Guo, C.; Dong, Q.; Li, W. Enhancement ethanol sensing properties of NiO–SnO_2 nanofibers. *J. Am. Ceram. Soc.* **2011**, *94*, 771–775. [CrossRef]
388. Wang, Z.; Li, Z.; Sun, J.; Zhang, H.; Wang, W.; Zheng, W.; Wang, C. Improved hydrogen monitoring properties based on p-NiO/n-SnO_2 heterojunction composite nanofibers. *J. Phys. Chem. C* **2010**, *114*, 6100–6105. [CrossRef]
389. Yang, Z.; Li, L.-M.; Wan, Q.; Liu, Q.-H.; Wang, T.-H. High-performance ethanol sensing based on an aligned assembly of ZnO nanorods. *Sens. Actuators B Chem.* **2008**, *135*, 57–60. [CrossRef]
390. Liu, J.; Li, Y.; Jiang, J.; Huang, X. C@ZnO nanorod array-based hydrazine electrochemical sensor with improved sensitivity and stability. *Dalton Trans.* **2010**, *39*, 8693–8697. [CrossRef] [PubMed]
391. Ibrahim, A.A.; Dar, G.N.; Zaidi, S.A.; Umar, A.; Abaker, M.; Bouzid, H.; Baskoutas, S. Growth and properties of Ag-doped ZnO nanoflowers for highly sensitive phenyl hydrazine chemical sensor application. *Talanta* **2012**, *93*, 257–263. [CrossRef] [PubMed]
392. Ahn, M.W.; Park, K.S.; Heo, J.H.; Kim, D.W.; Choi, K.J.; Park, J.G. On-chip fabrication of ZnO-nanowire gas sensor with high gas sensitivity. *Sens. Actuators B Chem.* **2009**, *138*, 168–173. [CrossRef]
393. Chang, S.J.; Weng, W.Y.; Hsu, C.L.; Hsueh, T.J. High sensitivity of a ZnO nanowire-based ammonia gas sensor with Pt nanoparticles. *Nano Commun. Netw.* **2010**, *1*, 283–288. [CrossRef]
394. Liu, Z.; Yamazaki, T.; Shen, Y.; Kikuta, T.; Nakatani, N.; Li, Y. O_2 and CO sensing of Ga_2O_3 multiple nanowire gas sensors. *Sens. Actuators B Chem.* **2008**, *129*, 666–670. [CrossRef]
395. Song, X.; Gao, L.; Mathur, S. Synthesis, Characterization, and Gas Sensing Properties of Porous Nickel Oxide Nanotubes. *J. Phys. Chem. C* **2011**, *115*, 21730–21735. [CrossRef]

396. Wu, Z.; Yu, K.; Zhang, S.; Xie, Y. Hematite Hollow Spheres with a Mesoporous Shell: Controlled Synthesis and Applications in Gas Sensor and Lithium Ion Batteries. *J. Phys. Chem. C* **2008**, *112*, 11307–11313. [CrossRef]
397. Yu, R.; Li, Z.; Wang, D.; Lai, X.; Xing, C.; Yang, M.; Xing, X. Fe_2TiO_5/α-Fe_2O_3 nanocomposite hollow spheres with enhanced gas-sensing properties. *Scr. Mater.* **2010**, *63*, 155–158. [CrossRef]
398. Zheng, W.; Lu, X.; Wang, W.; Li, Z.; Zhang, H.; Wang, Z.; Xu, X.; Li, S.; Wang, C. Assembly of Pt nanoparticles on electrospun In_2O_3 nanofibers for H_2S detection. *J. Colloid Interface Sci.* **2009**, *338*, 366–370. [CrossRef]
399. Gou, X.; Wang, G.; Yang, J.; Park, J.; Wexler, D. Chemical synthesis, characterisation and gas sensing performance of copper oxide nanoribbons. *J. Mater. Chem.* **2008**, *18*, 965–969. [CrossRef]
400. Hoa, N.D.; Van Quy, N.; Jung, H.; Kim, D.; Kim, H.; Hong, S.-K. Synthesis of porous CuO nanowires and its application to hydrogen detection. *Sens. Actuators B Chem.* **2010**, *146*, 266–272. [CrossRef]
401. Park, J.; Shen, X.; Wang, G. Solvothermal synthesis and gas-sensing performance of Co_3O_4 hollow nanospheres. *Sens. Actuators B Chem.* **2009**, *136*, 494–498. [CrossRef]
402. Ma, J.; Zhang, J.; Wang, S.; Wang, T.; Lian, J.; Duan, X.; Zheng, W. Topochemical Preparation of WO_3 Nanoplates through Precursor H2WO4 and Their Gas-Sensing Performances. *J. Phys. Chem. C* **2011**, *115*, 18157–18163. [CrossRef]
403. Fortunato, E.; Barquinha, P.; Martins, R. Oxide semiconductor thin-film transistors: A review of recent advances. *Adv. Mater.* **2012**, *24*, 2945–2986. [CrossRef]
404. Sheng, J.; Jeong, H.-J.; Han, K.-L.; Hong, T.; Park, J.-S. Review of recent advances in flexible oxide semiconductor thin-film transistors. *J. Inf. Disp.* **2017**, *18*, 159–172. [CrossRef]
405. Kim, S.J.; Yoon, S.; Kim, H.J. Review of solution-processed oxide thin-film transistors. *Jpn. J. Appl. Phys.* **2014**, *53*, 02BA02. [CrossRef]
406. Du Ahn, B.; Jeon, H.-J.; Sheng, J.; Park, J.; Park, J.-S. A review on the recent developments of solution processes for oxide thin film transistors. *Semicond. Sci. Technol.* **2015**, *30*, 064001. [CrossRef]
407. Chen, R.; Lan, L. Solution-processed metal-oxide thin-film transistors: A review of recent developments. *Nanotechnology* **2019**, *30*, 312001. [CrossRef]
408. Park, S.P.; Kim, H.J.; Lee, J.H.; Kim, H.J. Glucose-based resistive random access memory for transient electronics. *J. Inf. Disp.* **2019**, *20*, 231–237. [CrossRef]
409. Wang, P.; Wu, L.; Lu, Z.; Li, Q.; Yin, W.; Ding, F.; Han, H. Gecko-inspired nanotentacle surface-enhanced Raman spectroscopy substrate for sampling and reliable detection of pesticide residues in fruits and vegetables. *Anal. Chem.* **2017**, *89*, 2424–2431. [CrossRef] [PubMed]
410. Song, H.; Zhang, Y.; Wang, S.; Huang, K.; Luo, Y.; Zhang, W.; Xu, W. Label-free polygonal-plate fluorescent-hydrogel biosensor for ultrasensitive microRNA detection. *Sens. Actuators B Chem.* **2020**, *306*, 127554. [CrossRef]
411. Hernández-Cancel, G.; Suazo-Dávila, D.; Medina-Guzmán, J.; Rosado-González, M.; Díaz-Vázquez, L.M.; Griebenow, K. Chemically glycosylation improves the stability of an amperometric horseradish peroxidase biosensor. *Anal. Chim. Acta* **2015**, *854*, 129–139. [CrossRef]
412. Zheng, H.; Liu, M.; Yan, Z.; Chen, J. Highly selective and stable glucose biosensor based on incorporation of platinum nanoparticles into polyaniline-montmorillonite hybrid composites. *Microchem. J.* **2020**, *152*, 104266. [CrossRef]
413. Scognamiglio, V.; Antonacci, A.; Arduini, F.; Moscone, D.; Campos, E.V.; Fraceto, L.F.; Palleschi, G. An eco-designed paper-based algal biosensor for nanoformulated herbicide optical detection. *J. Hazard. Mater.* **2019**, *373*, 483–492. [CrossRef]
414. Wang, M.; Yin, H.; Zhou, Y.; Sui, C.; Wang, Y.; Meng, X.; Waterhouse, G.I.; Ai, S. Photoelectrochemical biosensor for microRNA detection based on a MoS_2/g-C_3N_4/black TiO_2 heterojunction with Histostar@ AuNPs for signal amplification. *Biosens. Bioelectron.* **2019**, *128*, 137–143. [CrossRef]
415. Liu, H.; Duan, C.; Yang, C.; Chen, X.; Shen, W.; Zhu, Z. A novel nitrite biosensor based on the direct electron transfer hemoglobin immobilized in the WO_3 nanowires with high length–diameter ratio. *Mater. Sci. Eng. C* **2015**, *53*, 43–49. [CrossRef]
416. Dong, Y.; Zheng, J. A nonenzymatic L-cysteine sensor based on SnO_2-MWCNTs nanocomposites. *J. Mol. Liq.* **2014**, *196*, 280–284. [CrossRef]
417. Zhang, X.; Li, W.; Zhou, Y.; Chai, Y.; Yuan, R. An ultrasensitive electrochemiluminescence biosensor for MicroRNA detection based on luminol-functionalized Au NPs@ ZnO nanomaterials as signal probe and dissolved O_2 as coreactant. *Biosens. Bioelectron.* **2019**, *135*, 8–13. [CrossRef]
418. Zhou, Q.; Yang, L.; Wang, G.; Yang, Y. Acetylcholinesterase biosensor based on SnO_2 nanoparticles–carboxylic graphene–nafion modified electrode for detection of pesticides. *Biosens. Bioelectron.* **2013**, *49*, 25–31. [CrossRef] [PubMed]
419. Li, L.; Huang, J.; Wang, T.; Zhang, H.; Liu, Y.; Li, J. An excellent enzyme biosensor based on Sb-doped SnO_2 nanowires. *Biosens. Bioelectron.* **2010**, *25*, 2436–2441. [CrossRef] [PubMed]
420. Liu, C.; Hong, M.; Lum, M.; Flotow, H.; Ghadessy, F.; Zhang, J. Large-area micro/nanostructures fabrication in quartz by laser interference lithography and dry etching. *Appl. Phys. A* **2010**, *101*, 237–241. [CrossRef]
421. Elahi, N.; Kamali, M.; Baghersad, M.H.; Amini, B. A fluorescence Nano-biosensors immobilization on Iron (MNPs) and gold (AuNPs) nanoparticles for detection of Shigella spp. *Mater. Sci. Eng. C* **2019**, *105*, 110113. [CrossRef] [PubMed]
422. Zhou, Y.; Yang, L.; Li, S.; Dang, Y. A novel electrochemical sensor for highly sensitive detection of bisphenol A based on the hydrothermal synthesized Na-doped WO_3 nanorods. *Sens. Actuators B Chem.* **2017**, *245*, 238–246. [CrossRef]

423. Rathinamala, I.; Jeyakumaran, N.; Prithivikumaran, N. Sol-gel assisted spin coated CdS/PS electrode based glucose biosensor. *Vacuum* **2019**, *161*, 291–296. [CrossRef]
424. Cobianu, C.; Dumbravescu, N.; Serban, B.-C.; Buiu, O.; Romanitan, C.; Comanescu, F.; Danila, M.; Marinescu, R.; Avramescu, V.; Ionescu, O. Sonochemically synthetized ZnO-Graphene nanohybrids and its characterization. *Rev. Adv. Mater. Sci.* **2020**, *59*, 176–187. [CrossRef]
425. Liu, H.; Guo, K.; Duan, C.; Dong, X.; Gao, J. Hollow TiO_2 modified reduced graphene oxide microspheres encapsulating hemoglobin for a mediator-free biosensor. *Biosens. Bioelectron.* **2017**, *87*, 473–479. [CrossRef]
426. Santos, L.; Silveira, C.M.; Elangovan, E.; Neto, J.P.; Nunes, D.; Pereira, L.; Martins, R.; Viegas, J.; Moura, J.J.; Todorovic, S. Synthesis of WO_3 nanoparticles for biosensing applications. *Sens. Actuators B Chem.* **2016**, *223*, 186–194. [CrossRef]
427. Dong, S.; Tong, M.; Zhang, D.; Huang, T. The strategy of nitrite and immunoassay human IgG biosensors based on ZnO@ ZIF-8 and ionic liquid composite film. *Sens. Actuators B Chem.* **2017**, *251*, 650–657. [CrossRef]
428. Zhang, B.; Wang, H.; Xi, J.; Zhao, F.; Zeng, B. In situ formation of inorganic/organic heterojunction photocatalyst of WO3/Au/polydopamine for immunoassay of human epididymal protein 4. *Electrochim. Acta* **2020**, *331*, 135350. [CrossRef]
429. Enesca, A.; Isac, L.; Duta, A. Charge carriers injection in tandem semiconductors for dyes mineralization. *Appl. Catal. B Environ.* **2015**, *162*, 352–363. [CrossRef]
430. Mihaly, M.; Lacatusu, I.; Enesca, I.A.; Meghea, A. Hybride nanomaterials based on silica coated C60 clusters obtained by microemulsion technique. *Mol. Cryst. Liq. Cryst.* **2008**, *483*, 205–215. [CrossRef]
431. Visa, M.; Andronic, L.; Enesca, A. Behavior of the new composites obtained from fly ash and titanium dioxide in removing of the pollutants from wastewater. *Appl. Surf. Sci.* **2016**, *388*, 359–369. [CrossRef]
432. Korotcenkov, G.; Han, S.-D.; Cho, B.; Brinzari, V. Grain size effects in sensor response of nanostructured SnO2-and In2O3-based conductometric thin film gas sensor. *Crit. Rev. Solid State Mater. Sci.* **2009**, *34*, 1–17. [CrossRef]
433. Vander Wal, R.; Hunter, G.; Xu, J.; Kulis, M.; Berger, G.; Ticich, T. Metal-oxide nanostructure and gas-sensing performance. *Sens. Actuators B Chem.* **2009**, *138*, 113–119. [CrossRef]
434. Umar, A.; Rahman, M.; Al-Hajry, A.; Hahn, Y.-B. Highly-sensitive cholesterol biosensor based on well-crystallized flower-shaped ZnO nanostructures. *Talanta* **2009**, *78*, 284–289. [CrossRef]
435. Oh, J.; Yoo, G.; Chang, Y.W.; Kim, H.J.; Jose, J.; Kim, E.; Pyun, J.-C.; Yoo, K.-H. A carbon nanotube metal semiconductor field effect transistor-based biosensor for detection of amyloid-beta in human serum. *Biosens. Bioelectron.* **2013**, *50*, 345–350. [CrossRef]
436. Kao, C.H.; Chen, H.; Hou, F.Y.S.; Chang, S.W.; Chang, C.W.; Lai, C.S.; Chen, C.P.; He, Y.Y.; Lin, S.-R.; Hsieh, K.M. Fabrication of multianalyte CeO_2 nanograin electrolyte–insulator–semiconductor biosensors by using CF4 plasma treatment. *Sens. Bio-Sens. Res.* **2015**, *5*, 71–77. [CrossRef]
437. Zhao, J.; Wu, D.; Zhi, J. A novel tyrosinase biosensor based on biofunctional ZnO nanorod microarrays on the nanocrystalline diamond electrode for detection of phenolic compounds. *Bioelectrochemistry* **2009**, *75*, 44–49. [CrossRef]
438. Ahmad, M.; Pan, C.; Luo, Z.; Zhu, J. A single ZnO nanofiber-based highly sensitive amperometric glucose biosensor. *J. Phys. Chem. C* **2010**, *114*, 9308–9313. [CrossRef]
439. Chu, X.; Zhu, X.; Dong, Y.; Chen, T.; Ye, M.; Sun, W. An amperometric glucose biosensor based on the immobilization of glucose oxidase on the platinum electrode modified with NiO doped ZnO nanorods. *J. Electroanal. Chem.* **2012**, *676*, 20–26. [CrossRef]
440. Li, C.; Liu, Y.; Li, L.; Du, Z.; Xu, S.; Zhang, M.; Yin, X.; Wang, T. A novel amperometric biosensor based on NiO hollow nanospheres for biosensing glucose. *Talanta* **2008**, *77*, 455–459. [CrossRef] [PubMed]
441. Fang, B.; Zhang, C.; Wang, G.; Wang, M.; Ji, Y. A glucose oxidase immobilization platform for glucose biosensor using ZnO hollow nanospheres. *Sens. Actuators B Chem.* **2011**, *155*, 304–310. [CrossRef]
442. Yang, C.; Xu, C.; Wang, X. ZnO/Cu nanocomposite: A platform for direct electrochemistry of enzymes and biosensing applications. *Langmuir* **2012**, *28*, 4580–4585. [CrossRef] [PubMed]
443. Chen, H.; Rim, Y.S.; Wang, I.C.; Li, C.; Zhu, B.; Sun, M.; Goorsky, M.S.; He, X.; Yang, Y. Quasi-two-dimensional metal oxide semiconductors based ultrasensitive potentiometric biosensors. *ACS Nano* **2017**, *11*, 4710–4718. [CrossRef]
444. Rim, Y.S. Review of metal oxide semiconductors-based thin-film transistors for point-of-care sensor applications. *J. Inf. Disp.* **2020**, *21*, 203–210. [CrossRef]
445. Sarkar, D.; Liu, W.; Xie, X.; Anselmo, A.C.; Mitragotri, S.; Banerjee, K. MoS_2 field-effect transistor for next-generation label-free biosensors. *ACS Nano* **2014**, *8*, 3992–4003. [CrossRef]
446. Smith, J.T.; Shah, S.S.; Goryll, M.; Stowell, J.R.; Allee, D.R. Flexible ISFET biosensor using IGZO metal oxide TFTs and an ITO sensing layer. *IEEE Sens. J.* **2013**, *14*, 937–938. [CrossRef]
447. Jung, J.; Kim, S.J.; Lee, K.W.; Yoon, D.H.; Kim, Y.-g.; Kwak, H.Y.; Dugasani, S.R.; Park, S.H.; Kim, H.J. Approaches to label-free flexible DNA biosensors using low-temperature solution-processed InZnO thin-film transistors. *Biosens. Bioelectron.* **2014**, *55*, 99–105. [CrossRef]
448. Rim, Y.S.; Bae, S.-H.; Chen, H.; Yang, J.L.; Kim, J.; Andrews, A.M.; Weiss, P.S.; Yang, Y.; Tseng, H.-R. Printable ultrathin metal oxide semiconductor-based conformal biosensors. *ACS Nano* **2015**, *9*, 12174–12181. [CrossRef]
449. Rahman, M.M.; Saleh Ahammad, A.; Jin, J.-H.; Ahn, S.J.; Lee, J.-J. A comprehensive review of glucose biosensors based on nanostructured metal-oxides. *Sensors* **2010**, *10*, 4855–4886. [CrossRef]
450. Kaushik, A.; Solanki, P.R.; Kaneto, K.; Kim, C.; Ahmad, S.; Malhotra, B.D. Nanostructured iron oxide platform for impedimetric cholesterol detection. *Electroanal. Int. J. Devoted Fundam. Pract. Asp. Electroanal.* **2010**, *22*, 1045–1055. [CrossRef]

451. Umar, A.; Rahman, M.; Hahn, Y.-B. Ultra-sensitive hydrazine chemical sensor based on high-aspect-ratio ZnO nanowires. *Talanta* **2009**, *77*, 1376–1380. [CrossRef] [PubMed]
452. Solanki, P.R.; Kaushik, A.; Ansari, A.A.; Malhotra, B. Nanostructured zinc oxide platform for cholesterol sensor. *Appl. Phys. Lett.* **2009**, *94*, 143901. [CrossRef]
453. Singh, S.; Arya, S.K.; Pandey, P.; Malhotra, B.; Saha, S.; Sreenivas, K.; Gupta, V. Cholesterol biosensor based on rf sputtered zinc oxide nanoporous thin film. *Appl. Phys. Lett.* **2007**, *91*, 063901. [CrossRef]
454. Wang, C.; Tan, X.; Chen, S.; Yuan, R.; Hu, F.; Yuan, D.; Xiang, Y. Highly-sensitive cholesterol biosensor based on platinum–gold hybrid functionalized ZnO nanorods. *Talanta* **2012**, *94*, 263–270. [CrossRef]
455. Ahmad, M.; Pan, C.; Gan, L.; Nawaz, Z.; Zhu, J. Highly sensitive amperometric cholesterol biosensor based on Pt-incorporated fullerene-like ZnO nanospheres. *J. Phys. Chem. C* **2010**, *114*, 243–250. [CrossRef]
456. Ahmad, R.; Tripathy, N.; Hahn, Y.-B. Wide linear-range detecting high sensitivity cholesterol biosensors based on aspect-ratio controlled ZnO nanorods grown on silver electrodes. *Sens. Actuators B Chem.* **2012**, *169*, 382–386. [CrossRef]
457. Khan, R.; Kaushik, A.; Solanki, P.R.; Ansari, A.A.; Pandey, M.K.; Malhotra, B. Zinc oxide nanoparticles-chitosan composite film for cholesterol biosensor. *Anal. Chim. Acta* **2008**, *616*, 207–213. [CrossRef]
458. Ansari, A.A.; Kaushik, A.; Solanki, P.R.; Malhotra, B.E.D. Electrochemical cholesterol sensor based on tin oxide-chitosan nanobiocomposite film. *Electroanal. Int. J. Devoted Fundam. Pract. Asp. Electroanal.* **2009**, *21*, 965–972. [CrossRef]
459. Salimi, A.; Hallaj, R.; Soltanian, S. Fabrication of a Sensitive Cholesterol Biosensor Based on Cobalt-oxide Nanostructures Electrodeposited onto Glassy Carbon Electrode. *Electroanal. Int. J. Devoted Fundam. Pract. Asp. Electroanal.* **2009**, *21*, 2693–2700. [CrossRef]
460. Ali, S.M.U.; Ibupoto, Z.H.; Salman, S.; Nur, O.; Willander, M.; Danielsson, B. Selective determination of urea using urease immobilized on ZnO nanowires. *Sens. Actuators B Chem.* **2011**, *160*, 637–643. [CrossRef]
461. Chen, X.; Yang, Z.; Si, S. Potentiometric urea biosensor based on immobilization of urease onto molecularly imprinted TiO_2 film. *J. Electroanal. Chem.* **2009**, *635*, 1–6. [CrossRef]
462. Kaushik, A.; Solanki, P.R.; Ansari, A.A.; Sumana, G.; Ahmad, S.; Malhotra, B.D. Iron oxide-chitosan nanobiocomposite for urea sensor. *Sens. Actuators B Chem.* **2009**, *138*, 572–580. [CrossRef]
463. Ali, A.; Ansari, A.A.; Kaushik, A.; Solanki, P.R.; Barik, A.; Pandey, M.; Malhotra, B. Nanostructured zinc oxide film for urea sensor. *Mater. Lett.* **2009**, *63*, 2473–2475. [CrossRef]
464. Solanki, P.R.; Dhand, C.; Kaushik, A.; Ansari, A.A.; Sood, K.; Malhotra, B. Nanostructured cerium oxide film for triglyceride sensor. *Sens. Actuators B Chem.* **2009**, *141*, 551–556. [CrossRef]
465. Luo, Y.; Liu, H.; Rui, Q.; Tian, Y. Detection of extracellular H_2O_2 released from human liver cancer cells based on TiO_2 nanoneedles with enhanced electron transfer of cytochrome c. *Anal. Chem.* **2009**, *81*, 3035–3041. [CrossRef]
466. Wang, J.; Li, S.; Zhang, Y. A sensitive DNA biosensor fabricated from gold nanoparticles, carbon nanotubes, and zinc oxide nanowires on a glassy carbon electrode. *Electrochim. Acta* **2010**, *55*, 4436–4440. [CrossRef]
467. Zhang, W.; Zheng, X.; Jiao, K. Label-free and enhanced DNA sensing platform for PML/RARA fusion gene detection based on nano-ZnO functionalized carbon ionic liquid electrode. *Sens. Actuators B Chem.* **2012**, *162*, 396–399. [CrossRef]
468. Zuo, S.-H.; Zhang, L.-F.; Yuan, H.-H.; Lan, M.-B.; Lawrance, G.A.; Wei, G. Electrochemical detection of DNA hybridization by using a zirconia modified renewable carbon paste electrode. *Bioelectrochemistry* **2009**, *74*, 223–226. [CrossRef] [PubMed]
469. Zhu, H.; Wang, J.; Xu, G. Fast synthesis of Cu_2O hollow microspheres and their application in DNA biosensor of hepatitis B virus. *Cryst. Growth Des.* **2009**, *9*, 633–638. [CrossRef]
470. Prabhakar, N.; Solanki, P.R.; Kaushik, A.; Pandey, M.; Malhotra, B. Peptide nucleic acid immobilized biocompatible silane nanocomposite platform for Mycobacterium tuberculosis detection. *Electroanalysis* **2010**, *22*, 2672–2682. [CrossRef]
471. Abu-Salah, K.M.; Alrokyan, S.A.; Khan, M.N.; Ansari, A.A. Nanomaterials as analytical tools for genosensors. *Sensors* **2010**, *10*, 963–993. [CrossRef] [PubMed]
472. Das, M.; Sumana, G.; Nagarajan, R.; Malhotra, B. Zirconia based nucleic acid sensor for Mycobacterium tuberculosis detection. *Appl. Phys. Lett.* **2010**, *96*, 133703. [CrossRef]
473. Sun, W.; Qin, P.; Gao, H.; Li, G.; Jiao, K. Electrochemical DNA biosensor based on chitosan/nano-V_2O_5/MWCNTs composite film modified carbon ionic liquid electrode and its application to the LAMP product of Yersinia enterocolitica gene sequence. *Biosens. Bioelectron.* **2010**, *25*, 1264–1270. [CrossRef]
474. Tsekenis, G.; Chatzipetrou, M.; Massaouti, M.; Zergioti, I. Comparative Assessment of Affinity-Based Techniques for Oriented Antibody Immobilization towards Immunosensor Performance Optimization. *J. Sens.* **2019**, *2019*, 6754398.
475. Gajos, K.; Szafraniec, K.; Petrou, P.; Budkowski, A. Surface density dependent orientation and immunological recognition of antibody on silicon: TOF-SIMS and surface analysis of two covalent immobilization methods. *Appl. Surf. Sci.* **2020**, *518*, 146269. [CrossRef]
476. Wang, J. *Analytical Electrochemistry*, 3rd ed.; John Wiley & Sons, Inc.: Hoboken, NJ, USA, 2006.
477. Che, X.; Yuan, R.; Chai, Y.; Li, J.; Song, Z.; Wang, J. Amperometric immunosensor for the determination of α-1-fetoprotein based on multiwalled carbon nanotube–silver nanoparticle composite. *J. Colloid Interface Sci.* **2010**, *345*, 174–180. [CrossRef]
478. Ra, H.-W.; Kim, J.-T.; Khan, R.; Sharma, D.; Yook, Y.-G.; Hahn, Y.-B.; Park, J.-H.; Kim, D.-G.; Im, Y.-H. Robust and multifunctional nanosheath for chemical and biological nanodevices. *Nano Lett.* **2012**, *12*, 1891–1897. [CrossRef]

479. Wei, Q.; Xiang, Z.; He, J.; Wang, G.; Li, H.; Qian, Z.; Yang, M. Dumbbell-like Au-Fe_3O_4 nanoparticles as label for the preparation of electrochemical immunosensors. *Biosens. Bioelectron.* **2010**, *26*, 627–631. [CrossRef]
480. Gou, N.; Onnis-Hayden, A.; Gu, A.Z. Mechanistic toxicity assessment of nanomaterials by whole-cell-array stress genes expression analysis. *Environ. Sci. Technol.* **2010**, *44*, 5964–5970. [CrossRef]
481. Yang, Z.; Ye, Z.; Zhao, B.; Zong, X.; Wang, P. A rapid response time and highly sensitive amperometric glucose biosensor based on ZnO nanorod via citric acid-assisted annealing route. *Phys. E Low-Dimens. Syst. Nanostructures* **2010**, *42*, 1830–1833. [CrossRef]
482. Kong, T.; Chen, Y.; Ye, Y.; Zhang, K.; Wang, Z.; Wang, X. An amperometric glucose biosensor based on the immobilization of glucose oxidase on the ZnO nanotubes. *Sens. Actuators B Chem.* **2009**, *138*, 344–350. [CrossRef]
483. Lei, Y.; Yan, X.; Luo, N.; Song, Y.; Zhang, Y. ZnO nanotetrapod network as the adsorption layer for the improvement of glucose detection via multiterminal electron-exchange. *Colloids Surf. A: Physicochem. Eng. Asp.* **2010**, *361*, 169–173. [CrossRef]
484. Yang, K.; She, G.-W.; Wang, H.; Ou, X.-M.; Zhang, X.-H.; Lee, C.-S.; Lee, S.-T. ZnO nanotube arrays as biosensors for glucose. *J. Phys. Chem.* **2009**, *113*, 20169–20172. [CrossRef]
485. Pradhan, D.; Niroui, F.; Leung, K. High-performance, flexible enzymatic glucose biosensor based on ZnO nanowires supported on a gold-coated polyester substrate. *ACS Appl. Mater. Interfaces* **2010**, *2*, 2409–2412. [CrossRef]
486. Wang, Y.-T.; Yu, L.; Zhu, Z.-Q.; Zhang, J.; Zhu, J.-Z.; Fan, C.-H. Improved enzyme immobilization for enhanced bioelectrocatalytic activity of glucose sensor. *Sens. Actuators B Chem.* **2009**, *136*, 332–337. [CrossRef]
487. Bao, S.J.; Li, C.M.; Zang, J.F.; Cui, X.Q.; Qiao, Y.; Guo, J. New nanostructured TiO_2 for direct electrochemistry and glucose sensor applications. *Adv. Funct. Mater.* **2008**, *18*, 591–599. [CrossRef]
488. Jang, H.D.; Kim, S.K.; Chang, H.; Roh, K.-M.; Choi, J.-W.; Huang, J. A glucose biosensor based on TiO_2–graphene composite. *Biosens. Bioelectron.* **2012**, *38*, 184–188. [CrossRef]
489. Umar, A.; Rahman, M.; Al-Hajry, A.; Hahn, Y.-B. Enzymatic glucose biosensor based on flower-shaped copper oxide nanostructures composed of thin nanosheets. *Electrochem. Commun.* **2009**, *11*, 278–281. [CrossRef]
490. Patil, D.; Dung, N.Q.; Jung, H.; Ahn, S.Y.; Jang, D.M.; Kim, D. Enzymatic glucose biosensor based on CeO_2 nanorods synthesized by non-isothermal precipitation. *Biosens. Bioelectron.* **2012**, *31*, 176–181. [CrossRef] [PubMed]
491. Yang, L.; Ren, X.; Tang, F.; Zhang, L. A practical glucose biosensor based on Fe_3O_4 nanoparticles and chitosan/nafion composite film. *Biosens. Bioelectron.* **2009**, *25*, 889–895. [CrossRef]
492. Umar, A.; Rahman, M.; Hahn, Y.-B. MgO polyhedral nanocages and nanocrystals based glucose biosensor. *Electrochem. Commun.* **2009**, *11*, 1353–1357. [CrossRef]
493. Umar, A.; Rahman, M.; Vaseem, M.; Hahn, Y.-B. Ultra-sensitive cholesterol biosensor based on low-temperature grown ZnO nanoparticles. *Electrochem. Commun.* **2009**, *11*, 118–121. [CrossRef]
494. Israr, M.Q.; Sadaf, J.R.; Asif, M.; Nur, O.; Willander, M.; Danielsson, B. Potentiometric cholesterol biosensor based on ZnO nanorods chemically grown on Ag wire. *Thin Solid Film* **2010**, *519*, 1106–1109. [CrossRef]
495. Ansari, A.A.; Kaushik, A.; Solanki, P.; Malhotra, B. Sol–gel derived nanoporous cerium oxide film for application to cholesterol biosensor. *Electrochem. Commun.* **2008**, *10*, 1246–1249. [CrossRef]
496. Zhang, W.; Yang, T.; Huang, D.M.; Jiao, K. Electrochemical sensing of DNA immobilization and hybridization based on carbon nanotubes/nano zinc oxide/chitosan composite film. *Chin. Chem. Lett.* **2008**, *19*, 589–591. [CrossRef]
497. Zhang, W.; Yang, T.; Zhuang, X.; Guo, Z.; Jiao, K. An ionic liquid supported CeO_2 nanoshuttles–carbon nanotubes composite as a platform for impedance DNA hybridization sensing. *Biosens. Bioelectron.* **2009**, *24*, 2417–2422. [CrossRef]
498. Ansari, A.A.; Kaushik, A.; Solanki, P.R.; Malhotra, B. Nanostructured zinc oxide platform for mycotoxin detection. *Bioelectrochemistry* **2010**, *77*, 75–81. [CrossRef]
499. Fu, X.; Wang, J.; Li, N.; Wang, L.; Pu, L. Label-free electrochemical immunoassay of carcinoembryonic antigen in human serum using magnetic nanorods as sensing probes. *Microchim. Acta* **2009**, *165*, 437–442. [CrossRef]
500. Wang, L.; Jia, X.; Zhou, Y.; Xie, Q.; Yao, S. Sandwich-type amperometric immunosensor for human immunoglobulin G using antibody-adsorbed Au/SiO_2 nanoparticles. *Microchim. Acta* **2010**, *168*, 245–251. [CrossRef]
501. Eryiğit, M.; Cepni, E.; Urhan, B.K.; Doğan, H.Ö.; Özer, T.Ö. Nonenzymatic glucose sensor based on poly (3, 4-ethylene dioxythiophene)/electroreduced graphene oxide modified gold electrode. *Synth. Met.* **2020**, *268*, 116488. [CrossRef]
502. Nguyen, T.N.; Jin, X.; Nolan, J.K.; Xu, J.; Le, K.V.H.; Lam, S.; Wang, Y.; Alam, M.A.; Lee, H. Printable nonenzymatic glucose biosensors using carbon nanotube-PtNP nanocomposites modified with AuRu for improved selectivity. *ACS Biomater. Sci. Eng.* **2020**, *6*, 5315–5325. [CrossRef] [PubMed]
503. Hwang, D.-W.; Lee, S.; Seo, M.; Chung, T.D. Recent advances in electrochemical non-enzymatic glucose sensors—A review. *Anal. Chim. Acta* **2018**, *1033*, 1–34. [CrossRef] [PubMed]
504. Burke, L. Premonolayer oxidation and its role in electrocatalysis. *Electrochim. Acta* **1994**, *39*, 1841–1848. [CrossRef]
505. Xiao, F.; Li, Y.; Gao, H.; Ge, S.; Duan, H. Growth of coral-like PtAu–MnO_2 binary nanocomposites on free-standing graphene paper for flexible nonenzymatic glucose sensors. *Biosens. Bioelectron.* **2013**, *41*, 417–423. [CrossRef]
506. Lee, S.; Lee, J.; Park, S.; Boo, H.; Kim, H.C.; Chung, T.D. Disposable non-enzymatic blood glucose sensing strip based on nanoporous platinum particles. *Appl. Mater. Today* **2018**, *10*, 24–29. [CrossRef]
507. Chen, H.; Fan, G.; Zhao, J.; Qiu, M.; Sun, P.; Fu, Y.; Han, D.; Cui, G. A portable micro glucose sensor based on copper-based nanocomposite structure. *New J. Chem.* **2019**, *43*, 7806–7813. [CrossRef]

508. Liu, X.; Yang, W.; Chen, L.; Jia, J. Three-dimensional copper foam supported CuO nanowire arrays: An efficient non-enzymatic glucose sensor. *Electrochim. Acta* **2017**, *235*, 519–526. [CrossRef]
509. Guascito, M.R.; Chirizzi, D.; Malitesta, C.; Siciliano, M.; Siciliano, T.; Tepore, A. Amperometric non-enzymatic bimetallic glucose sensor based on platinum tellurium microtubes modified electrode. *Electrochem. Commun.* **2012**, *22*, 45–48. [CrossRef]